Doctoral Thesis

Thermoelectric and electrical transport properties of Bi_2Te_3 compacted nanoparticles bulk material

by

Sepideh Izadi

The Thesis submitted to

Bielefeld University

Faculty of Physics

July, 2021

Supervisor

Prof. Dr. Gabi Schierning

To my parents and my lovely brother

Contents

Acknowledgement

Hereby, I would like to appreciate Prof. Gabi Schierning who not only set an example of a knowledgeable scientist but also one of the loveliest people I have ever met in my life.

I would especially thank the chemist research partners Prof. Stephan Schultz and Sarah Salloum at University of Duisburg-Essen for providing initial Bi_2Te_3 nanoparticles together with powder morphology characterization.

I would like to thank Dr. Ulrike Wolf for morphology characterization of Bi_2Te_3 compacted nanoparticles including AFM, Conductive-AFM and TEM analysis; special thanks to Almut for FIB sample preparation; together with specific surface area realization using BET method.

I would also thank the THz research partners Prof. Martin Mittendorf and Dr. Jeong Woo Han at University of Duisburg-Essen for the THz time-domain spectroscopy measurements together with data analysis using results of Hall characterization.

I would also like to thank Dr. Heike Schlörb for her continuous support and kindness. I would also thank Dr.Heiko Reith and Dr.Nicolas Perez for their nice support during my PhD study.

Finally, I thank the continuous support and encouragement of my parents, my younger brother and my long-term friends.

Funding

This project has received funding from the European Research Council (ERC) under the European Union's Horizon 2020 research and innovation programme (grant agreement No. 863823 MATTER), gratefully acknowledged by G.S. M.M. acknowledges funding by the Deutsche Forschungsgemeinschaft (DFG, German Research Foundation) – Project-ID 278162697 – SFB 1242. St.S. acknowledges funding by the Deutsche Forschungsgemeinschaft (DFG) within the Priority Program SPP 1708 "Material Synthesis near Room Temperature" (S. Schulz SCHU 1069/17-2), and Sa.S. acknowledges funding from the International Max Planck Research School IMPRS-RECHARGE.

Publications

1. Loor, M., Salloum, S., Kawulok, P., Izadi, S. *et al.* Ionic Liquid-Based Low-Temperature Synthesis of Phase-Pure Tetradymite-Type Materials and Their Thermoelectric Properties. *Inorg. Chem.* **59**, 3428–3436 (2020).

2. Salloum, S. *et al.* Influence of Nanoparticle Processing on the Thermoelectric Properties of $(Bi_xSb_{1-x})_2Te_3$ Ternary Alloys. *Open. Chem*. **10**, 189-198 (2021).

3. Izadi, S. *et al.* Interface-dominated topological transport in nanograined bulk Bi_2Te_3 (recently submitted)

List of Figures

List of Tables

Nomenclature

The following list contain the most important symbols and abbreviations which were used in this work.

Symbols

ρ	Resistivity
$M\rho$	Magneto-resistivity
ΔG	Magneto-conductance
l_{ϕ}	Phase coherence length
R	Resistance
R_{xx}	Longitudinal resistance
R_{xy}	Hall resistance
B	Magnetic field
μ	Mobility
n	Carrier concentration
S	Seebeck coefficient
σ	Electrical conductivity
k	Thermal conductivity
k_l	Lattice thermal conductivity
C_p	Heat capacity
α	Thermal diffusivity
$k_{\perp}$	In-plane thermal conductivity
$k_{\parallel}$	Cross-plane thermal conductivity
PF	Power factor
ZT	Figure of merit
k_B	Boltzmann constant
h	Plank constant
m^*	Effective mass
R	Reflectivity

E_F	Fermi energy
$f(E, E_F)$	Fermi Dirac distribution function
σ_f^B	Bulk Drude conductivity
σ_f^S	Surface Drude conductivity
σ_f^p	Plasmon conductivity of surface carriers
ω_P	Plasmon frequency
V_F	Fermi velocity
μ'	Chemical potential
γ_S	Surface scattering rate
τ_S	Surface scattering lifetime
n_B	Bulk carrier concentration
n_s	Surface carrier concentration
μ_B	Bulk carrier mobility
μ_s	Surface carrier mobility

Abbreviations

Bi_2Te_3	Bismuth telluride
TI	Topological insulator
DP	Dirac point
TRS	Time reversal symmetry
TE	Thermoelectric
THz	Terahertz
QH	Quantum Hall
QSH	Quantum spin Hall
SEM	Scanning electron microscope
EDX	Electron dispersive X-ray
AFM	Atomic force microscope
TEM	Transmission electron microscope
BET	Brunauer-Emmett-Teller
IL	Ionic Liquid
IR	Infrared spectroscopy

DOS	Density of state
CB	Conduction band
VB	Valence band
DC	Direct current
WAL	Weak anti localization
WL	Weak localization
HLN	Hikami Larkin Nagaoka
TKNN	Thouless, Kohmoto, Nightingale, and denNijs
SOC	Spin orbit coupling
PPMS	Physical property measurement system
VdP	Van der Pauw
ETO	Electrical transport option
TTO	Thermal transport option
STM	Scanning tunneling microscope
ARPES	Angle resolved photoemission spectroscopy
AB	Aharonov–Bohm
SDH	Schubnikov-de Haas
BZ	Brillouin zone

Introduction

Three-dimensional (3D) topological insulators (TIs) hosting surface carriers with extremely high mobility (μ) are intensively studied since their discovery due to their promising technical applications e.g. thermoelectricity. While surface transport properties of 3D TIs are of outmost importance for potential applications, they are difficult to characterize, yet utilize. The reason is that electrical transport properties of these materials are always dominated by bulk carriers that outnumber surface transport by orders of magnitude.

Within this thesis, it will be shown that the problem of bulk carrier dominance can be overcome conceptually by a nanoparticle-based material design strategy. Bi_2Te_3 nanoparticles that are well known for their excellent thermoelectric and topological insulating properties serve as model system. The Bi_2Te_3 nanoparticles were synthesized by the chemist partners at University of Duisburg-Essen with two different chemical approaches (classical and developed synthesis routes) in weakly binding ionic liquids (ILs) to ensure high purity of the nanoparticle surfaces. To make quantum transport visible on microscopic scale, nanoparticles having low levels of impurities and surface contaminations were compacted using hot pressing technique.

In this work, electrical transport properties of Bi_2Te_3 compacted nanoparticles which were synthesized by distinct chemical approaches were investigated using temperature-dependent resistivity (ρ), magnetoresistivity ($M\rho$) and Hall characterization techniques. To provide a better insight of the interplay between the observed transport properties and microstructural configuration of Bi_2Te_3 bulk samples, diverse morphological analysis including scanning electron microscope (SEM), electron dispersive X-ray (EDX), atomic force microscope (AFM), Conductive-AFM, Brunauer-Emmett-Teller (BET) and transmission electron microscope (TEM) were effectively employed.

Tailored-based electrical transport properties together with the observed evidences of surface transport carriers in a real TI Bi_2Te_3 bulk material, emphasizes on the unique nanoparticle-based design strategy. To elucidate separate contribution of surface and bulk transport carriers in the observed measurement signal, time-domain terahertz (THz) spectroscopy was successfully applied by the THz partner at University of Duisburg-Essen. Therewith, the observed THz spectra was mathematically modeled using three different contributions of surface and bulk Drude carriers together with plasmonic contribution of surface carriers.

Finally, to realize the importance of having high quality Bi_2Te_3 nanoparticles of having clean surfaces for thermoelectric (TE) applications, TE properties of Bi_2Te_3 nano bulk samples were investigated using Seebeck (S), electrical conductivity (σ) and thermal conductivity (k) characterization.

Hopefully, the obtained results of this thesis could open the path towards microscopic quantum materials as well as high efficient TE materials.

Chapter.1

Fundamentals of topological insulators

Introduction

TIs are new class of quantum materials representing a bulk band gap similar to the insulating phase of matter along with gapless surface states which are protected by time reversal symmetry (TRS)[1-2]. Compared to conventional surface states[3], topologically-protected surface carriers of TIs possess fascinating features defining them as a novel category of quantum materials. In 2016 the Nobel Prize in physics awarded to *D. J. Thouless*, *F. D. M. Haldane*, and *J. M. Koserlitz* for theoretical discovery of topological insulating phases of matter[4] which has opened new horizons in condensed matter physics, chemistry and material science. From that time, theoretical and experimental efforts have been invested on further exploration of these unique states of matter[5-6].

In the following, first quantum Hall (QH) effect as a preliminary introduction of topologically-protected materials is provided and explained in more details. Moreover, concepts of topology, quantum spin Hall (QSH) effect and 3D TIs are presented and discussed schematically. Finally, a brief summary of experimental techniques of visualization and characterization of topologically-protected carriers along with the most significant hindrance of topological carrier detection will be provided.

1.1. Quantum Hall effect

1.1.1. Manifestation of significant conflict

QH effect as one of the fundamental concepts in physics and material science plays a significant role for the discovery of TIs. In 1985 Nobel Prize in physics was awarded to German physicist *Klaus von Klitzing* for the discovery of QH effect[7]. The quantum Hall effect introduced a new geometry-independent state of matter that was microscopically similar to a normal insulator; however, it was theoretically confirmed that QH system was not topologically equivalent to a normal insulator[1]. Aiming at topologically-protected states of matter, conceptual perception of QH effect is inevitable. As illustrated in Fig.1 (a), confined electrons of a 2D QH system which are exposed to a strong magnetic field (B), reveal an orbiting electronic motion with frequency of ω_c known as cyclotron frequency[1]; therefore, as demonstrated in Fig.1 (b), spatially-localized and quantized levels known as Landau levels (ψ_m), with specific energy of ε_m are created. Based on eq.1, ε_m is directly related to ω_c,

$$\varepsilon_m = \hbar\omega_c(m + \frac{1}{2}) \qquad (1)$$

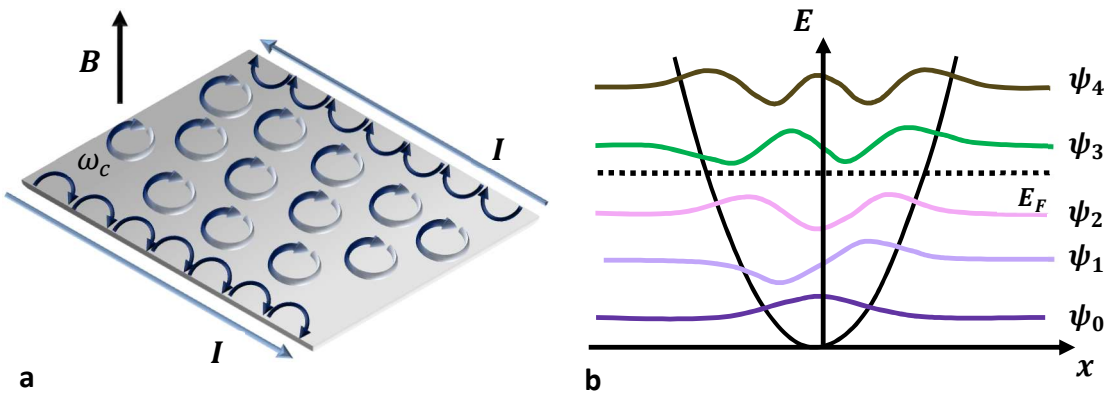

Fig.1: (a) Schematic representation of QH effect. (b) Schematic representation of harmonic oscillator wave functions.

As schematically represented in Fig.1 (b), Fermi level of E_F locating in the band gap of 2D electronic system, signifies a phase of matter which is not microscopically different from a conventional insulator. However, current of I resulting from skipping electronic motions (blue arrows), introduces metallic surrounding boundaries into the 2D QH system which is basically against the previous assumption. Based on QH experiment conducted in 1980[7], longitudinal resistivity (ρ_{xx}) represented with the red curve in Fig.2, exhibits an oscillating behavior as a function of B. Simultaneously, Hall resistance (R_H) starts increasing, representing quantized plateaus exactly over the same B interval where ρ_{xx} dropped to zero.

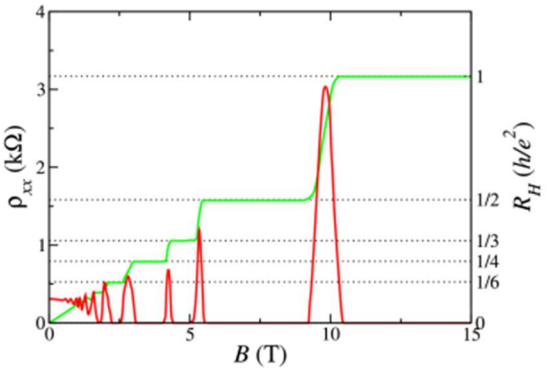

Fig.2: QH experiment[8]; red and green curves illustrate ρ_{xx} and R_H behavior respectively.

1.1.2. Topology

Historically, classification of diverse states of matter originates from principle of broken symmetry[9] where, crystalline solids, magnets and superconductors were classified based on translational, rotational and gauge symmetry breakage respectively. However, there is no symmetry which is clearly broken in a QH system. In another word, the difference between QH system and a normal insulator is not distinguishable based on the phase transition principle. To differentiate these two systems from each other, the concept of topology is required to be taken into account.

Topology is conceptually related to material classification based on geometrical properties using mathematical equations[10]. In Fig.3 (a) two different topological classes are demonstrated in red and blue; simply speaking, objects belonging to the red group (without any hole) are topologically distinct from objects belonging to the blue group (with one hole). Interestingly, objects of each topological classification are prone to be transformed into each other through bending or stretching without any surface breakage; as demonstrated in Fig.3 (b), a coffee cup is continuously converted into a donut yet, preserving the corresponding topology. However, surface breakage as a result of converting objects from one topological classification into the other one is unavoidable.

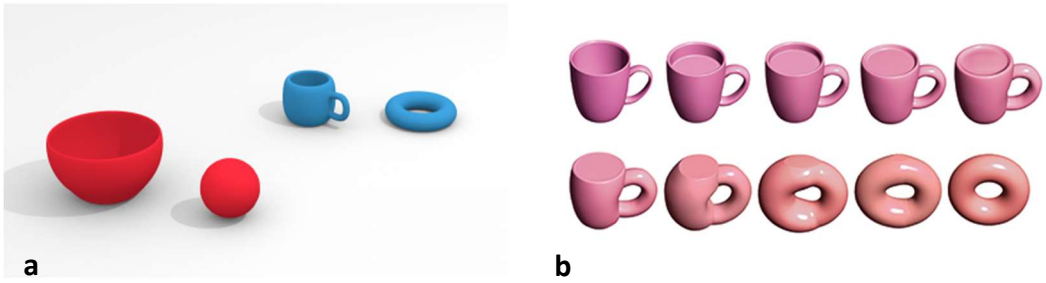

Fig.3: (a) Representation of two topological classifications. (b) Continuously deformation of a coffee cup into a donut[11].

Similarly, gapped band structures which can be continuously transformed into each other without closing the band gap, are classified into the same topological category[1]. This continuous transformation can be well explained based on the concept of topological invariant known as TKNN invariant or Chern number which was introduced for the first time by Thouless, Kohmoto, Nightingale, and denNijs[12]. By continuously deforming objects of the same topological class into each other TKNN invariant stays the same specifying independency of this number from details of the surface. Based on this concept, scientist found new classification of electronic structures where QH system was topologically distinct from a conventional insulator[1, 13]. TKNN as a criterion of topology

specification associates with Berry flux integration over the entire Brillouin zone (BZ). Considering BZ as a torus, the result of such integration over the whole BZ is equal to an integer number. Interestingly, this integer is exactly the one describing quantum Hall conductivity. Depending on topological properties, different systems exhibit distinct quantum Hall conductivities.

As demonstrated in Fig.4 (a), one-dimensional current of I is conducted on the edge of the 2D QH system by applying strong B. Interestingly, by introducing smooth deformation or non-magnetic impurities (yellow spheres) into the system, I still persists flowing around[14]. This feature can be interpreted as current robustness of QH system with respect to different kinds of perturbations as long as TKNN invariant stays the same.

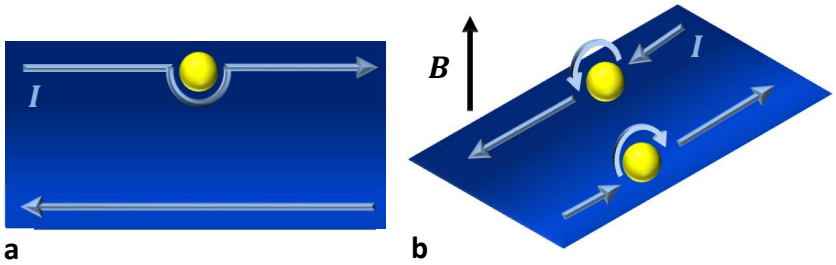

Fig.4: (a) Two-dimensional and (b) three-dimensional representation of QH system; blue arrows specify one-directional electronic motion in presence of non-magnetic impurities (yellow spheres).

Current Robustness against non-magnetic dislocations and disorders in the system associates with uni-directional electronic motion where electrons of the 2D QH system have only one degree of freedom. As demonstrated in Fig.4, by introducing non-magnetic impurities into the system, electrons persist moving on a detour-like trajectory around the incorporated impurity. Consequently, in the QH system, dissipationless electronic transport is offered by absence of back-scattered electronic motions[15]. Dissipationless electronic transport is of great interest for semiconducting electronic devices; however, providing a strong B creates a severe hindrance in potential application of QH effect.

1.2. Quantum Spin Hall effect

For the first time, *Bernevig et. al.* introduced quantum well of CdTe/HgTe/CdTe as the first QSH system where, HgTe layer was sandwiched between two CdTe layers with strong spin-orbit coupling (SOC)[16]. Theoretically, intrinsic interaction of SOC plays the role of strong B as was discussed in QH

effect, creating 2D metallic boundaries within the material. Materials representing QSH effect are known as 2D TIs[17].

A QSH system provides exclusively separated transport channels of electrons carrying spin-up and down directions. As illustrated in Fig.5 (a), system consists of four distinct transport channels which are hosted by electrons with spin-up and down moving in forward and backward directions respectively. Electrons of top and bottom edges demonstrate opposite transport features, i.e. while electrons with spin-up at the top edge move in forward direction, the corresponding spin-up electrons at the bottom edge move in the backward direction.

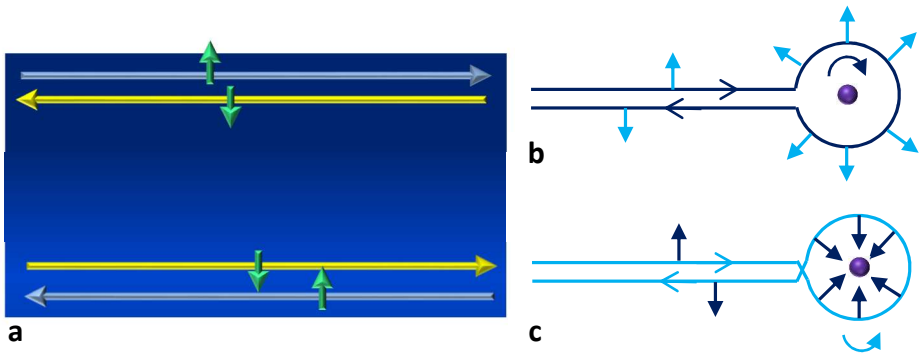

Fig.5: (a) Schematic representation of QSH system; while, spin-up/down electrons of the top edge move in forward/backward directions, respectively, spin-down/up electrons of the bottom edge move in forward/backward directions correspondingly. (b)-(c) Schematic illustration of destructive interference of electrons with spin-up and spin-down moving in CW and CCW directions respectively[14].

Two distinct blue and yellow lines of each edge carrying opposite spin directions do not interfere with the concept of current robustness. For more clarification, schematic illustrations of this concept are provided in Fig.5 (b)-(c) where electrons with spin-up and down directions encounter a non-magnetic impurity represented with a blue sphere. Electrons with spin-up and down persist moving on a detour-like trajectory in clockwise (CW) and counter-clockwise (CCW) directions respectively. After one rotation, the resulted phase difference would be equal to 2π resulting in a destructive interference of two back-scattered trajectories represented in Fig.5 (b) and (c).

1.3. Topological insulators

Topological systems such as TIs[1, 13], topological superconductors[2, 18] and Weyl semimetals[19-20] are known as new classifications of quantum materials. Due to the potential application of these materials in variety of fields including spintronic[21], thermoelectric (TE)[22], dissipationless electronics[15],

quantum computing[21], etc. they grabbed considerable attention in the last decade. As one of the main focuses of this work was invested on characterization of topologically-protected carriers of TIs, hence, more details of structural properties, material classification, outstanding features and characterization techniques of this novel category of quantum materials are provided and discussed in the following.

3D TIs feature a bulk band gap of a conventional semiconductor and metallic topological surface states on all crystal facets[5]. Electrons on these metallic surface states are robust with respect to localization[23]. Even with strong disorder on atomic scale, these electrons do not backscatter between states of opposite momentum and opposite spin[24]. This confers the high μ of the electrons occupying these surface states. Such electrons also penetrate energetic barriers caused by materials imperfections and atomic steps at the surfaces[23]. In contrast, magnetic impurities deteriorate TRS, leading to opening up a band gap in so-called gapless protected carriers[25-26]. These unique electronic properties propel visions of potential applications in quantum computing and spintronics[15, 21].

Compared to semiconducting materials where valence band (VB) and conduction band (CB) are separated with an energy gap of up to $\sim 3\ eV$[27], TIs offer a non-trivial electronic structure where VB is connected into the CB through linearly-dispersive topological carriers[1, 13]. Band structure of a TI is schematically represented in Fig.6 where the insulating band gap is traversed by linearly-dispersive states whose spin directions are oriented perpendicularly relative to the momentum. These linear branches intersect each other at a so-called Dirac point (DP) forming a massless Dirac fermion[28]. Topologically-protected states residing in the bulk band gap of TIs contain counter-propagating electrons of spin-up and down directions which are protected by TRS. Bulk surface of 3D TIs is supposed to be wrapped after encountering a non-magnetic defect resulted from back-scattered electronic suppression. Such electronic suppression is mathematically formulated in eq.2, where Θ is a time reversal operator[29],

$$\Theta|\uparrow, k> = |\downarrow, -k> \qquad (2)$$

Based on the equation, spin-up electrons propagating with momentum of k are not back-scattered into another direction ($-k$), i.e. the only way of back scattering is accompanied with changing spin direction. This dependency of momentum on spin orientation or vice versa is known as spin-momentum locking of TIs prohibiting backscattered electronic motions[30].

TIs can be found in two-dimensional or three-dimensional configurations; as demonstrated in Fig.7 (a), a 2D TI is surrounded by metallic edges of counter propagating electrons; however, 2D metallic surfaces are wrapped around a 3D TI (Fig.7 (b))[13].

Moreover, 3D TIs are divided into weak and strong categories[27]; therewith, every single surface of all facet directions in strong 3D TIs represents spin-polarized robust nature; in contrast, this feature is only limited to certain or high symmetry directions of weak 3D TIs.

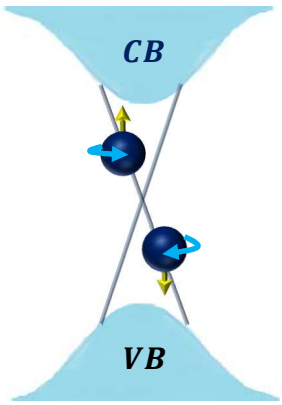

Fig.6: Schematic representation of a 3D TI; Linearly-dispersive branches connecting maximum of the VB to the minimum of the CB specifying two-dimensional illustration of topologically-protected surface states of counter propagating electrons.

Presence of topologically-protected edge/surface transport channels of 2D/3D TIs, respectively, is guaranteed via bulk-boundary correspondence. As mentioned before, as long as TKNN invariant is preserved, topological carriers are robust with respect to the deformations. However, TKNN invariant of a topological insulating system varies at the interface where non-trivial topology meets a trivial insulator for instance, vacuum. Subsequently, the energy gap of topological insulating material is closed followed by evolution of linearly-dispersive protected channels.

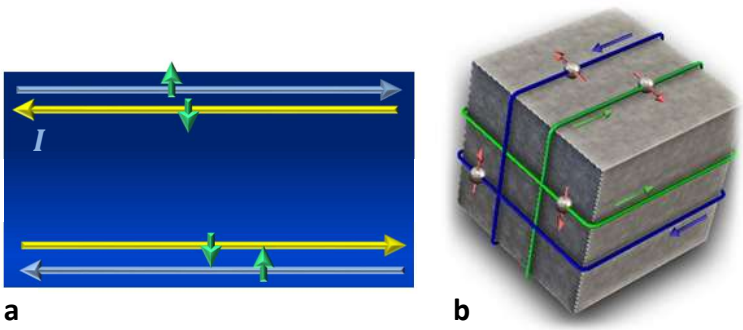

Fig.7: Schematic representation of (a) 2D and (b) 3D TI.

1.3.1. Experimental techniques

Experimental observation of topologically-protected carriers is triggered by two experimental measurement techniques of spectroscopy and transport characterization[29]. Spectroscopic measurements such as angle resolved photoemission spectroscopy (ARPES)[31-32] and scanning tunneling microscopy (STM)[23] are of potential interests for visualization of linearly-dispersive protected carriers and are considered as an effective tool of probing outstanding electronic features.

Taking advantage of ARPES visualization technique, $Bi_{1-x}Sb_x$ compound was introduced as the first candidate of 3D TIs[33]. However, complicated surface states of $Bi_{1-x}Sb_x$ prohibited further experimental investigation. Later, theoretical prediction[5] and experimental confirmation[6] of 3D TIs proceeded by simple topologically-protected surface states of Bi-based binary chalcogenides of Bi_2Te_3, Bi_2Se_3 and Sb_2Te_3 where existence of a single DP was confirmed using ARPES technique.

Besides spectroscopic measurements, governed transport mechanism of TIs is prone to be elucidated using electrical transport characterization. Therewith, indications of topologically-protected surface states of TIs are clarified by manifestation of Schubnikov-de Haas (SDH)[34-35] and Aharonov–Bohm (AB) oscillations[36-37] as well as weak anti-localization (WAL) effect[38-39]. Quantum phenomenon of AB effect can be realized by interference experiments where an electrical charge is affected by an electromagnetic potential[40]. In contrast, conductivity oscillation of material at low temperatures and strong magnetic fields reflects SDH oscillation manifesting governed quantum mechanical transport properties within the material[41]. Finally, WAL effect as one of the main focus of this work will be discussed in more details in the next section.

However, major challenge of bulk carrier dominance hinders comprehensive and clear understanding of non-trivial surface transport characterization[13]. This issue mostly results from intrinsic defects of vacancies and anti-site defects known as crystal imperfections[42]. Moreover, as in bulk crystals, the surface-to-volume ratio is typically small; electrons that contribute to the bulk band transport usually dominate over surface electrons in their quantity by orders of magnitude[13]. More importantly, position of the DP can considerably affect transport signal; as was demonstrated for Bi_2Te_3, the DP is buried beneath the VB deteriorating surface transport realization dramatically[5]. In addition, it was already proven that material exposure of O_2 and H_2O is accompanied with surface degradation along with additional bulk carrier generation[43-45].

Based on the mentioned deteriorating factors, considerable numbers of bulk carriers contributing into the whole transport signal oppose an insulating bulk channel within the material leading to lower bulk ρ. In the last few years various techniques such as compensational doping[28, 46-48] and electrical gating[49-51] were effectively implemented for bulk carrier suppression; so that, surface

carrier μ of $\sim 5800\, cm^2V^{-1}s^{-1}$ was measured for Bi_2Te_3 nanoribbon using gate voltage mechanism[52].

The reported surface contribution values into the total conductivity (σ) are still not considerable; in a $100\ \mu m$-thick Bi_2Te_3 single crystal with a maximum ρ of $\sim 12\ m\Omega cm$, only 0.3% contribution of surface carriers at $0.3\ K$ was observed[53]; *Zhi Ren et. al* reported only 6% surface states contribution to the total σ at $1.6\ K$ in a Bi_2Te_2Se material with sufficiently decreased bulk carrier density resulting from compensational doping with exceeding ρ value of $1\ \Omega cm$[54].

Due to the fact that main focus of this work is concentrated on transport characterization technique, introducing some fundamental concepts of that field will improve desirable perception and facilitate in-depth data interpretation. For that reason, concept of characteristic length is explained and based on that, relevant electronic transport regimes are introduced. In the following, details of WAL effect as an indication of topological surface transport realization is provided and mathematically discussed.

1.3.1.1. Transport regimes

To elucidate the governed electronic transport regime of the system under investigation, scaling factor of characteristic length is considered as a determinative criterion. Simply speaking, transport mechanism of a defined electronic system can be determined by comparing system dimension (L) with respect to the relevant characteristic lengths[55].

Distance of two successive collisions travelled by a charge carrier defines characteristic length of electron mean free path (l). Depending on scattering mechanism, two subgroups of elastic mean free path (l_e) and inelastic mean free path (l_{in}) are specified. In contrast, characteristic length of phase coherence length (l_ϕ) defines a distance over which the phase information of electronic wave function is preserved; in another word, electrons propagate phase coherently over distance of l_ϕ.

Based on characteristic lengths of l and l_ϕ, two transport regimes of ballistic and diffusive are represented in Fig.8. In a ballistic transport regime with precondition of $l_e > L$, electrons tunnel through the system without being scattered (Fig.8 (a)); however, for a diffusive regime ($l_e < L$), elastic scatterings are followed with random electronic diffusion (Fig.8 (b)). Depending on whether l_ϕ is smaller or bigger than l_e, classical and quantum transport regimes are defined for diffusive and ballistic transport respectively.

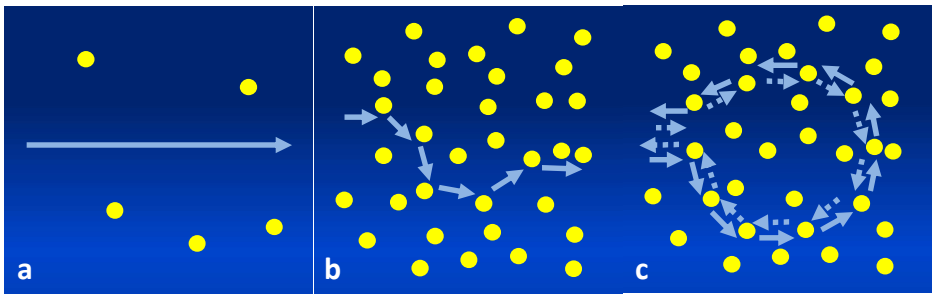

Fig.8: Schematic of (a) Ballistic, (b), Diffusive and (c) Quantum diffusive electronic transport regime in a solid (yellow circles are representative of solid impurities and blue arrows specify electron propagation trajectories[55].

1.3.1.2. Weak anti localization effect

WAL effect is an indication of quantum interference in a disordered electronic system where material ρ suddenly drops at low temperatures and small B representing a dip-like configuration (Fig.9)[55]. Presence of ρ dip in electrical transport characterization specifies evidence of strong spin orbit coupled transport within the material. According to Hikami-Larkin-Nagaoka (HLN) interference model[56], ρ dip can be interpreted as a 2D quantum interference correction known as WAL effect. More details of this model together with mathematical calculation of l_ϕ is provided in chapter.4.

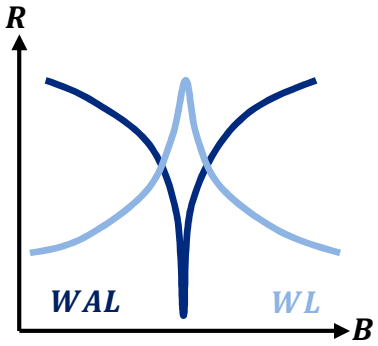

Fig.9: Schematic representation of WAL and WL effect at low temperatures.

Quantum interference of WAL effect arises from the precondition of $l_\phi > l$ specifying quantum diffusive transport regime (Fig.8 (c))[55]. As illustrated in Fig.9, by applying magnetic field of B, the ρ dip is disappeared resulting from vanishing quantum interference effect followed by TRS breakage. Basically, WAL effect is a generalization of weak localization (WL) interference phenomenon where electrons spins are neglected.

While WAL phenomenon enhances σ at low temperature regime, WL effect suppresses σ originating from electron localization of enhanced back-scattered probability of electronic wave functions; this feature represents a cusp-like configuration at small B (Fig.9).

Compared to WL effect where spin orientation is preserved, electrons spin direction of WAL effect is varied during electronic propagation through a closed loop. Electronic wave propagation in two opposite directions of a specified time-reversed loop is depicted in Fig.10. Considering closed loops of distinct geometries, spin rotation of every closed loop is exclusive. In the following interference amplitude of propagating electronic wave functions of two opposite directions in an arbitrary closed loop is calculated.

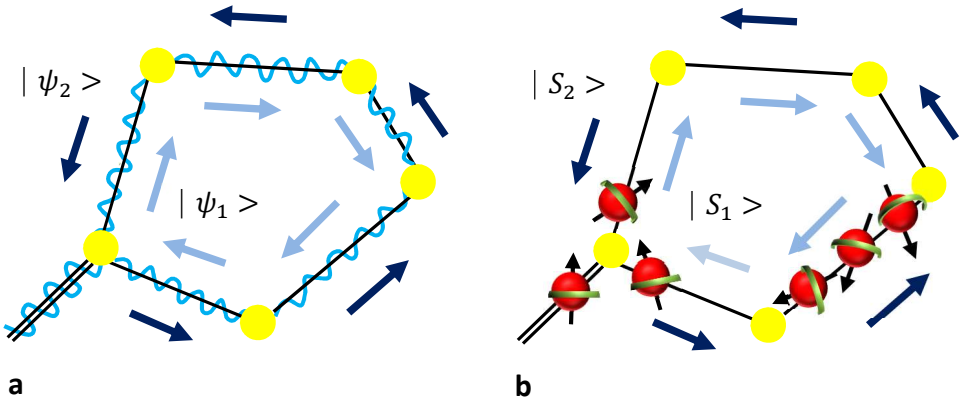

Fig.10: Schematic illustration of electron wave function interference in a closed loop resulting in (a) WL and (b) WAL effect (yellow circles represent scattering centers)[57].

According to eq.3, initial spin state of $|S1> = (a, b)$ representing spin rotation of $\frac{1}{2}$ is evolved into the final spin state of $|S2>$ where U defines a rotational matrix. The evolution of $|S1>$ for the opposite direction is given in eq.4 where $|S3>$ represents the final state,

$$|\mathrm{S2}> = U\,|\mathrm{S1}> \qquad (3)$$

$$|\mathrm{S3}> = U^{-1}\,|\mathrm{S1}> \qquad (4)$$

Rotational matrix of U consists of three rotational mechanisms of $R_z(\alpha)$, $R_y(\theta)$ and $R_z(\beta)$ which are presented in eq.5; first, $|S1>$ is rotated with Euler rotational angle of β around z-axis ($R_z(\beta)$), then

rotational process is followed by rotation of θ along y-axis ($R_y(\theta)$). Finally, spin rotation is accomplished with rotation of α around z-axis. The resulting rotational matrix of U is given in eq.6,

$$U = R_z(\alpha)R_y(\theta)R_z(\beta) = \begin{pmatrix} e^{i\alpha/2} & 0 \\ 0 & e^{-i\alpha/2} \end{pmatrix}\begin{pmatrix} \cos\theta/2 & \sin\theta/2 \\ -\sin\theta/2 & \cos\theta/2 \end{pmatrix}\begin{pmatrix} e^{i\beta/2} & 0 \\ 0 & e^{-i\beta/2} \end{pmatrix} \quad (5)$$

$$U = \begin{pmatrix} e^{i(\alpha+\beta)/2}\cos\theta/2 & e^{i(\alpha-\beta)/2}\sin\theta/2 \\ -e^{i(\alpha-\beta)/2}\sin\theta/2 & e^{-i(\alpha+\beta)/2}\cos\theta/2 \end{pmatrix} \quad (6)$$

The interference amplitude of $|S2>$ and $|S3>$ is calculated by defining expectation value of $<S2|S3>$ represented in eq.7,

$$<S2|S3> = <(U^{-1}S1)|(U\,S1)> = <S1|(U^{-1})^{+}U|S1> \quad (7)$$

Based on unitary transformation of $U^{-1} = U^{+}$, the resulting U^2matrix is calculated (eq.8),

$$U^2 = \begin{pmatrix} e^{i(\alpha+\beta)/2}\cos^2\frac{\theta}{2} - \sin^2\frac{\theta}{2} & \frac{1}{2}\left(e^{i\alpha} + e^{-i\beta}\right)\sin\theta \\ -\frac{1}{2}(e^{-i\alpha} + e^{i\beta})\sin\theta & e^{i(\alpha+\beta)/2}\cos^2\frac{\theta}{2} - \sin^2\frac{\theta}{2} \end{pmatrix} \quad (8)$$

Using eq.7 and 8, the final expectation value is provided in eq.9,

$$e^{i(\alpha+\beta)/2}\cos^2\frac{\theta}{2} - \sin^2\frac{\theta}{2} + \frac{1}{2}\sin\theta\left[a^{*}b\left(e^{i\alpha} + e^{-i\beta}\right) + c.c\right] \quad (9)$$

According to eq.9, WL and WAL specify constructive and destructive interference effects respectively. Due to the fact that no spin rotation was involved in the WL effect, α, β and θ are equal to zero, subsequently, the result of eq.9 would be equal to one indicating constructive electronic interference.

Given the fact that spin orientation of the final state is randomly distributed, only the $\sin^2\frac{\theta}{2}$ term of eq.9 will survive after averaging over all possible angles which introduces the factor of $-1/2$. Therefore, destructive interference will be the dominated interference effect of strong spin orbit coupled transport cases.

1.3.2. Nanostructured topological insulators

Nanostructured materials exhibit exclusive properties compared to the bulk counterpart originating from quantum confinement effect[58]. By reducing material dimension down to nanometer scale which is comparable to the relevant characteristic lengths, remarkable physical properties appear. TIs as a novel category of quantum materials possessing robust surface carriers are well-implemented into the concept of nanostructured material. This strategy is considered as an effective approach for topological surface carrier realization and of potential interest for electronic device application.

High surface to volume ratio of nanostructured materials promote topologically-protected carriers contribution into the whole transport signal[27, 59]; therewith, nanostructured TIs have been specified as an excellent candidate of non-trivial topology investigation. Nanowires[60] and thin films[61] revealed evidence of surface transport contribution with high reported charge carrier μ.

Physical interference effects of AB and SDH oscillations as well as WAL effect specifying evidence of surface transport contribution were already observed in various nanostructured topological insulating materials[37, 52-53, 62]. To eliminate residual bulk carriers, E_F of nanostructured TIs was electrically-tuned and constrained to the material bulk band gap using gate-voltage effect[52]. Moreover, specific transport properties of topological superconductors where nanostructured TIs are sandwiched between two superconducting materials prove versatile material application[2, 18].

More importantly, well-defined and adjustable nanoscale morphology configuration of nanostructured TIs provide well-oriented electrical trajectories which are desirable for interference-based measurement techniques[34-37].

Chapter.2

Fundamentals of thermoelectric materials

Introduction

Thermal energy dissipation is of great issue nowadays. Transformation of wasted heat into useful forms of energy could considerably reduce hazardous consequences and provide a replacement platform of current fossil fuel utilization. TE materials with capability of converting waste heat produced in vehicle exhaust or cooling systems into electricity and vice versa yet consist of any moving parts or environmentally-harmful fluid offer promising and reliable technology[63]. Potential application of TE materials in automotive[64], refrigeration[65] and aerospace industries[66] defines well-distinguished and worldwide platform which grabbed considerable attention recently.

Bi_2Te_3-based alloys[67] with ZT of around one at room temperature are considered as one of the promising TE categories. However, for industrial application, TE materials with ZT value of higher than one are desirable[68]. Therefore, low efficiency and engineering challenges of these environmentally-friendly materials hinder large potential application.

In the last two decades, different techniques of electrical and thermal transport optimization were effectively applied to resolve efficiency obstacle[69-72]. Innovative strategies of tailoring material structure with capability of ZT engineering higher than one, propelled vision of large-scale application.

The organization of this chapter is as follows. First, a brief summary of thermoelectricity and the governed working principles are provided. In the next step, different techniques of improving TE efficiency including nanostructured-based TE materials and TE nanograined bulk approach are explained and discussed in more details. Then, topologically-protected boundaries of TIs are addressed as one of the most recent techniques of TE efficiency improvement. Finally, crystalline structure of Bi_2Te_3 binary chalcogenide as key concentration of this work is provided and schematically discussed along with the most prominent material characteristics defining Bi_2Te_3 as an intriguing example of TIs and TE materials.

2.1. Thermoelectricity principles

The principles of thermoelectricity originate from Seebeck and Peltier effects discovered by *Thomas Johann Seebeck* and *Jean-Charles Peltier*, where TE materials are supposed to produce power (TE generators) or refrigerate (TE refrigerators) correspondingly[63].

Seebeck coefficient (S) specifies the amount of voltage generated per temperature gradient; in contrast, Peltier effect defines the amount of heat that can be absorbed or rejected at the interface of two dissimilar materials by driving a current in the circuit.

The efficiency of TE material is expressed in terms of dimensionless figure of merit (ZT) which is directly proportional to S and σ while, is inversely related to k (eq.10)[63],

$$ZT = \frac{\sigma S^2}{k} T \qquad (10)$$

Obviously, an efficient TE material is expected to have high S and σ as well as low k; however, finding such material is of a great challenge. Basically, TE parameters of represented in eq.10 are interrelated and cannot be easily optimized independently[73]; for instance, despite the high σ of metals, these materials are not an appropriate candidate for thermoelectricity due to their high k as well. In contrast, insulators represent low values of k and σ.

Engineering of carrier concentration (n) plays a crucial role at electrical transport optimization of TE materials. Based on eq.11 for a degenerate semiconductor, S is inversely related to n where k_B, h, e and m^* represent Boltzmann constant, Planck's constant, charge carrier and carrier effective mass respectively[74]. In contrast, σ is directly related to n (eq.12),

$$\mathrm{S} = \frac{8\pi^2 {k_B}^2}{3eh^2} \mathrm{m}^* T \left[\frac{\pi}{3n}\right]^{\frac{2}{3}} \qquad (11)$$

$$\sigma = \mathrm{ne}\mu \qquad (12)$$

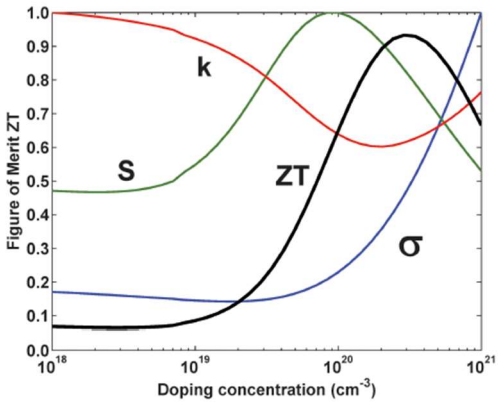

Fig.11: Schematic illustration of S, σ, k and ZT of a bulk material versus n[75].

In Fig.11, dependency of TE parameters on doping concentration is represented[74, 76]. It can be clearly seen, while low amount of doping concentration serves high S, high doping level favors high σ. Hence, desirable variation of one TE parameter is accompanied with unfavorable variation of the other factor. According to the Fig.11, highly-doped semiconducting materials with n of $10^{19} - 10^{21}$ cm^{-3} are promising candidates of efficient TE materials[74].

Heat transportation within a TE material is conducted by heat-carrying charge carriers as well as lattice vibrating phonons (eq.13); while the latter is specified as lattice thermal conductivity (k_l), the former originates from thermal contribution of electrical conductivity (k_e).

Using *Wiedmann-Franz* Law[76] given in eq.14, one can calculate k_e contribution where l_0 defines the Lorenz number,

$$k = k_e + k_l \quad (13)$$

$$k_e = l_0 \sigma T \quad (14)$$

$$k_l = \frac{1}{3}(C_v v_s \lambda_{ph}) \quad (15)$$

In contrast, k_l is defined using eq.15 where C_v, v_s and λ_{ph} are heat capacity, sound velocity and phonon mean free path respectively.

2.2. Different approaches

2.2.1. Nanostructured thermoelectric materials

Based on considerable improvement of electrical, thermal and mechanical stability of nanostructured-based materials compared to the corresponding bulk counterparts[70], these materials are of potential candidates for TE generators[77-78], TE coolers[79-80] and other fields of applications[81-82].

Historically, first generation of TE bulk materials including Bi_2Te_3, PbTe and SiGe for room temperature, intermediate temperature and high temperature applications, respectively, introduced for the first time in 1950s[74]. In the mid of 1990s, two outstanding approaches revolutionized TE society; first approach was concerned with creating complex crystalline structures[83-84] where voids (vacancies) and rattlers (heavy atoms located in the voids) of skutterudites and clathrates remarkably enhanced phonon scattering centers within the material resulting in significant k_l reduction. The other approach which is the main focus of this work was to create nanostructured TE materials[71-74, 85-86].

Discovery of nanostructured TE materials proposed for the first time by *Dresselhaus* and *Hicks* in 1993[87]. They theoretically confirmed that electronic wave function confinement in one and two dimensions was accompanied with ZT enhancement of one dimensional (1D) quantum wire and 2D

quantum well respectively. Later, theoretical and experimental proof of significant k_l reduction followed by nanostructured-based material design strategy was reported by other groups[86]; therewith, k value of $\sim 0.3 - 0.4\ Wm^{-1}K^{-1}$ was measured for Bi_2Te_3 thin films prepared by pulsed laser deposition technique which is 25% lower than in the bulk[86].

Compared to a bulk counterpart, nanostructured material exhibits completely exclusive behavior resulted from quantum confinement effect[85]. According to *Mahan-Sofo* theory[88], material size reduction down to nanometer scale is accompanied with local density of states (DOS) enhancement over a narrow energy range near E_F which is followed by S enhancement[89]. Based on *Mott* formula[90] given in eq.16, S associates with energy derivative of energy-dependent σ at E_F which is only valid for metals and highly degenerate semiconductors,

$$\mathrm{S} = \frac{\pi^2}{3} {k_B}^2 \frac{\mathrm{T}}{e} \left(\frac{d(ln\sigma(E))}{dE}\right)_{E = E_F} \tag{16}$$

$$n(E) = \mathrm{g(E)f(E)} \tag{17}$$

$$\mathrm{S} = \frac{\pi^2}{3} {k_B}^2 \frac{\mathrm{T}}{e} \left(\frac{1}{n}\frac{d(n(E))}{dE} + \frac{1}{\mu}\frac{d(\mu(E))}{dE}\right)_{E = E_F} \tag{18}$$

Using eq.12, 16 and 17, one can extract eq.18 where, $f(E)$ and $g(E)$ represent Fermi-Dirac function and DOS respectively. Based on eq.18, two energy-dependent mechanisms of $n(E)$ and $\mu(E)$ define S value. Considering $\mu(E) = \mu$, S value can be improved by local enhancement of $g(E)$. Such S enhancement was experimentally observed for zero dimensional (0D) quantum dots, 1D quantum wire and 2D quantum wells[91-92].

In addition, nanostructured TE materials benefit from considerable reduction of k_l resulting from the enhanced phonon scattering mechanism[71]; therewith, low k_l value of $0.22\ Wm^{-1}K^{-1}$ was reported for p-type Bi_2Te_3/Sb_2Te_3 superlattice[93]. Another example stands for $PbTe/PbTe_{0.75}Se_{0.25}$ superlattice with k_l value of $0.5\ Wm^{-1}K^{-1}$ Ref[94].

More importantly, interconnected TE parameters can be decoupled using nanostructured-based material design strategy; in such materials the optimized dimension is supposed to be larger than electron mean free path preserving electrical transport contribution yet, smaller than phonon mean free path suppressing heat-carrying phonon transportation[95]. For that reason, TE properties of nanostructured materials are widely improved compared to the bulk counterparts; *Venkatasubramanian et al*. reported high ZT value of 2.4 for Bi_2Te_3/Sb_2Te_3 superlattices[93], *Harman et al.* calculated ZT value of 3 for PbTe/PbTeSe quantum dot superlattices at $600\ K$[91].

However, time-consuming and expensive nano-fabrication techniques limit large-scale potential applications of nanostructured TE materials. In addition, reproduction of Bi_2Te_3/Sb_2Te_3 superlattice satisfying high ZT value of 2.4 conducted by other research groups, still remains challenging[96].

2.2.2. Nanograined bulk thermoelectric materials

Recently, persistent efforts were made to incorporate bulk fabrication techniques into nanostructured materials namely, nanograined bulk materials. Basically, the possibility of material fabrication in large quantity together with having more design flexibility favor economical and engineering considerations; therewith, low-cost material production in large quantity (kg-scale) as well as high TE performance of nanograined bulk materials grabbed considerable attention of TE society[68, 76, 97].

Nanograined bulk materials consist of isolated nano-sized grains which are separated by well-defined interfaces called grain boundaries. Surrounding grain boundaries of small dimension introduce effective phonon-scattering centers within the material resulting in dramatic k_l reduction yet, preserve electrical transport contribution[95].

The fabrication condition must trigger mechanically stable and highly efficient nanograined TE materials yet retain nanostructural configuration. However, grain boundary arrangement fulfilling all the required conditions is not that straightforward. Moreover, creating thermodynamically-stable nanograined bulk material is of a great challenge.

Nanograined bulk materials are fabricated using different bulk processing techniques such as hot pressing[68, 98] and spark plasma sintering[99, 100]. Compared to the traditional methods of sample preparation with maximum ZT value of $\sim 0.8 - 1$[101-103], these techniques offer easier fabrication method along with mechanically more stable samples. However, transition of nanograins into micro or even larger grains during sintering procedure resulting from high temperature and long compaction time[98, 104], can be regarded as a major drawback which could affect k_l destructively. Based on the previous reports, the resulted grain size distribution varies in the range of $\sim 10 - 1000\ nm$[76].

Despite of grain growth and recrystallization effect during sintering procedure of nanograined bulk materials, TE efficiency increase of $\sim 40\% - 75\%$ was observed[72].

Therewith, ZT of p-type $Bi_{2-x}Sb_xTe_3$ nanograined alloy was improved using hot pressing and ball milling techniques where maximum ZT of 1.4 was measured at $100\ °C$ which was exclusively attributed to the unique microstructural configuration offered by nanograined bulk material design strategy[68, 105]. Later, nanostructured p-type Bi_2Te_3/Sb_2Te_3 revealed ZT value of 1.56 using rapid solidification technique where k reduction of $\sim 30\%$ was observed[106].

Micro and nano-sized grain accumulation of different volume percentages within a nanograined bulk material can also be addressed as an effective design strategy of improving material TE efficiency.

Electrically- and thermally-propagating carriers are supposed to be decoupled to some extent in nano-micro-structured composite materials. While, heat-carrying phonons are most likely prone to be scattered at the interfaces of fine grains, interconnected coarse grains could provide electrically-connected trajectories which are favorable for surface transport carriers. Electrical and thermal disentanglement was experimentally observed by introducing nano-micro-structured Bi_2Te_3 composite where coarse ($\sim 1\ \mu m$) and fine ($\sim 100\ nm$) Bi_2Te_3 nanoparticles were combined by mechanical alloying and compacted using spark plasma sintering[107]; therewith, maximum ZT value of 0.66 at $323\ K$ for 60% distributed fine grains was reported. More importantly, this experiment made a strong emphasis on determinative influence of grain boundary distribution on material TE properties.

Boundary engineering is regarded as one of the effective approaches of improving material TE efficiency where thermal and electrical properties are prone to be manipulated separately[76]. To achieve low amount of k, phonons of different wavelengths must be strongly scattered; for that reason, specified characteristic lengths of defined dimension for scattering of not only short wavelength phonons but also mid- to long-wavelength heat carrying phonons are required. While short-wavelengths phonons are being scattered by incorporation of point defects within the material, mid- and long-wavelengths phonons will be scattered intensively through highly-dense interfaces of nanograined bulk material. Therefore, boundary engineering of TE materials is considered as a powerful tool of material optimization. Moreover, formation of defects, strains, pores and dislocations are potential interests of further grain boundary modification; for instance, ZT value of 1.86 at $320\ K$ was reported for $Bi_{0.5}Sb_{1.5}Te_3$ bulk alloy where highly dense defects and dislocation arrays were successfully incorporated into material grain boundaries[108].

Randomly oriented grain boundaries sophisticate phonon transport interpretation in a nanograined bulk material. As mentioned before, the grains of nano-sized dimension create effective centers of phonon scattering which can reduce k_l remarkably; however, phonon transport mechanism where interfaces specify the value of k is still not clear. One reason can be attributed to thermal boundary resistance of adjacent grain boundaries[109].

In spite of qualitative understanding of phonon transport mechanism in nanograined bulk materials, details of electronic transport are poorly understood which is considered as a great hindrance of improving TE efficiency.

2.2.3. Topological insulators and thermoelectric materials

Linearly-dispersive topological states of TIs consisting of electrons of high μ are promising candidates of improving TE performance. Recently, considerable numbers of theoretical and experimental studies were conducted to improve efficiency of TE materials taking advantage of topologically-protected boundary states[29, 110-114].

In the last few years, evidence of non-trivial topology was found in the well-known TE materials such as Bi_2Te_3, Bi_2Se_3 and Sb_2Te_3[5, 6] representing a single topologically-protected Dirac cone near Γ point of the surface BZ. Moreover, robustness of topological carriers against non-magnetic impurities and dislocations paves the way of introducing non-magnetic defects into the material leading to significant k_l reduction.

Physical properties including small band gap and heavy elements are triggered by both categories of thermoelectricity and topological insulating materials[29]; however, fulfilling common features is not adequate for defining a relation between these two categories. Heavy elements favor low k as well as strong spin-orbit interaction, which are required preconditions of having high-efficient TE material and topologically-protected states respectively[113]. In contrast, efficiency of TE materials can be improved significantly by doping mechanism; however, lightly-doped crystal structures using compensational doping are considered as great candidates of topological insulating investigation.

Recently, influence of topologically-protected boundary states on material TE properties attracted tremendous theoretical and experimental investigations; *Sun et. al.* obtained ZT of 0.63 for nanograined Bi_2Se_3 at $570\ K$ using hot pressing approach. They showed grain size reduction of down to $80\ nm$ was accompanied with electrical μ improvement of $\sim 12\ cm^2V^{-1}s^{-1}$ up to $\sim 600\ cm^2V^{-1}s^{-1}$which was not compatible with previous reports where μ decreased as a result of carrier scattering enhancement. The accompanying S reduction, in a similar fashion as in nanowires or thin films, further indicates the surface transport contribution in those bulk samples[27]. *Ryuji et. al*. theoretically investigated the influence of topologically-protected edge channel of QSH system on TE properties where ZT enhancement of low temperature regime was directly attributed to edge-dominated TE trasport[110].

Moreover, contribution of boundary states on material TE performance was studied in nanostructured TIs using multiple-channel model consisting of bulk and surface transport channels[111]; *Hinsche et. al.* studied separate influence of bulk and surface transport channels of Sb_2Te_3 film on TE properties using ab-initio calculation method[61].

However, lots of efforts should be invested on full characterization and effective utilization of those topologically-protected boundary states. To efficiently incorporate high μ surface carriers of TIs into thermoelectricity yet retain low k_l values, it is desirable to develop new strategies of further material-dimension reduction as well as innovating qualified engineering of further disorders and defects incorporation within the material[111].

2.3. Bi_2Te_3

After first discovery of Bi_2Te_3 in 1950[116], the material itself and its alloys have been widely investigated and utilized for different TE applications[117-118]. Recently, based on theoretical and experimental investigations, binary chalcogenide of Bi_2Te_3 grabbed considerable attention as an intriguing example of 3D TI[5, 6].

Bi_2Te_3 compound with narrow-band-gap of $\sim 0.13\ eV$[119] represents rhombohedral crystal structure with the space group of $D_{3d}^5(R\bar{3}m)$[120-121]. Crystal structure of Bi_2Te_3 represented in Fig.12, is made up of repeating building blocks of quintuple layers (QLs) consisting of two non-equivalent Te atoms namely $Te^{(1)}$ and $Te^{(2)}$ and Bi atoms (brown cage). Hence, each QL is made up of five monoatomic layers which are located along z-direction with sequence of $Te^{(1)}$ – Bi – $Te^{(2)}$ – Bi – $Te^{(1)}$ where every $Te^{(2)}$ atom is surrounded by six Bi atoms, however, every $Te^{(1)}$ atom is connected into three Bi atoms from one side and three $Te^{(1)}$ atoms on the other side.

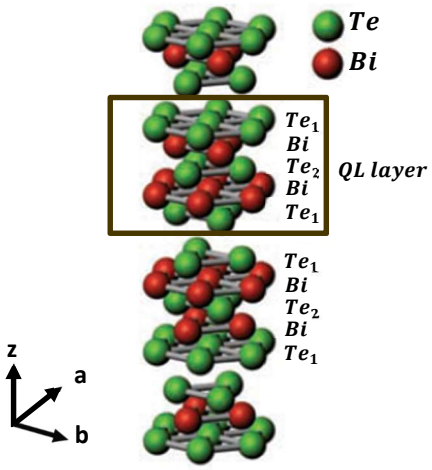

Fig.12: Bi_2Te_3 crystal structure; The building block of Bi_2Te_3 is demonstrated with a brown cage.

While QLs of Bi_2Te_3 compound are connected by weak Van der Waals forces, Bi and Te atoms of each layer are connected through covalent bonding. Due to weak Van der Waals interaction of $Te^{(1)} – Te^{(1)}$ atoms, the distance between $Te^{(1)}$ atoms is larger ($3.66\ °A$) than Bi – $Te^{(1)}$ and Bi – $Te^{(2)}$ atoms with atomic distance of $3.07\ °A$ and $3.25\ °A$ respectively. As a result of crystalline structure, one can expect preferential cleavage plane between adjacent $Te^{(1)}$ layers[121].

More importantly, the crystalline structure of Bi_2Te_3 induces anisotropic electrical and thermal properties of different crystallographic orientations[99, 122-123]. Therewith, k of Bi_2Te_3 bulk single crystalline along Van der Waals bonding direction revealed low value of $0.6\ \mathrm{W}m^{-1}K^{-1}$ compared to the corresponding value of $\sim 1.5-2\ \mathrm{W}m^{-1}K^{-1}$ along the cleavage plane[124]. Basically, anisotropy ratios of $\sim 4-7$ and ~ 2 along the cleavage plane compared to those along z-direction were measured for electrical and thermal conductivities, respectively[124]; therefore, the resulted ZT of two crystallographic directions would be different by a factor of ~ 2.

Bi_2Te_3 is known as a reliable TE material with ZT of ~ 1 near room temperature[67] which is widely utilized for TE device applications[117-118], integrated circuits and heat pumps[125]. Recently, to improve efficiency of Bi_2Te_3-based TE materials, different approaches were effectively employed including nanostructured-based material design stratrgy[93, 126-127] as well as bulk nanostructured materials[68, 97, 105, 123, 128].

Among those techniques, nanostructured bulk material has been recently believed as an effective approach of material TE optimization. For the first time, *Tang et. al.* reported ZT value of 1.35 at $300\ K$ for Bi_2Te_3 multi-layered nanostructure material fabricated by melt-spinning and spark plasma sintering[103]. In that work, layered-nanostructure morphological configuration of Bi_2Te_3 was realized as an effective factor of defining thermal and electrical transport properties. Taking advantage of defects, vacancies and grain boundaries, k_l of Bi_2Te_3 was dramatically decreased resulting from the enhanced phonon scattering mechanism[42, 68, 103, 106, 129-130]. For instance, k_l reduction of $> 60\%$ and $> 70\%$ for 5% and 4% vacancy of Bi and Te atoms, respectively, have been reported[42]. *Lan et. al.* reported k reduction of $\sim 30\%$ at $100\ °C$ which was quite stable up to $250\ °C$, for $Bi_{2-x}Sb_xTe_3$ nanograined bulk material resulting from the enhanced phonon scattering mechanism at material grain boundaries[128].

TE properties of Bi_2Te_3 nano-micro composite was dramatically affected by grain boundary distribution[107] where maximum ZT value of 0.66 at $323\ K$ was reported for 60% distributed nano-sized grains. Grain boundary engineering could also affect material ρ; for Bi_2Te_3 sample prepared by microwave assisted solvothermal method, grain size reduction of $97\ nm$ down to $51\ nm$ was followed with ρ enhancement[104].

Based on the conducted literature review, high-quality Bi_2Te_3 nanophases of well-controlled sizes and shapes resulted in further k_l reduction specifying the key importance of synthesis-based bulk nanostructured material design strategy[73, 76, 97, 122, 131-134]; therewith low k_l of $0.3\ \mathrm{W}m^{-1}K^{-1}$ has been reported for n-type Bi_2Te_3 nanoplate pellets[97]. Taking advantage of bottom-up synthesis approach, p-type Bi_2Te_3 bulk material with ZT of $\sim 1.3-1.5$ has been produced[98]. *Cao et. al.* reported ZT value of ~ 1.47 for Bi_2Te_3/Sb_2Te_3 bulk nanocomposite using hydrothermal synthesis together with hot pressing approach[129]. However, the reported ZT values of bottom-up synthesis approach are commonly less than 0.6 resulting from the bonded residual surfactant into nanoparticle surfaces followed by decreased value of carrier μ[73, 122, 131-134].

Moreover, Bi_2Te_3 is an outstanding candidate of elucidating non-trivial topology with a detected single Dirac cone of locating at Γ point of the surface BZ[5]. However, material narrow-band-gap as well as buried DP in the VB, hinder well realization of topologically-protected carriers associating with outnumber of bulk carrier transport. Recently, different tailoring approaches were effectively implemented for further surface transport realization[28, 46, 48-49, 52]; therewith, crystal structure of Bi_2Te_3 single crystal was successfully manipulated by compensational doping of $(Bi_{1-x}Sn_x)_2Te_3$ where E_F tuned to intersect only the surface carriers[28]. *Taskin et. al*. reported 70% surface transport contribution into the whole transport signal for $Bi_{1.5}Sb_{0.5}Te_{1.7}Se_{1.3}$ compound[46].

Moreover, *Xiu et. al*. reported surface carrier μ of $\sim 5800\ cm^2V^{-1}s^{-1}$ for Bi_2Te_3 nanoribbon using gate voltage mechanism[52]. In $40\ nm$-thick Na-doped Bi_2Te_3 nanoplate, surface μ and mean free path of $\sim 3400\ cm^2V^{-1}s^{-1}$ and $\sim 119\ nm$ were specified, respectively, using tunable gate voltage mechanism[49]. *Kong et. al.* reported reduced bulk carrier density of over two orders of magnitudes for $(Bi_xSb_{1-x})_2Te_3$ compound yet preserving topologically-protected features using gate voltage effect[48].

In contrast to conceptually simple topological surface states of Bi_2Te_3, chemistry of this material is always complicated. Basically, complicated defect chemistry of Bi_2Te_3 originates from anti-site defects where excess Te (Bi) elements occupy Bi (Te) lattice sites resulting in n-type and p-type dopant system correspondingly[42]. Incorporated anti-site defects are followed by having heavy effective mass which can dramatically affect material TE properties[120]. *Satterthwaite et al., Brebrick*[135] and more recently *Cho et al.*[136] proposed that Bi_{Te} and Te_{Bi} anti-site defects behave as acceptor- and donor-like atoms respectively. *Hashibon et al.* showed[120] E_F of Bi_2Te_3 compound can be tuned using anti-site defect approach where E_F is shifted toward VB and CB by excess amount of Bi and Te, respectively, resulting in an enhanced DOS near E_F.

In addition, n of Bi_2Te_3 alloys can be affected by defect chemistry; therewith, *Kim et. al.* reported an increase of n by decreasing grain surface area resulting from acceptor-like behavior of grain boundaries in B_2Te_3 bulk material[137]. Similar behavior was found in nanostructured Bi_2Te_3 bulk material where n decreased by average grain size reduction which was attributed to Bi_{Te} anti-site defects[99]. Optimized n of V_2VI_3 materials is supposed to be in order of $10^{19}\ cm^{-3}$ Ref[42], while intrinsic point defects alone are supposed to contribute in order of $10^{18} - 10^{20}\ cm^{-3}$ which can well interpret dominance of bulk carriers over surface transport of Bi_2Te_3-based materials.

Chapter.3

Methods

Introduction

In this chapter, experimental approaches of Bi_2Te_3 nanoparticle synthesis as well as compacted bulk pellet fabrication are introduced and explained in more details. Moreover, methodology principles of topologically-protected surface transport realization, TE characterization and THz time-domain spectroscopy measurement of Bi_2Te_3 compacted nanoparticles are represented.

Organization of this chapter is as follows; first, a brief overview of the applied chemical synthesis approaches of Bi_2Te_3 nanoparticle fabrication is provided. In the following, experimental details of Bi_2Te_3 compacted nanoparticles fabrication, sample contacting along with working principles of transport characterization setup are provided and discussed in more details. Besides that, methodology principles of TE characterization including ρ, S and k measurements are introduced. Finally, a brief overview of THz time-domain experimental setup is provided.

3.1. Synthesis of Bi_2Te_3 nanoparticle

In the last few years, different approaches of solution-based[131, 138-139] and gas-phase-based processes such as atomic layer deposition (ALD)[132-133], metal organic chemical vapor deposition (MOCVD)[134, 140] and physical vapor deposition (PVD)[141-142] were widely utilized for synthesis of highly stoichiometric and phase-pure binary Bi_2Te_3, Bi_2Se_3, Sb_2Te_3 and Sb_2Se_3 and ternary $(Sb_xBi_{1-x})_2Te_3$ compounds. A particular drawback of solution-based synthesis of Bi_2Te_3 and Bi_2Se_3 which were studied over the past decade[143-144] is the formation of Bi-rich phases due to the incorporation of additional bilayers into tetradymite-type layered materials[73]. In this work chemist partners from University of Duisburg-Essen developed a new synthesis strategy using well-defined Bi-containing ionic liquids (ILs). These precursors are not only robust to withstand various temperature conditions but also highly reactive in reaction with $E(SiEt_3)_2$ (E = Se, Te) precursors[73].

Depending on presence or absence of capping agent of oleylamine (OA) during chemical synthesis approach, Bi_2Te_3 nanoparticles of completely distinct morphological configuration were fabricated.

Therewith, in the following two different categories of classical and developed approaches followed by presence and absence of chemical compound of OA, respectively, are introduced.

3.1.1. Classical approach

$3.4\ g$ ($3.9\ mmol$) of $[C_4C_1Im]_3[Bi_3I_{12}]$ was dissolved in $10\ mL$ of $[C_{4mim}]I$ with $3\ mL$ of oleylamine (OA) in a centrifuge tube. The mixture was stirred for $1\ h$ at $100\ ^{\circ}C$. $1.24\ g$ ($3.47\ mmol$) $(Et_3Si)_2Te$ were added dropwise and the resulting black suspension was stirred at $150\ ^{\circ}C$ for $12\ h$. The resulting colloidal solutions were centrifuged ($2500\ rpm$), washed with $6 * 15\ mL$ acetonitrile and $2 * 15\ mL$ chloroform, and dried at room temperature under vacuum. The whole synthesis procedure was performed under an inert atmosphere condition. The corresponding chemical reaction is given in eq.19,

$$[C_4mim]_3[Bi_3I_{12}] + (Et_3Si)_2Te \xrightarrow[OA,\ [C_4mim][I]]{150\ ^{\circ}C,\ 12h} Bi_2Te_3 \qquad (19)$$

3.1.2. Developed approach

$3.5\ g$ ($1.4\ mmol$) $[C_4C_1Im]_3[Bi_3I_{12}]$ were dissolved in $10\ mL$ of $[C_4C_1Im]I$ under inert conditions. The ionic liquid mixture was stirred at $100\ ^{\circ}C$ for $1\ h$ and was then cooled to room temperature. $1.9\ g$ ($5.6\ mol$) $[C_4C_1Pyr][TeSiEt_3]$ were added to the resulting red solution, yielding a black suspension which was further stirred at $150\ ^{\circ}C$ for $1\ h$. A black precipitate was obtained, which was then isolated by centrifugation and repeatedly washed with $20\ mL$ of acetonitrile ($6 *$). The isolated solid was dried in vacuum at ambient temperature. Yield: $1100\ mg$ (73% of theoretical yield). The whole synthesis procedure was performed under an inert atmosphere condition. The corresponding chemical reaction is given in eq.20,

$$[C_4mim]_3[Bi_3I_{12}] + [C_4C_1Pyr][TeSiEt_3] \xrightarrow[[C_4mim][I]]{150\ ^{\circ}C,\ 4h} Bi_2Te_3 \qquad (20)$$

3.2. Sample preparation

Bi_2Te_3 bulk samples were fabricated using hot pressing approach. To fulfill all the required conditions which are desirable for efficient TE characterization and better surface transport realization, nanoparticle-based Bi_2Te_3 sample processing plays a crucial role.

Aiming at Bi_2Te_3 bulk sample fabrication, high-quality Bi_2Te_3 nanoparticles of two different chemical approaches were compacted using table press produced by Specac design company (Fig.13 (a)).

To fabricate nanoparticle-based Bi_2Te_3 sample, $\sim 0.07\ g$ Bi_2Te_3 nanoparticles were compacted for 90 minutes at a specific temperature in the range of $170 - 300\,^{\circ}C$ using a $5\ mm$ metal die (Fig.13 (b)-(c)) under an inert atmosphere condition. Depending on the applied temperature during compaction procedure, pellets of different thickness and degree of compaction were fabricated. It is worth to mention that the whole hot-pressing setup was incorporated into a glove box system to avoid surface oxidation.

To fabricate a mechanically-stable Bi_2Te_3 sample, yet preserve nanostructured morphology configuration different sintering parameters including applied temperature, pressure and compaction time were optimized. More importantly, to have stable Bi_2Te_3 bulk pellets, the amount of Bi_2Te_3 nanoparticles (m) optimized so that Bi_2Te_3 bulk pellets of lowest possible thickness were produced. More details of optimized pressing parameters are provided in chapter 4.

Fig.13: (a) Hot pressing device. (b) Metal Die of covered with a heating jacket. (b) Accurate temperature measurement was triggered by a thermocouple tool that was placed in the hole represented by a red circle.

Compaction parameters are determinative factors defining material properties where surface and bulk transport channels are significantly affected by these parameters; if nanoparticles are compacted at low temperatures, they are not in a good contact; hence, carrier propagation is hindered. In contrast, if nanoparticles are sintered at too high temperatures, the crystallinity of the

interfaces improves and therewith less interfaces as energy barriers are provided; subsequently, bulk metallic transport is expected to dominate surface signal. Moreover, nanoparticle compaction at high temperature for a long time leads to undesirable growth of grain boundaries resulting in reduced amount of phonon scattering centers. However, a balance between temperature and compaction time can significantly reduce undesirable grain growth procedure.

Fig.13 (b)-(c) specifies the $5\ mm$ metal die where Bi_2Te_3 nanoparticles were compacted. To avoid sample contamination during compaction procedure, Bi_2Te_3 nanoparticles were covered with tungsten foils from both sides. After 90 minutes of nanoparticle compaction followed by ~ 2 hours of cooling procedure, the resulted Bi_2Te_3 bulk pellet was removed from the metal die. The applied temperature was provided by an external heating system. The measured temperature by the external heater was different from the one measured at the compaction spot resulting from unavoidable heat loss. Aiming at accurate temperature measurement, a hole was incorporated into a metal die where Bi_2Te_3 nanoparticles were compacted (red circle in Fig.13 (c)).

3.2.1. Density measurement

Based on eq.21, density of Bi_2Te_3 compacted nanoparticles were defined followed by mass and volume measurements. In this equation, m, d and t represent mass, diameter and thickness of the Bi_2Te_3 compacted pellet respectively,

$$\rho = \frac{m}{\pi\left(\frac{d}{2}\right)^2 t} \qquad (21)$$

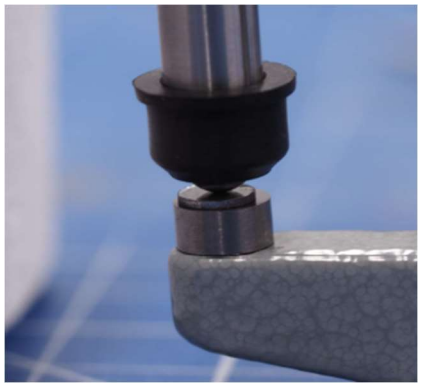

Fig.14: thickness measurement of Bi_2Te_3 compacted pellet.

As shown in Fig.14, thickness measurement of Bi_2Te_3 compacted pellet was conducted using a digital micrometer with an additional ball equipment on the top.

3.3. Contacting

To have an accurate electrical transport measurement, sample contacting is of key importance. For that reason, progress of contacting procedure is explained in the following. Sample contacting was performed using two different approaches. First, lithography followed by soldering technique was employed to establish promising electrical contacts. Later, Bi_2Te_3 samples were directly contacted using a metallic probe setup.

3.3.1. First approach

In the first approach, Bi_2Te_3 compacted pellet was mounted on a silicon substrate using soldering technique. In this section, first more details of substrate preparation is provided using lithography approach followed by sample mounting onto the predefined substrate using soldering technique.

3.3.1.1. Substrate preparation

Photolithography or optical lithography is a famous microfabrication technique in which the desired pattern is constructed on a substrate up to nanometer resolution accuracy[145]. In this technique, a predefined pattern is established on a light-sensitive polymer known as photoresist which is exposed during lithography procedure. The schematic illustration of the whole process is represented in Fig.15.

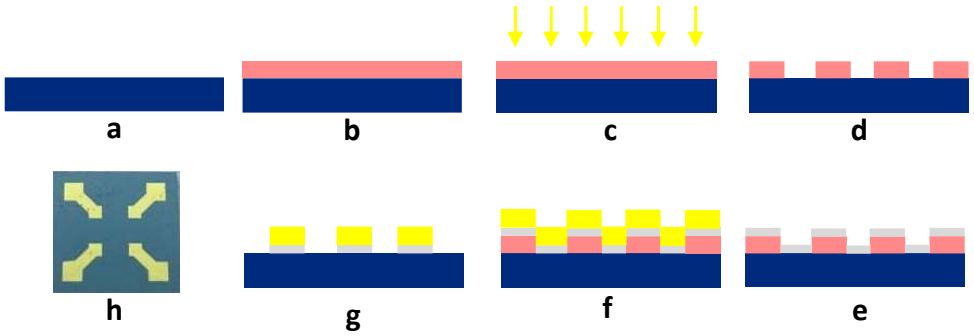

Fig.15: Substrate fabrication, (a) Silicon substrate. (b) Spin-coated photoresist on silicon substrate. (c) UV exposure. (d) Removing exposed area using developer. (e) Cr sputtering. (f) Gold sputtering. (g) Removing photoresist. (h) Final substrate.

In the first step adhesion layer of TIPRIME was spin coated on a silicon substrate (Fig.15 (b)); subsequently, the coated substrate was heated on a hot plate with the applied temperature of $120\,^{\circ}C$ for two minutes.

In the next step, photoresist of AZ5214E was coated on the substrate followed by heating procedure of $90\,^{\circ}C$ for four minutes. Then, the predefined pattern represented in Fig.15 (h), was patterned on the spin coated substrate using MLA 100. Depending on the coated photoresist, the exposed area of the substrate is removed or remained after exposure for positive and negative photoresist respectively[145]. In this work positive photoresist was utilized; hence, as demonstrated in Fig.15 (d), developer of AZ726 removed photoresist of the exposed regions in Fig.15 (c). To establish gold conducting paths, first, $50\,nm$-thick adhesion layer of Cr was sputtered on the substrate (Fig.15 (e)), followed by sputtering of $400\,nm$-thick gold layer (Fig.15 (f)). Finally, as shown in Fig.15 (g), by immersing the substrate into the remover the desired pattern appeared.

3.3.1.2. Sample mounting

In this step, the compacted Bi_2Te_3 sample was mounted onto the substrate using Indium-Tin (InSn) soldering contact. As demonstrated in Fig.16 (a), small amount of InSn was mechanically soldered on top of the gold square contacts. For that purpose first, silicon substrate was heated on a hot plate with the applied temperature of $120\,^{\circ}C$ for 5 minutes; subsequently, InSn was delicately soldered on the defined areas.

To avoid surface oxidation, sample was mounted on the substrate inside the glove box. Therewith, the represented substrate in Fig.16 (a) was heated up to temperature of $120\,^{\circ}C$ on a hot plate for 5 minutes inside the glove box; subsequently, molten-InSn contacts paved the way of delicate sample adjustment onto the substrate.

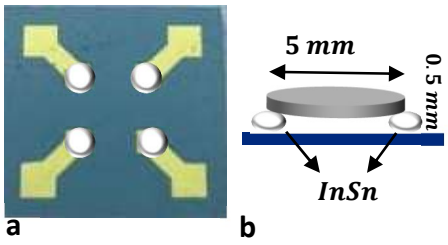

Fig.16: (a) Top view and (b) Side view of soldered InSn on a silicon substrate.

3.3.2. Second approach

Sample contacting using first approach is limited in some important aspects. First of all, the whole procedure of substrate preparation, soldering and sample mounting take some time. More importantly, the substrate with a mounted sample on top was bonded to a DynaCool puck using Bonding machine which made the procedure longer and more complicated.

In addition, side-coverage of some of the compacted pellets with InSn during sample mounting was inevitable.

To avoid such constrains, sample was directly contacted using a metallic probe setup. As demonstrated in Fig.17, the setup consists of four Copper Beryllium probes whose adjustment is feasible by an implemented screw on the top. To avoid sample breakage during screw adjustment, each Copper Beryllium probe offers a spring-like flexibility so that the applied pressure can be controlled significantly.

Compared to the first approach, this method facilitates and improves sample contacting dramatically. The possibility of direct contacting of the fabricated samples to the Copper Beryllium probe setup without utilizing any additional soldering substance offers more accurate and reliable electrical transport measurement which can considerably save time as well.

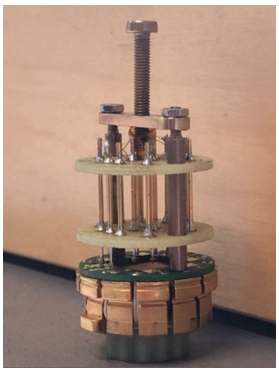

Fig.17: metallic contact probe.

3.4. Electrical transport characterization

Electrical transport properties of the compacted Bi_2Te_3 bulk pellets were characterized in a Physical Property Measurement System (PPMS) of the DynaCool series from Quantum Design. Based on Van der Pauw (VdP) configuration approach which was applied for transport characterization, physical properties of Bi_2Te_3 compacted nanoparticles were investigated.

3.4.1. Van der Pauw configuration

VdP method is one of the famous characterization techniques which is widely used in semiconductor industry. According to VdP calculation, specific resistivity and Hall voltage of an arbitrary shape consisting of any isolated hole, homogeneous in thickness with sufficiently small contacts can be identified[146]. Samples of quite small $\frac{t}{d}$ ratio are desirable for this method, where t and d specify thickness and diameter of the sample under investigation respectively.

Given the fact that there was no other accessible method for the transport characterization of not fully-dense Bi_2Te_3 bulk samples, VdP configuration method was applied in this work.

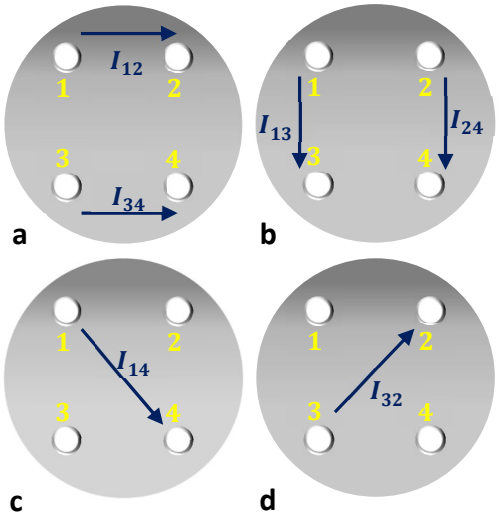

Fig.18: Schematic representation of VdP configuration for measuring (a)-(b) longitudinal resistance and (c)-(d) Hall resistance.

Fig.18 represents a schematic illustration of VdP configuration. According to the figure, four small contacts are placed at four corners of the Bi_2Te_3 compacted pellet. In VdP configuration voltage can be measured by flowing current of I_{ij} between every two contacts of i and j respectively. Depending on measuring longitudinal resistance (R_{xx}) or Hall resistance (R_{xy}), current direction is different. To measure R_{xx}, current is flown through the square edges (Fig.18 (a)-(b)) while, for measuring R_{xy}, current flow is conducted through the square diameters (Fig.18 (c)-(d)).

Based on VdP formula given in eq.22, sheet resistance of R_S was measured; two characteristic resistance of R_A and R_B represent the average resistance of two measurement directions (eq.23). Sample ρ was calculated using eq.24 where t defines sample thickness,

$$e^{(\frac{-\pi R_A}{R_S})} + e^{(\frac{-\pi R_B}{R_S})} = 1 \quad (22)$$

$$R_A = \frac{(R_{12}+R_{34})}{2}, R_B = \frac{(R_{13}+R_{24})}{2} \quad (23)$$

$$\rho = R_S t \quad (24)$$

Based on Hall VdP configuration (Fig.18 (c)-(d)), carrier concentration (n) and mobility (μ) of Bi_2Te_3 compacted nanoparticles were estimated using eqs.25-26; d, e and ρ represent sample thickness, electron elementary charge and sample resistivity at zero magnetic field respectively.

$$\mathrm{n} = \frac{B}{R_S e d} \quad (25)$$

$$\mu = \frac{1}{\rho e d} \quad (26)$$

3.4.2. Electrical instruments

3.4.2.1. Dynacool

DynaCool measurement system is of great interest for specifying physical transport properties where a precise control over sample condition is offered during measurement procedure. This measurement setup is known as second generation of PPMS which is fabricated by Quantum Design. Compared to the first generation, DynaCool systems take advantage of not using liquid cryogens which was utilized for cooling superconducting magnet and temperature control system. Therewith, low vibrational environment for sample measurement is feasible using DynaCool system. It is worth to mention, for cooling superconducting magnet as well as temperature control of DynaCool system only little amount of liquid Helium-4 is required. In addition, the possibility of creating high vacuum of less than $10^{-4}\ Torr$ in around 10 minutes using an integrated cryopump improves quality of the electrical transport measurement.

Material physical properties can be elucidated at temperature range of $1.8 - 400\ K$ using DynaCool system. Moreover, the system is designed to perform B-dependent measurements where the amount of B can be sweeped up to $16\ T$ in two different directions. In addition, the possibility of B rotation during the measurement facilitates further physical investigations. Delicate temperature and B adjustment of DynaCool system is highly demanding for different measurement setups.

To start with the electrical transport measurement, sample was mounted in the middle of a DynaCool puck. The electrical puck consists of three different channels where only two channels are commonly used for electrical transport option (ETO).

ETO performs based on lock-in technique where amplitude and phase angle of an oscillating electrical signal can be measured simultaneously. Phase angle is a determinative factor defining the angle difference between the excitation signal and corresponding oscillating response of the sample. In this work the amount of phase angle was optimized to less than one specifying ignorable influence of inductive and capacitive effects.

For standard four-point measurement, each channel of DynaCool puck consists of four gold pads of $I+$, $I-$, $V+$ and $V-$ ($+$ and $-$ specify input and output directions respectively); by passing current from $I+$ to $I-$, voltage drop can be estimated between $V+$ and $V-$ correspondingly. To avoid negative resistance, polarity of voltage probes must be observed.

Electrical and thermal transport properties of different kinds of materials can be investigated using relevant DynaCool transport option. Depending on measurement purpose, two characterizations of ETO and Thermal Transport Option (TTO) can be performed using DynaCool measurement system. Due to the fact that electrical transport characterization of this work was conducted using ETO, more details of this transport option are provided in the following.

3.4.2.1.1. Electrical Transport Option

Electrical transport parameters of the sample under investigation can be optimized using ETO of DynaCool system. This option offers possibility of resistance measurement over the defined temperature and B regime as well as current-voltage characterization.

Depending on sample ρ, ETO is expected to perform 2/4-point configuration measurements. For samples whose resistance is below $10\ M\Omega$, 4-wire configuration is applicable while for samples with resistance above $10\ M\Omega$ up to $5\ G\Omega$ 2-wire configuration is recommended.

Hall measurement is also feasible using ETO where voltage probes are placed vertically. However, due to some inevitable measurement errors, R_{xx} contribution is always incorporated into R_{xy}.

To have a precise measurement, transport parameters of ETO must be optimized. Therewith, resistance of 10 measurement points was optimized at different temperatures. Aiming at optimized resistance variation of those measurement points, electrical transport parameters of amplitude, voltage range and frequency were delicately optimized. More importantly, phase angle values were observed during measurement to fulfill the desired requirement of $< 1^{\circ}$. Finally, values of $\sim 1\ mA$, $44 - 440\ \mu V$ and $\sim 0.1 - 3\ Hz$ were identified for amplitude, voltage and frequency range respectively.

3.4.2.2. Switch box

Considerable improvement in electrical transport characterization was achieved using electrical instrument of switch box (Fig.19).

The automatic possibility of contacts switching during electrical transport measurement prohibits simultaneous measurement of VdP configurations. More importantly, cross talk between different channels can be avoided so that accuracy and reliability of the transport characterization improves significantly.

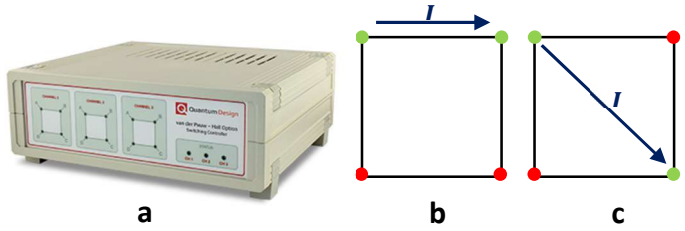

Fig.19: (a) Switch box device. Schematic representation of (b) Longitudinal resistance and (c) Hall resistance measurement of switch box (green lights of switch box represent the applied current direction).

3.5. Thermoelectric characterization

3.5.1. Direct 4-contact measurement device

To characterize ρ and S of Bi_2Te_3 bulk samples, a direct 4-contact measurement device (LSR platform) was utilized (Fig.20) effectively. Basically, TE properties of solid materials can be characterized up to maximum temperature of $1500\,^{\circ}C$ using Linseis LSR-platform. Moreover, low-temperature TE characterization down to $-100\,^{\circ}C$ is also feasible using liquid Nitrogen.

In this work ρ and S of Bi_2Te_3 compacted nanoparticles were characterized in the temperature range of $30\,^{\circ}C$ up to $240\,^{\circ}C$. Principles of S and ρ measurements using LSR characterization device is explained in more details in the following.

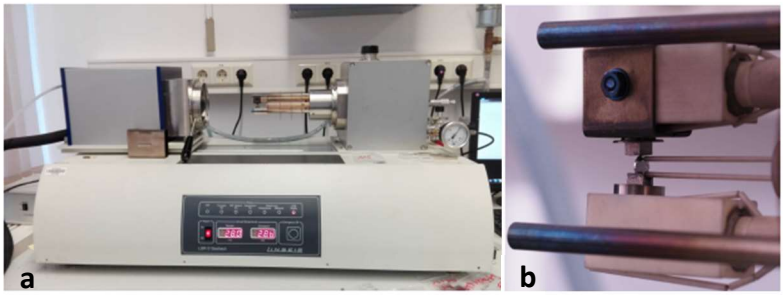

Fig.20: (a) LSR setup. (b) Sample adjustment for In-plane characterization.

3.5.1.1. Seebeck measurement

To start with S measurement, sample was placed vertically between two conducting electrodes of LSR device as demonstrated in Fig.20 (b). The schematic illustration of the whole setup is provided in Fig.21 (a).

To heat the sample, the whole setup was placed in a furnace (Fig.20 (a)); as soon as the sample temperature was reached to a certain value which was already defined in the heating program, a predefined temperature gradient of ΔT was created through the sample. Two electrodes represented on the top and bottom measure the amount of ΔT.

Practically, by applying ΔT, ΔV can be measured by two side-thermocouples as represented in Fig.21 (a), subsequently, sample S can be identified using eq.27,

$$S = \frac{\Delta V}{\Delta T} \qquad (27)$$

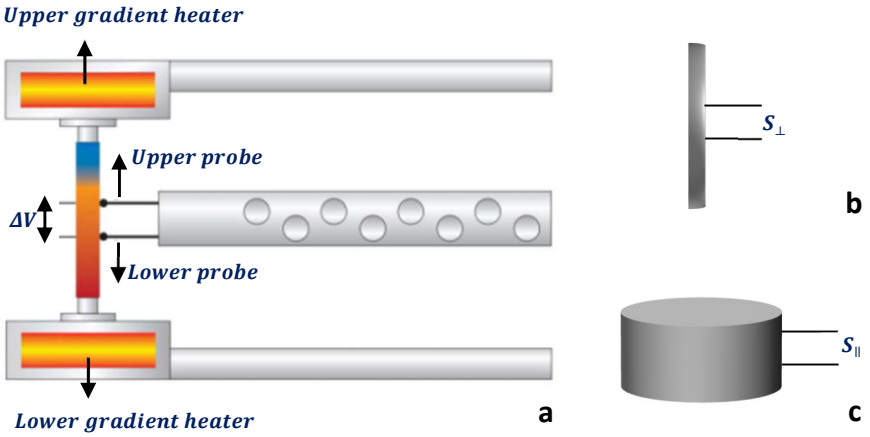

Fig.21: (a) Schematic illustration of Seebeck measurement setup of LSR device. (b) In-plane Seebeck measurement. (c) Cross-plane Seebeck measurement.

In-plane (⊥) and cross-plane (||) orientations are associated with perpendicular and parallel directions relative to the vertical pressing direction respectively. Depending on sample adjustment, $S_{||}$ and $S_\perp$ of different crystallographic orientations can be measured; as demonstrated in Fig.21 (b)-(c), ΔT is applied through and across the sample correspondingly, subsequently, $S_\perp$ and $S_{||}$ can be identified respectively. Due to the limited amount of Bi_2Te_3 initial powder, in-plane S characterization was triggered in this work.

3.5.1.2. Resistivity measurement

The schematic illustration of ρ-measurement setup is represented in Fig.22 where sample ρ can be specified using ohm's law. First, one dimensional current was provided by upper and lower electrodes under thermal equilibrium condition; subsequently, voltage drop of certain length (t) was measured using side-contact thermocouples. The distance of two thermocouples was measured before starting the characterization.

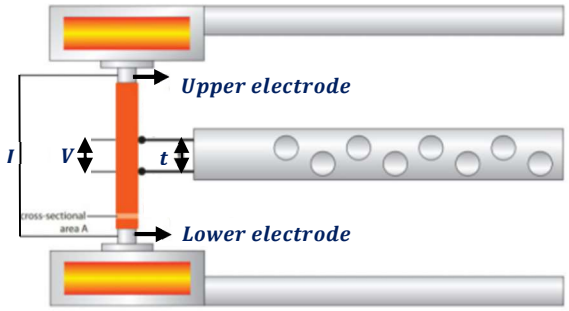

Fig.22: Schematic illustration of resistivity measurement setup of LSR device.

3.5.2. Laser flash method

k of Bi_2Te_3 compacted pellets was defined in two different crystallographic orientations in the temperature range of $30\,^{\circ}C$ up to $240\,^{\circ}C$ using a laser flash characterization device (Fig.23). Base on eq.28, k of the compacted sample was calculated where α, ρ and C_p are thermal diffusivity, density and specific heat capacity of the Bi_2Te_3 compacted pellets respectively,

$$k = \alpha \rho C_p \qquad (28)$$

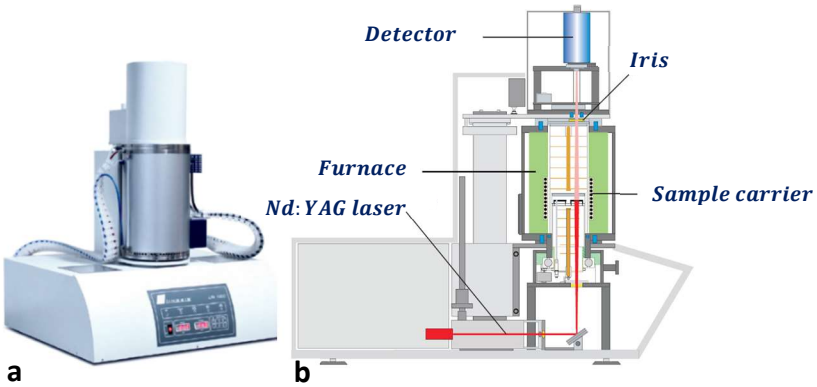

Fig.23: (a) LFA setup. (b) Schematic illustration of LFA setup.

As demonstrated in Fig.23 (b), the device consists of three main parts of detector on the top, sample carrier in the middle and laser flash (heat source) on the bottom where sample was exposed by laser flash from the bottom during measurement time.

Depending on laser beam collection, in-plane and cross-plane measurement of k is feasible. For cross-plane measurement, center of the pellet was exposed; subsequently, reflected beam was collected by the detector. However, the reflected beam of in-plane measurement was collected from sample edges. The corresponding sample holders of in-plane and cross-plane measurements are shown in Fig.24. While cross-plane holder contains an empty hole exactly at the center, the reflected beam of in-plane measurement can be collected from the surrounding grooves.

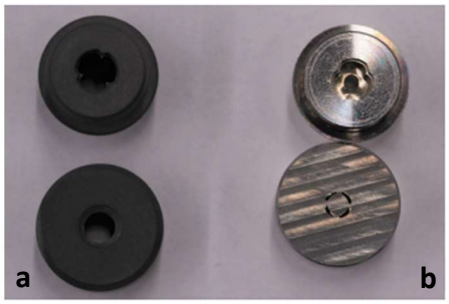

Fig.24: (a) Cross-plane and (b) In-plane sample holder of k characterization.

To have an accurate measurement, different parameters of predefined heating program were delicately optimized. Depending on the sample and type of the measurement (in-plane or cross-plane), parameters of laser pulse energy, pulse duration, Iris and amplifier are necessary to be optimized. In this work, laser power of $300\ W$ with pulse length of $2\ ms$ was considered for cross-plane measurement. Moreover, Iris and amplification were set as 4 and 20 respectively. However, for in-plane characterization higher laser power value of $350\ W$ as well as amplification of 50 were defined. The number of measurements at each specific temperature of cross-plane and in-plane measurements were set to 5 and 8 respectively.

3.6. THz time-domain spectroscopy

Detailed realization of topological surface carriers of the nano bulk Bi_2Te_3 material was performed by the THz team at University of Duisburg-Essen using a commercial THz time-domain system in reflection geometry. At the sample position, the THz spot size is about $1\ mm$ for frequencies of $1\ THz$ and above, for lower frequencies the spot size was increased according to the wavelength.

The sample was mounted next to a gold mirror that served as the reference, in a closed cycle cryostat to vary the temperature in the range of $4 - 300\ K$. Z-cut quartz windows limits the upper frequency of the measurement to about $3\ THz$. Sample and reference mirror were mounted behind apertures with a diameter of $3\ mm$, limiting the lower threshold to about $0.7\ THz$ resulting in reliable measurement. Multiple measurements were taken on different days and averaged to minimize the noise of the resulted data so that the observed features were well reproducible.

Chapter.4

Results of electrical transport characterization

Introduction

In this chapter electrical transport characterization of Bi_2Te_3 compacted nanoparticles of two different chemical approaches (classical and developed synthesis routes) are represented and discussed in more details. First, an overview of the investigated samples along with the corresponding optimized sintering parameters is provided. In the next step, results of electrical transport characterization of Bi_2Te_3 bulk pellets fabricated from classical synthesis approach are represented and discussed in more details, followed by developed synthesis route.

Organization of each approach is as follows. First, dominant transport mechanism of different samples compacted from each nanoparticle batch was investigated analyzing temperature-dependent ρ. Taking advantage of B sweep measurement, $M\rho$ and Hall resistance of the samples were investigated followed by phase coherence length (l_ϕ), carrier concentration (n) and mobility (μ) calculations. Morphological analysis including scanning electron microscopy (SEM), atomic force microscopy (AFM), Conductive-AFM and transmission electron microscopy (TEM) were effectively employed for in-depth data analysis. Finally, the conclusion was accomplished with results of THz-time-domain spectroscopy conducted for Bi_2Te_3 compacted nanoparticles of second chemical approach.

4.1. Sample overview

A list of selected electrically-investigated Bi_2Te_3 samples of two different approaches is provided in table.1. According to the table.1, pressure of $2\ kN$ was applied to compact Bi_2Te_3 nanoparticles for 90 minutes compaction time. Depending on the applied temperature, Bi_2Te_3 bulk pellets of distinct thickness (d) and degree of compaction (density) were fabricated; therewith, relative densities (ρ') of 47% up to 99% for the applied temperature of $170\ ^\circ C$ up to $320\ ^\circ C$ with constant pressure of $2\ kN$ were realized respectively. The ρ' values were calculated with respect to density of Bi_2Te_3 bulk material which is $\sim 7.7\ gcm^{-3}$ Ref [147].

According to the table.1, measured temperature of different samples at the spot where nanoparticles were compacted (T_2) was different compared to the heater value (T_1) originating from heat loss through the metal die and connecting cables. It is worth to mention, compaction time of 90 minutes was considered with respect to the time where T_2 value was achieved.

Due to the fact that accurate temperature measurement of T_2 was achieved during the sample processing of this work, this information was missing for some samples and compaction time was considered with respect to T_1 value.

The selected samples were contacted using InSn and Copper Beryllium probes.

Table.1: list of selected Bi_2Te_3 compacted bulk pellets and corresponding optimized parameters of compaction procedure.

Batch name	Sample name	$m \pm 0.001$ (mg)	$d \pm 0.001$ (mm)	T_1 ($^{\circ}C$)	T_2 ($^{\circ}C$)	$Density$ (gr/cm^3)	ρ' (%)	cotact
SS2	SS2-01	69.8	0.99	170	_	3.6	47	Metal probe
	SS2-02	72.7	0.66	280	_	5.6	72	Metal probe
	SS2-03	61.3	0.50	320	310	6.2	81	InSn
	SS2-04	62.7	0.50	320	312	6.4	83	Metal probe
	SS2-05	75	0.59	320	307	6.5	84	Metal probe
SS22	SS22-01	80.2	0.62	170	_	6.6	85	InSn
	SS22-02	74.8	0.50	300	_	7.6	99	Metal probe
	SS22-03	45.9	0.31	300	295	7.5	98	Metal probe
	SS22-04	52.7	0.37	300	290	7.2	94	–

4.2. Classical synthesis approach

4.2.1. Powder characterization

In this section, electrical transport properties of Bi_2Te_3 bulk samples which were compacted from SS2 nanoparticle batch is represented and discussed in more details.

Morphological analysis of initial SS2 Bi_2Te_3 nanoparticles is illustrated in Fig.25; as represented in Fig.25 (a) SEM image elucidates highly-agglomerated Bi_2Te_3 nanoparticles which are randomly distributed. High-resolution TEM (HR-TEM) analysis of SS2 powder revealed atomic lattice fringes with a lattice spacing of $\sim 0.2\ nm$ proving high-crystalline quality of synthesized Bi_2Te_3 nanoparticles (Fig.25 (d)). As demonstrated in Fig.25 (c), the calculated thickness value of each QL of $1\ nm$ was estimated for Bi_2Te_3 single particle which agrees very well with literature values[73].

However, red arrow of Fig.25 (d) specifies some trace of contamination surrounding Bi_2Te_3 nanoparticle. Based on the conducted infrared spectroscopy (IR) spectra of Bi_2Te_3 nanoparticles small

trace of OA contamination which was used as capping agent during synthesis procedure (eq.19), was detected (Fig.26). In addition, as will be discussed later, presence of Te nano-rods as represented in Fig.25 (b) is considered as a drawback of classical synthesis approach.

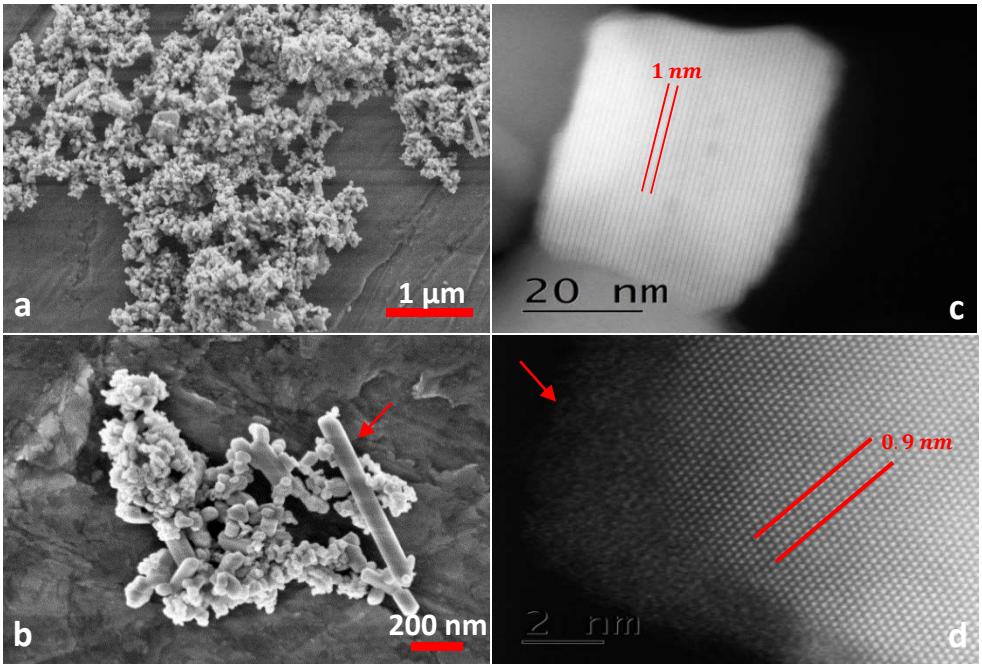

Fig.25: (a)-(b) SEM images of agglomerated SS2 Bi_2Te_3 nanoparticles; (red arrow of Fig.25 (b) illustrates evidence of Te nano-rod). (c)-(d) TEM images of single Bi_2Te_3 nanoparticle.

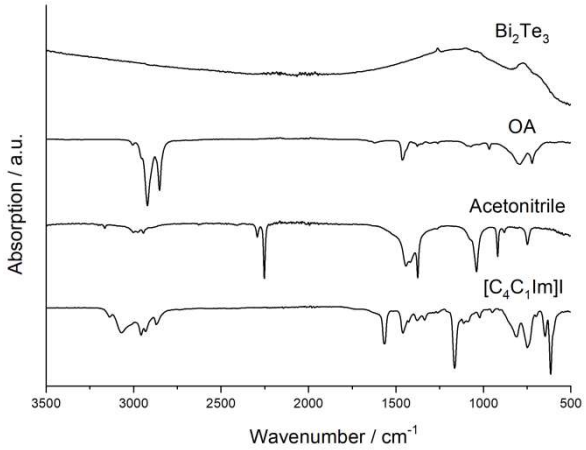

Fig.26: IR spectra of Bi_2Te_3 nanoparticles via classical approach showing absorption signal from small traces of OA contamination.

4.2.2. Temperature dependent resistivity

Thermally-activated bulk carriers of Bi_2Te_3 compacted pellets are supposed to be gradually suppressed followed by temperature reduction mechanism promoting topologically-protected surface transport contribution; therewith, resistance of Bi_2Te_3 compacted nanoparticles was measured over temperature range of $300 - 1.8\,K$ using VdP configuration. Subsequently, longitudinal resistivity (ρ) of five SS2 compacted samples with distinct density values (table.1) was calculated using eq.24; corresponding results of transport characterization are demonstrated in Fig.27.

Depending on the sample density, temperature dependent ρ of SS2 compacted nanoparticles relies on different transport mechanisms; as demonstrated in Fig.27 (a), ρ of SS2-01 and SS2-02 samples increases with decreasing temperature representing semiconducting-like behavior which is usually unexpected for samples of high carrier density which will be discussed later. However, a different transport mechanism is governed by increasing sample density; as shown in Fig.27 (a), ρ of SS2-03 sample increases with decreasing temperature down to $\sim 200\,K$ where the maximum ρ value of $\sim 7.5\,m\Omega.cm$ was achieved. By further temperature reduction down to $\sim 30\,K$, ρ reduces representing metallic transport behavior associating with weaker phonon scattering mechanism of low temperature regime[148]. In accordance with SS2-01 and SS2-02 samples, ρ increases by further temperature reduction down to $1.8\,K$ which can be attributed to carrier freeze-out effect where electron density decreases by temperature reduction[148-150]. In Fig.27 (b), ρ versus temperature of three Bi_2Te_3 compacted pellets with ρ' of $\sim 80\%$, are compared to each other. Similar ρ trends with a broad peak $\sim 200\,K$ elucidate multiple transport mechanism (semiconducting and metallic transport) within $\sim 80\%$ dense Bi_2Te_3 compacted nanoparticles confirming reproducibility and reliability of the transport measurement.

Wang et. al. reported nonmetallic ρ trend for highly porous films of interconnected Bi_2Te_3 microplates[148]. *Zhang et. al.* observed semiconducting behavior for Sn-doped Bi_2Te_3 polycrystalline film which was attributed to the reduced bulk carrier contribution[149].

For chemical vapor deposited Bi_2Te_3 film of interconnected nano-plates of $\sim 1\,\mu m$, similar trend as represented in Fig.27 (b), was observed by temperature reduction; in that work, the initial resistance increase was attributed to carrier freeze out effect resulting from temperature reduction[148]. For single crystalline Bi_2Se_3[151], similar ρ trend was obtained; therewith, a shallow ρ minimum observed at temperature of $\sim 30\,K$ followed by negative ρ slope which was developed at temperatures higher than $250\,K$ resulting from low n of $\sim 10^{16}\,cm^{-3}$; the negative ρ slope of that work was associated with a crossover to activated behavior at temperatures higher than $300\,K$. In a similar work, multiple ρ variation of single crystalline Bi_2Te_3 similar to what is presented in Fig.27 (b) was observed[152]. *Tian*

et. al. reported a ρ hump at temperature of $\sim 220\ K$ followed by an upturn at temperatures below $14\ K$ for Bi_2Te_3 single crystalline nanowire of $320\ nm$ and $100\ nm$ thick[153].

Similarly, ρ of n-type Bi_2Te_3 nanograined bulk material prepared by spark plasma sintering, encountered a maximum of $\sim 10\ m\Omega.cm$ at $\sim 300\ K$ followed by metallic behavior down to $\sim 2\ K$[99].

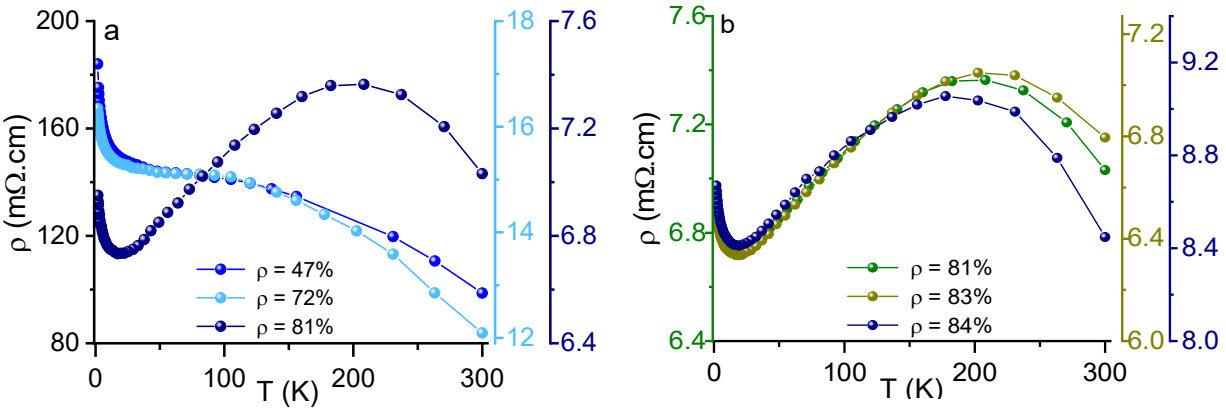

Fig.27: Longitudinal ρ versus temperature of (a) SS2-01, SS2-02 and SS2-03 (b) SS2-03, SS2-04 and SS2-05 in temperature range of $300 - 1.8\ K$.

A transition of transport mechanism from the observed semiconducting-like behavior of SS2-01 and SS2-02 samples into an exclusively different mechanism as a result of density variation, introduces density as a determinative factor of defining physical properties of compacted nanoparticles. According to Fig.27 (a), the measured ρ values were decreased two orders of magnitudes by increasing sample density specifying improved σ contribution.

4.2.2.1. SEM and EDX morphological analysis

For further analysis, SEM images of SS2-01 and SS2-03 compacted pellets at their broken cross section are illustrated in Fig.28. According to Fig.28 (a)-(b), SS2-01 sample is formed by interconnected multi-sized nanoparticles with an average size distribution of $\sim 80\ nm$ which are loosely connected into each other. Randomly-distributed tiny pores of irregular shapes and sizes which are incorporated between nanoparticles, introduce a nanoporous-based design strategy. Non-uniformly distributed porosity of SS2-01 compacted pellet is in accordance with low measured ρ' value of 47% .

The measured ρ of SS2-01 compacted nanoparticles represent high values in the range of $100 - 180\ m\Omega.cm$ specifying direct influence of sample porosity on ρ values (Fig.27 (a)). Considering Fig.25 (b) and Fig. 28 (b), shape of Bi_2Te_3 nanoparticles was relatively preserved in SS2-01 sample; however, particles diameters were expanded resulting from sintering approach.

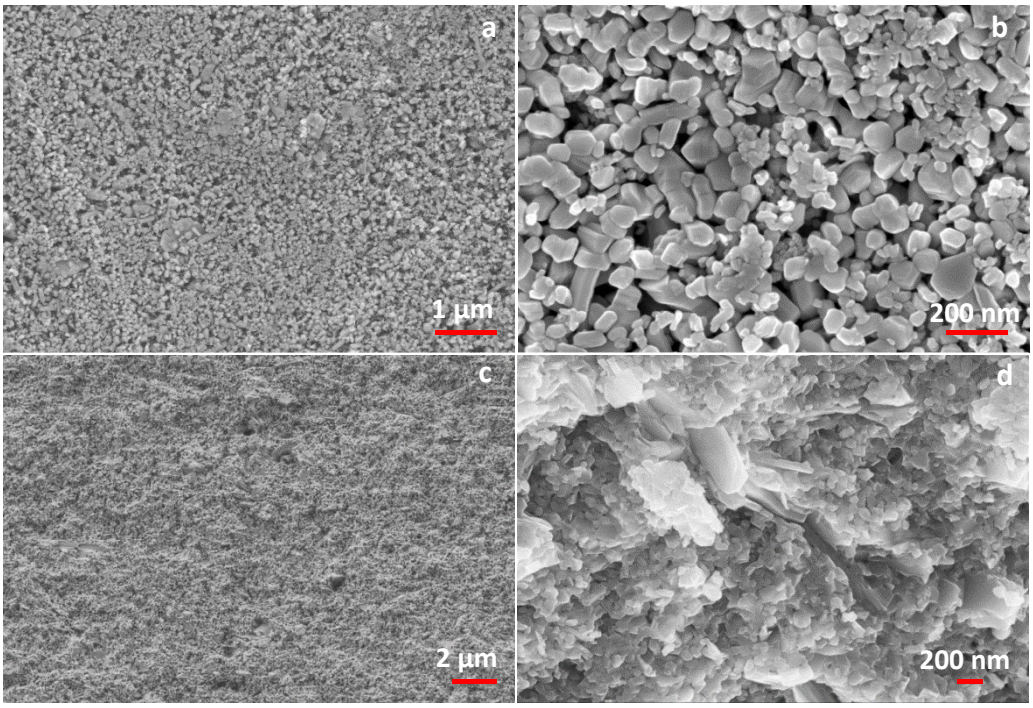

Fig.28: SEM analysis of (a)-(b) SS2-01 and (c)-(d) SS2-03 compacted pellets at a broken cross section.

To compare particle size distribution of SS2-01 compacted nanoparticles with initial SS2 Bi_2Te_3 nanoparticles, histogram of statistical analysis of SS2-01 compacted nanoparticles represented in Fig.28 (b), was compared with Fig.25 (b); the corresponding statistical analysis is provided in Fig.29. According to Fig.29 (a), large particle size distribution ranging from $\sim 31\ nm$ up to $\sim 133\ nm$ was estimated for initial SS2 Bi_2Te_3 nanoparticles. In contrast, particle size distribution of SS2-01 sample varies in the range of $\sim 23\ nm$ up to $\sim 238\ nm$ specifying considerable particle growth resulting from the applied sintering temperature (Fig.29 (b)).

According to the conducted analysis, nanoparticles with diameter between $\sim 40\ nm$ and $\sim 70\ nm$ are the major synthesis products of Bi_2Te_3 SS2 batch; however, minority nanoparticles whose diameter are larger than $\sim 100\ nm$ can be distinguished as well. In contrast, most of the SS2-01 particles are distributed in the range of $40 - 120\ nm$.

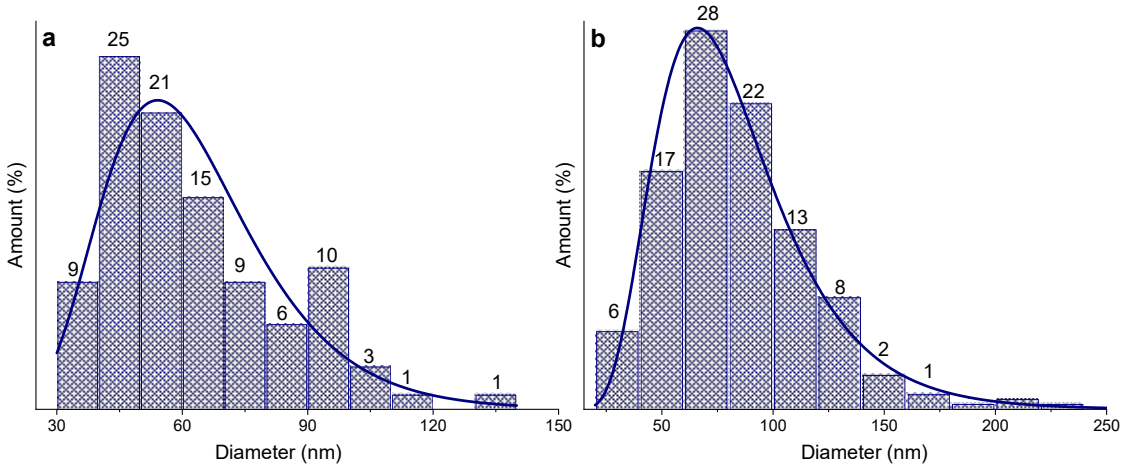

Fig.29: Nanoparticle size distribution of Bi_2Te_3 (a) SS2 initial powder (b) SS2-01 compacted nanoparticles; the blue smooth curve specifies Gaussian fit to particle diameter distribution).

Nanoparticles of SS2-03 sample are tightly bonded into each other representing higher degree of material compaction (Fig.28 (c)-(d)). Compared to Fig.28 (b), nanoparticle growth is visible in Fig.28 (d) originating from higher amount of sintering temperature; therewith, nano-sheets of $\sim 600\, nm$ was measured for SS2-03 compacted pellet. Moreover, by increasing sintering temperature, well-defined nanoparticle boundaries of Fig.28 (b) become invisible. Considerable reduction of porosity and highly-compacted nanoparticles of SS2-03 sample justifies reduced ρ values as represented in Fig.27 (a).

Based on SEM morphological analysis, the measured ρ'values provide an evaluation of nanoparticles degree of compaction where corresponding transport mechanism of Bi_2Te_3 compacted pellets strictly relies on microstructural configuration.

Atomic compositional ratio of compacted pellets was studied using Electron Dispersive X-ray (EDX) analysis. Fig.30 represents SEM images of SS2-03 compacted pellet at a broken cross section. Average atomic ratio of Bi and Te atoms of corresponding SEM images are collected in table.2 which is consistent with desired stoichiometric ratio of 2:3.

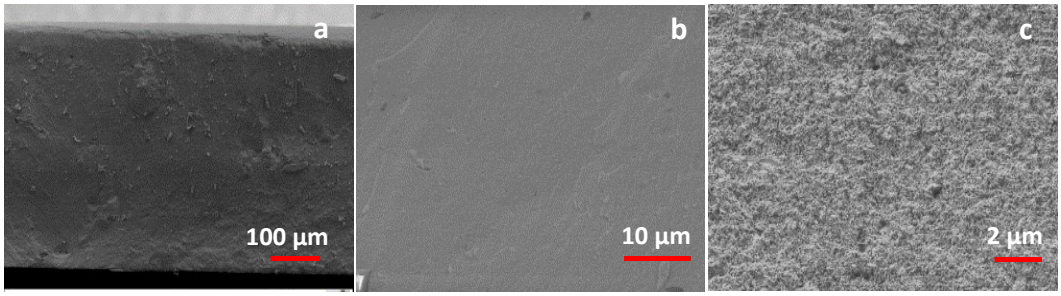

Fig.30: SEM analysis of SS2-03 compacted pellet at a broken cross section with three different resolutions.

Table.2: EDX compositional analysis.

SEM image	b	c
Element	Atomic ratio	
Bi	42%	62%
Te	58%	38%

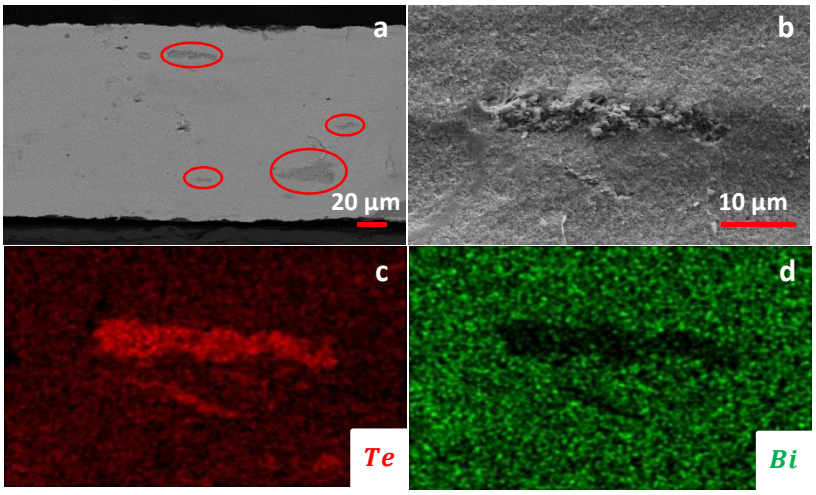

Fig.31: (a) SEM analysis of SS2-04 sample at a broken cross section. (b) Magnified SEM image of the highlighted areas (red circles). (c)-(d) Elemental mapping analysis.

Table.3: EDX compositional analysis.

Element	Bi	Te
Atomic ratio	16%	84%

However, based on the represented SEM cross-sectional analysis of SS2-04 sample in Fig.31, specific areas of quite distinct morphological configuration are randomly distributed within the sample (red circles of Fig.31 (a)). Using elemental mapping EDX analysis, these regions elucidate Te-rich areas of $\sim 84\%$ Te composition (table.3).

Given detected Te-rich areas of $\sim 84\%$ composition, the highlighted nano-rod of Fig.25 (b) with $\sim 700\, nm$ length most likely specifies presence of elemental Te in the initial Bi_2Te_3 powder. Unintentionally-formed elemental Te during Bi_2Te_3 nanoparticle synthesis approach could induce

additional n which could interpret metallic ρ trend of highly-compacted Bi_2Te_3 nanoparticles (Fig.27 (b)).

Hor et. al. reported strong dependence of electrical transport behavior of Bi_2Te_3 single crystal on Te composition where material demonstrated completely distinct transport mechanism with slight variation of elemental Te[154]. The reported ρ trend of Bi_2Te_3 single crystalline of that work is similar to the behavior of Bi_2Te_3 compacted nanoparticles as represented in Fig.27 (b). However, the resulted ρ behavior of that work resulted from Te evaporation at temperature range of $400 - 420\,°C$ which is not the case in this work.

4.2.3. Magnetic field dependent resistivity

To investigate the effect of B on sample ρ known as $M\rho$, magnetic field of B was applied perpendicularly to the sample plane in two different directions. In the following results of R_{xx} and R_{xy} measurements of compacted Bi_2Te_3 nanoparticles followed by B sweep of up to $9\,T$ are provided. Subsequently, l_ϕ of Bi_2Te_3 compacted nanoparticles are calculated using two-dimensional HLN model. In the next step n and μ of propagating charge carriers are calculated using Hall transport characterization results.

4.2.3.1. Magneto-transport characterization

The results of $M\rho$ measurement of five SS2 compacted pellets at different temperatures between $1.8\,K$ and $50\,K$ are demonstrated in Fig.32; $M\rho$ data were normalized using eq.29, where $(M\rho)_{min}$ and $(M\rho)_{max}$ are $M\rho$ at B of zero and $9\,T$ respectively,

$$(M\rho)_n = \frac{M\rho - (M\rho)_{min}}{(M\rho)_{max} - (M\rho)_{min}} \qquad (29)$$

As demonstrated in Fig.32, sharp drop of ρ around zero B of low temperature regimes elucidates strong spin-orbit-coupled transport of SS2 compacted pellets. With increasing temperature, pronounced ρ dip becomes broader and finally disappeared at higher temperatures; therewith, ρ dip of SS2-01 porous pellet disappeared at $14\,K$ while for SS2-03 compacted pellet, evidence of spin-orbit-coupled transport survived up to $50\,K$.

So far, signature of spin-orbit coupled transport which was attributed to WAL effect was observed for different Bi_2Te_3 structures including thin films[155-156], microflakes[157], nanowires[158] and single crystals[152, 159-160]. Interestingly, this is the first time that evidence of quantum transport can be visible on a microscopic Bi_2Te_3 nanoparticle-based sample.

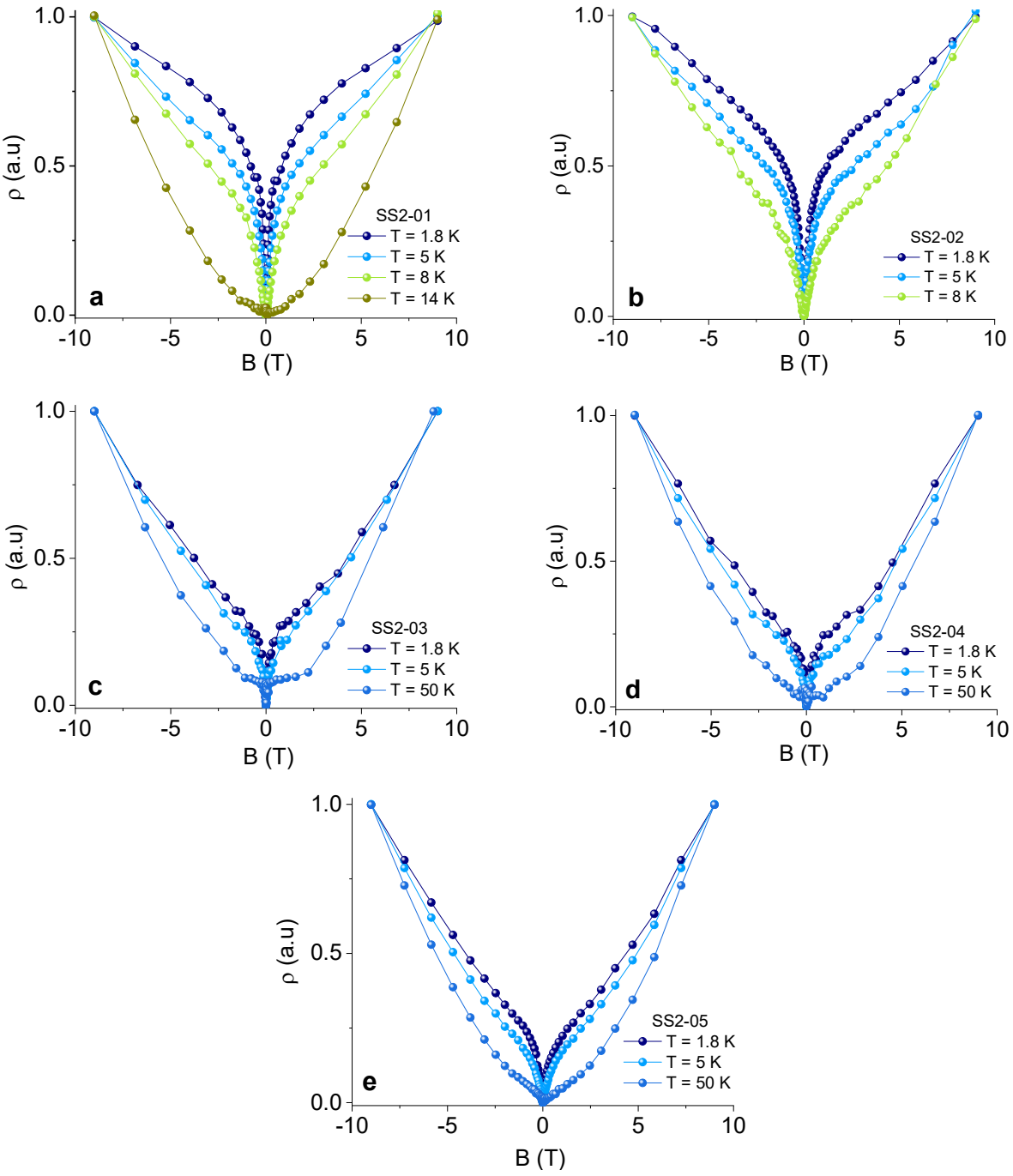

Fig.32: Normalized resistivity versus magnetic field of (a) SS2-01 (b) SS2-02 (c) SS2-03 (d) SS2-04 (e) SS2-05 compacted pellets over magnetic field of $-9\ T$ to $9\ T$ at different temperatures.

4.2.3.1.1. HLN approach

As demonstrated in Fig.33 (a), Magneto-conductance (ΔG) of SS2-01 compacted pellet at three different temperatures of $1.8\ K$, $5\ K$ and $8\ K$ for B interval of $-0.5\ T$ up to $0.5\ T$ was fitted using eq.30[161],

$$\Delta G_{2D} = \frac{-\alpha e^2}{2\pi\hbar}\left[\psi\left(\frac{1}{2}+\frac{B_\phi}{B}\right) - \ln\left(\frac{B_\phi}{B}\right)\right] \quad (30)$$

$$B_\phi = \frac{\hbar}{4el_\phi{}^2} \quad (31)$$

In this equation, B_ϕ and ψ represent characteristic field and digamma function, respectively, α in eq.30 is a prefactor; based on eq.31, B_ϕ associates with characteristic length of l_ϕ.

The fitted $M\rho$ dip of SS2-01 sample as represented in Fig.32 (a), with respect to 2D HLN interference formula elucidates evidence of quantum interference transport known as WAL effect, in the compacted Bi_2Te_3 nanoparticles. As illustrated in Fig.32, destructive quantum interference of electronic wave function was destroyed by applying small amount of perpendicular magnetic field resulting in quantum conductance correction of ΔG_{2D} (eq.30).

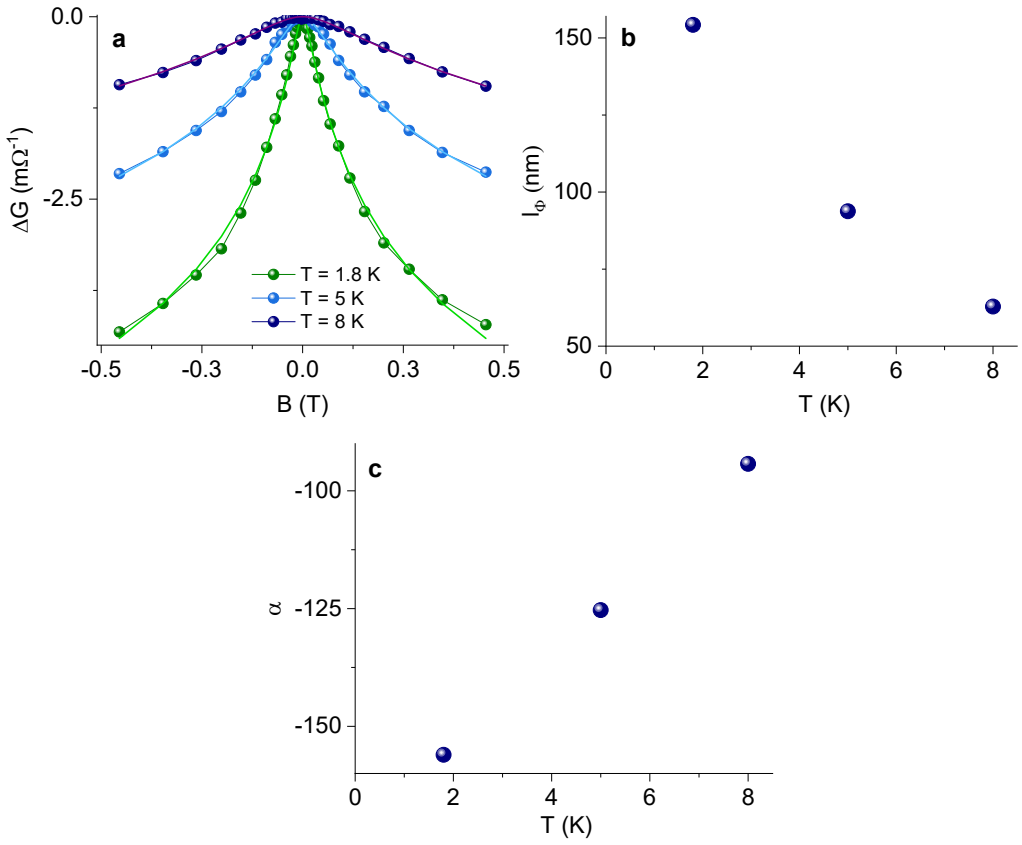

Fig.33: ΔG fitting of SS2-01 compacted pellet using HLN approach (a) ΔG versus magnetic field of $-0.5\ T$ up to $0.5\ T$ at three different temperatures of $1.8\ K$, $5\ K$ and $8\ K$. Calculated fitting parameters of (b) phase coherence length and (c) prefactor of alpha at temperatures of $1.8\ K$, $5\ K$ and $8\ K$.

The calculated fitting parameters of l_ϕ and α are illustrated in Fig.33 (b)-(c); therewith, l_ϕ decreases with increasing temperature which is consistent with previous reports[156-157, 160-161]. Considering high numbers of scattering barriers introduced in a nanograined bulk material (Fig.25 and 28), the calculated l_ϕ of $\sim 154\ nm$ at $1.8\ K$ is roughly half of the reported value for epitaxial Bi_2Te_3 thin film samples ($\sim 331\ nm$)[162]. Given l_ϕ value of SS2-01 sample, porous-based design strategy can be regarded as an effective engineering approach of realizing topologically-protected surface transport within nanograined bulk material. Basically, the incorporated porosity within the material could introduce high energy barriers towards bulk carrier propagation, yet retain electrically-connected interfaces; therewith, entangled surface and bulk transport contributions within the material can be decoupled to some extent.

The prefactor α in HLN formula is defined as WAL coefficient signifying the number of topologically-independent conducting channels. Theoretically, $\alpha = -0.5$ was reported for one independent topological channel[163-164]. Considering multiple conducting surface and bulk transport channels in a nanograined bulk material as well as dominant bulk carrier contribution, α can be assumed much higher than the reported values[162]. The calculated α values represented in Fig.33 (c) are three orders of magnitudes higher than the theoretically predicted one. However, the increasing trend of α values with temperature reduction is in accordance with the previous reports[161-162].

ρ dip of other SS2 compacted pellets was fitted using eq.30 and the corresponding fitting parameters were calculated; therewith, a comprehensive overview of the calculated fitting parameters of five SS2 compacted pellets at two different temperatures of $1.8\ K$ and $5\ K$ is summarized in table.4. According to the table, fitting parameters of l_ϕ and α follow a systematic trend; the calculated l_ϕ of SS2 compacted pellets increased with temperature reduction.

In addition, contribution of multiple transport channels into the whole transport signal was improved by decreasing temperature; therewith, the calculated α values were normalized with respect to the calculated one at $1.8\ K$ (α_N).

It is worth to mention that the calculated α values of SS2 samples with average density of $\sim 60\%$ and $\sim 80\%$ are three and four orders of magnitudes higher than the theoretically predicted one respectively, specifying improved contribution of multiple transport channels with increasing sample density.

Table.4: Fitting parameters of SS2 compacted pellets at temperatures of $1.8\ K$ and $5\ K$.

Sample name	$l_\phi\ (nm)$		α		α_N	$\rho'\ (\%)$
	Temperature (K)					
	1.8	5	1.8	5		
SS2-01	154	94	-156	-125	0.80	47
SS2-02	91	86	-263	-214	0.81	72
SS2-03	109	87	-1137	-913	0.80	81
SS2-04	117	74	-1421	-1314	0.92	83
SS2-05	114	88	-1357	-1002	0.73	84

Based on comprehensive analysis of $M\rho$ measurements, sharp ρ dip of spin-orbit-coupled transport can be interpreted as quantum interference phenomenon known as WAL effect. Therewith, the calculated ρ dip of nanoparticle-based Bi_2Te_3 samples (Fig.32 (a)-(e)) confirms quantum interference contribution of Bi_2Te_3 charge carriers associating with surface transport channel.

In addition, different values of fitting parameters (table.4) determine distinct ρ-dip configuration of Bi_2Te_3 compacted samples (Fig.32 (a)-(e)) in quantum diffusive transport regime.

4.2.3.1.2. Density dependent transport characterization

In Fig.34 (a), $M\rho$ of loosely-compacted Bi_2Te_3 nanoparticles of SS2-01 sample is compared with two SS2 compacted pellets of SS2-02, SS2-05 with higher ρ' values at specific temperature of $1.8\ K$. As represented in Fig. 34 (a), Bi_2Te_3 nanoporous bulk material elucidates the sharpest ρ dip. Interestingly, ρ dip of Bi_2Te_3 compacted nanoparticles becomes broader followed by compaction improvement.

Corresponding l_ϕ values of extracted at $1.8\ K$ versus ρ' are represented in Fig.34 (b); the amount of l_ϕ decreased by ρ' enhancement with the highest l_ϕ value of $\sim 154\ nm$ (blue circle) associating with loosely-compacted Bi_2Te_3 nanoparticles.

Given the calculated l_ϕ value of $\sim 154\ nm$ is comparable to the nanoparticle length scale (Fig.29), detailed morphological analysis of the loosely-compacted Bi_2Te_3 nanograined sample is conducted in the next section.

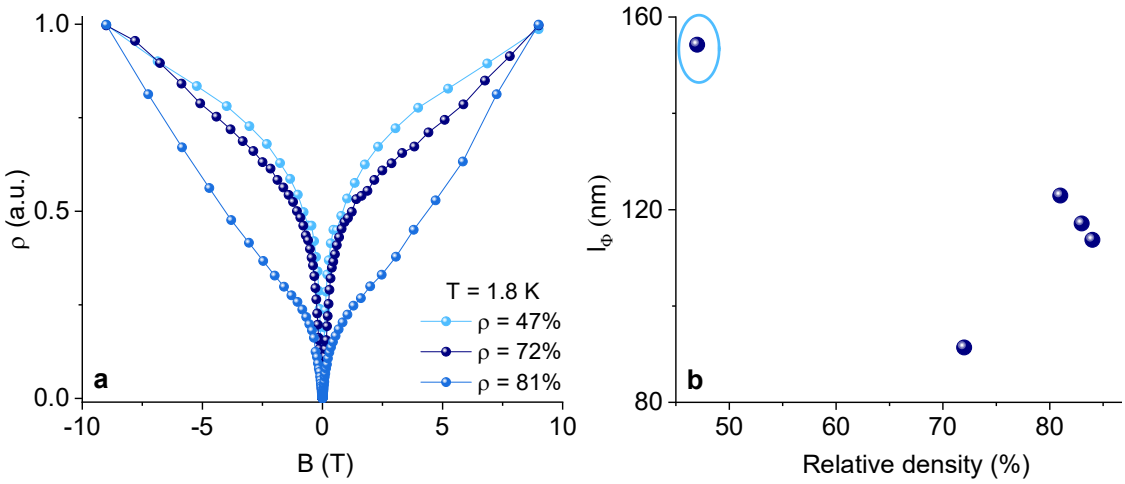

Fig.34: (a) Normalized $M\rho$ of SS2-01, SS2-02 and SS2-05 compacted pellets at temperature of $1.8\,K$. (b) l_ϕ of SS2 compacted pellets versus relative sample density.

4.2.3.2. Morphological characterization

4.2.3.2.1. AFM and Conductive-AFM analysis

Given high calculated l_ϕ value of SS2-01 sample, AFM and Conductive-AFM analysis of Bi_2Te_3 nanoporous sample at a broken cross section was conducted at room temperature; the corresponding results are shown in Fig.35. According to Fig.35 (a), AFM analysis depicts randomly oriented Bi_2Te_3 nanostructure with average particle size of $\sim 120\,nm$. Multi-sized nanoparticles with irregular shapes of Fig.35 (a) are in accordance with the conducted SEM morphology analysis of Fig.28 (a)-(b). An incorporated porosity with an average size of $\sim 400\,nm$ within the material introduces a distinct nanoparticle-based material design strategy resulting in high surface-to-volume ratio.

The specific surface area (S) of SS2 Bi_2Te_3 nanoparticles and compacted nanoparticle bulk of SS2-01 was determined by gas adsorption experiment with Brunauer-Emmett-Teller (BET) method. The result of BET measurement for $300\,mg$ and $69.8\,mg$ of SS2 Bi_2Te_3 powder and SS2-01 compacted bulk pellet accordingly, is summarized in table.5.

Free surface area of $10.7\ \mathrm{x}\ 10^4\ cm^2g^{-1}$ of Bi_2Te_3 nanoparticles was reduced into $6.1\ \mathrm{x}\ 10^4\ cm^2g^{-1}$ for SS2-01 compacted pellet originating from surface degradation under compaction procedure. However, the preserved amount of 57% of free surfaces within the nanograined bulk material agrees well with the previous consideration of high surface-to-volume ratio (Fig.35 (a)).

Such high amount of free surfaces within the nanoporous bulk material is capable of surface transport promotion and can partly explain high calculated l_ϕ value. Considering density of Bi_2Te_3

($7.7\ gcm^{-3}$)[147], surface-to-volume ratio of approximately $46.9 \text{ x } 10^4\ cm^2/cm^3$ was calculated confirming highly porous nanograined bulk material.

Table.5: BET characterization of SS2 nanoparticles and SS2-01 bulk pellet.

	m (mg)	S $(cm^2 g^{-1})$
Powder	300	10.7 x 10^4
Pellet	69.8	6.1 x 10^4

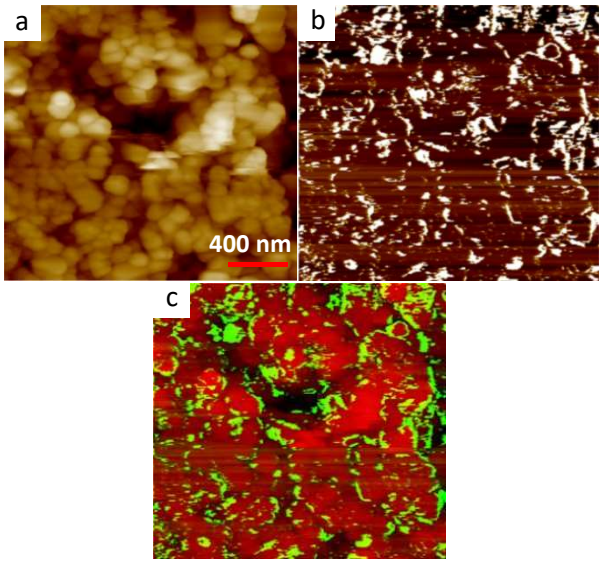

Fig.35: (a) AFM image analysis of SS2-01 bulk pellet at a broken cross section. (b) Current image network of corresponding AFM image of represented in (a). (c) Superposition of AFM analysis and corresponding current image.

High surface-to-volume ratio of Bi_2Te_3 compacted pellet could provide a three-dimensional network of charge carrier transportation. To visualize electronic transport mechanism of highly porous SS2-01 sample, current image network of the represented topography in Fig.35 (a), was provided by Conductive-AFM characterization. White paths of Fig.35 (b) specify current flow of $\sim 8\ nA$ through the defined white trajectories. By merging current and topographic images, one can identify current trajectory suppliers. As illustrated in Fig.35 (c), either single Bi_2Te_3 nanoparticles, surrounding area of

agglomerated nanoparticles or the introduced porosity within the material could contribute into electrical transport mechanism.

4.2.3.2.2. TEM analysis

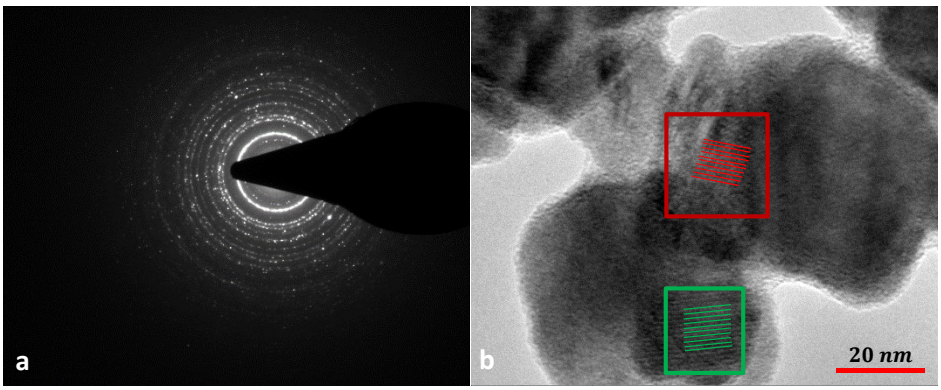

Fig.36: TEM analysis; (a) Diffraction pattern of SS2-01 bulk pellet. (b) Two adjacent nano-grains (red and green lines specify detected atomic fringes which are oriented in different crystallographic orientations).

TEM morphological analysis of SS2-01 nanoporous sample is demonstrated in Fig.36. As represented in Fig.36 (a), concentric circular diffraction pattern confirms polycrystalline nature of SS2-01 compacted nanoparticles. Fig.36 (b) illustrates two adjacent grain boundaries with an average grain size of $\sim 60\,nm$ which is comparable with the average initial Bi_2Te_3 nanoparticle distribution of $\sim 40 - 70\,nm$ (Fig.29 (a)). Atomic fringes highlighted in red and green are distributed in different crystallographic orientations introducing effective scattering centers within the Bi_2Te_3 nanograined bulk material.

4.2.3.3. Hall characterization

Hall characterization analysis of five SS2 Bi_2Te_3 compacted nanoparticles at temperatures of $1.8\ K$, $5\ K$, $50\ K$, $100\ K$ and $300\ K$ are illustrated in Fig.37; the negative Hall slope suggests n-type carrier transport mechanism.

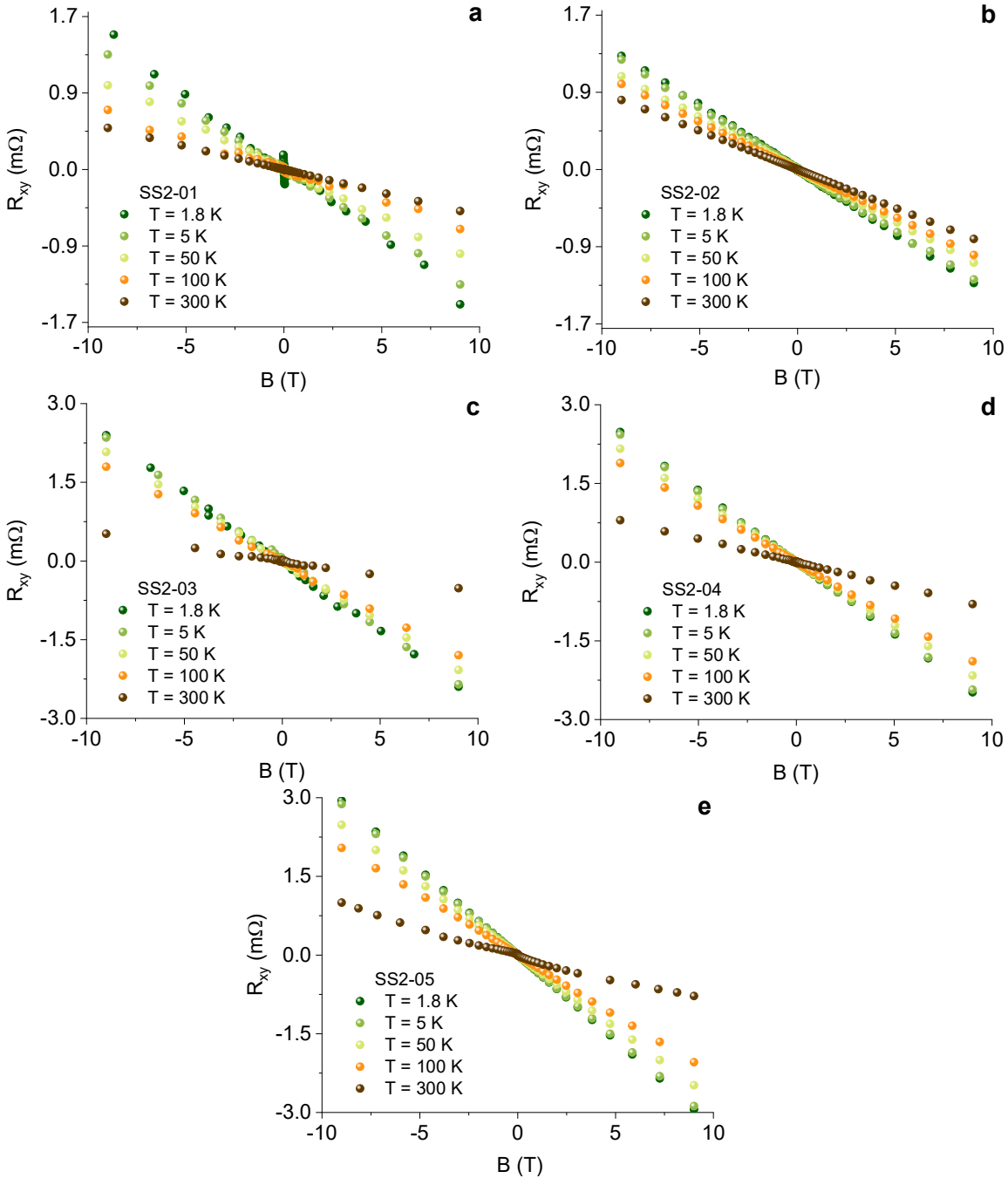

Fig.37: Hall measurement of (a) SS2-01 (b) SS2-02 (c) SS2-03 (d) SS2-04 (e) SS2-05 compacted pellets over magnetic field of $-9\ T$ to $9\ T$ at temperatures of $1.8\ K$, $5\ K$, $50\ K$, $100\ K$ and $300\ K$.

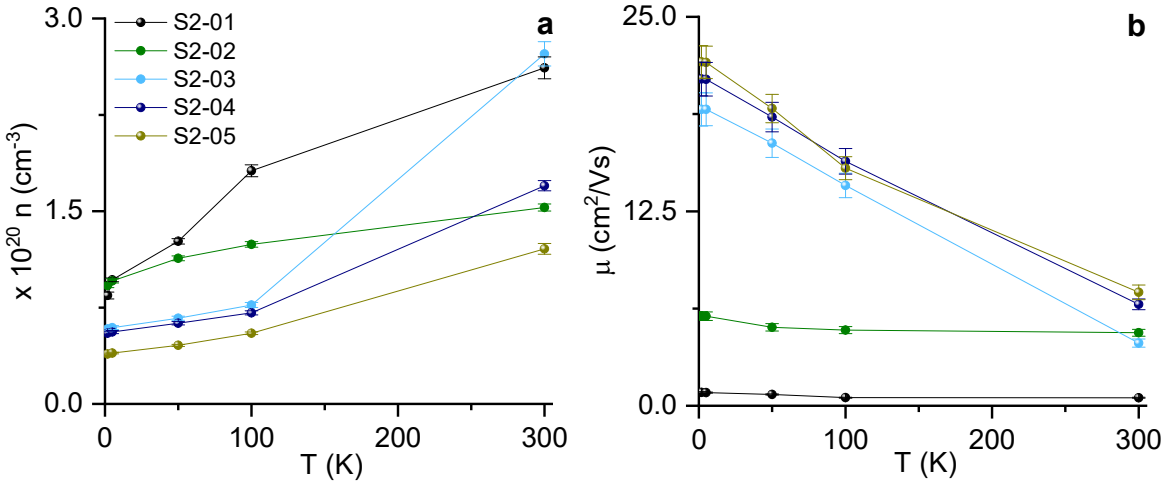

Fig.38: (a) n and (b) μ of SS2 compacted pellets in temperature range of $300 - 1.8\ K$.

n and μ of charge carriers at temperatures of $1.8\ K, 5\ K, 50\ K,\ 100\ K$ and $300\ K$ were calculated using eq.25-26; the corresponding results are shown in Fig.38. According to Fig.38 (a), n of SS2 compacted pellets reduced with temperature reduction down to $1.8\ K$ originating from carrier freeze-out effect. Therewith, the calculated n of $10^{20}\ cm^{-3}$ at room temperature decreased one order of magnitude into $10^{19}\ cm^{-3}$ at $1.8\ K$. *Zhang* reported n in the same order of magnitude for n-type Bi_2Te_3 which was prepared by spark plasma sintering[99].

Given calculated n of $\sim 10^{19} - 10^{20}\ cm^{-3}$, bulk carriers are supposed to dominate Hall transport signal. According to Fig.38 (b), μ of charge carriers improved with temperature reduction; while μ variation of loosely-compacted Bi_2Te_3 nanoparticles (SS2-01) together with SS2-02 compacted pellet are not considerable, μ of highly-compacted SS2 nanoparticles of SS2-03, SS2-04 and SS2-05 at $1.8\ K$ is ~ 2 times of the measured values at room temperature which is consistent with lower ρ values represented in Fig.27. This can be attributed to the promoted bulk carrier contribution into the whole transport signal resulting from compaction improvement.

Low calculated μ values of SS2-01 nanoporous sample proves strong scattering mechanism of bulk contribution channel from porosity, Te nano-rods and incorporated interfaces of SS2-01 nanograined bulk material. Given high calculated l_ϕ value together with evidence of bulk channel suppression, one can conclude with surface and bulk transport channel disentanglement of the Bi_2Te_3 nanograined bulk material using porosity-based design strategy. However, more investigation must be conducted to define position of E_F which could interpret the observed nonmetallic trend of represented in Fig.27 (a).

4.3. Developed synthesis approach

4.3.1. Powder characterization

In this section, Bi_2Te_3 nanoparticles which were synthesized in the absence of capping agent of OA serve as the model system.

Morphological analysis of SS22 initial powder is provided in Fig.39. Concentric circular diffraction pattern illustrated in Fig.39 (a) represent polycrystalline nature of the initial Bi_2Te_3 powder material. High resolution TEM analysis of SS22 nanoparticle is represented in Fig.39 (b)-(d); hexagonal shape of single nanoparticle confirms high quality of crystalline structure of SS22 nanoparticles batch (Fig.39 (b)). Compared to Fig.25, where some traces of contamination were detected like elemental Te and capping agent of OA, no evidence of such contamination was observed.

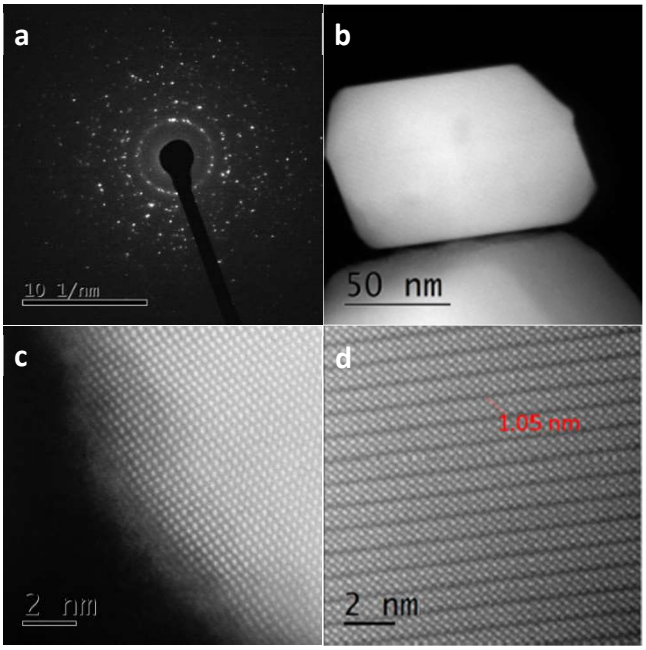

Fig.39: Electron diffraction pattern of SS22 Bi_2Te_3 initial powder. (b)-(d) TEM images of single Bi_2Te_3 nanoparticle.

Highly-crystalline and well-oriented atomic fringes with calculated QL thickness value of $\sim 1.05\ nm$ which are demonstrated in Fig.39 (c)-(d), offer high quality material which is distinct to what was observed in classical approach.

According to SEM image represented in Fig.40 (a), multi-sized Bi_2Te_3 nanoparticles with average size of $\sim 60\ nm$ are randomly distributed. Based on statistical analysis (Fig.40 (b)), particle size distribution varies in the range of $\sim 23\ nm$ up to $\sim 176\ nm$ with more than 50% of particles representing diameter in the range of $20 - 80\ nm$.

Compared to classical approach, Bi_2Te_3 nanoparticles of distinct morphological configuration are distinguishable. Moreover, no Te nano-rod was observed.

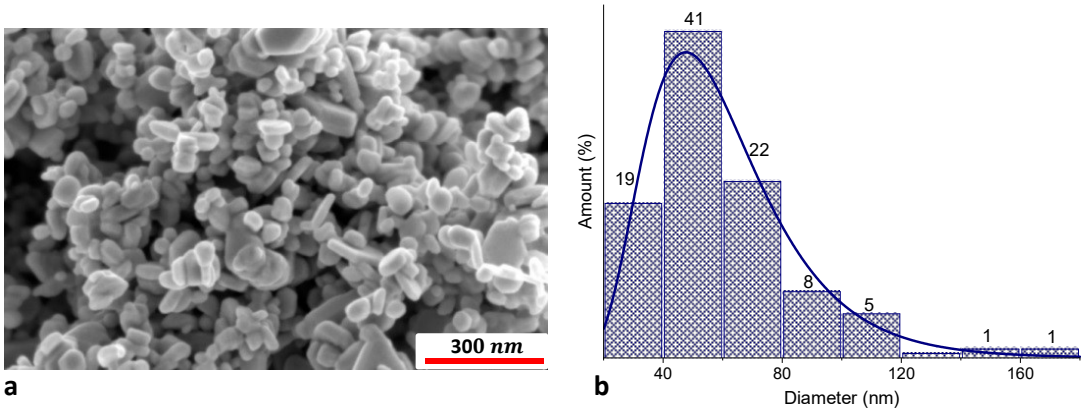

Fig.40: (a) SEM image and (b) corresponding statistical particle size distribution of Bi_2Te_3 SS22 initial powder.

Due to the fact that most of the initial powder was invested first on TE characterization which will be discussed in the next chapter, along with limited amount of ILs-based Bi_2Te_3 initial nanoparticles ($600\ mg$), the following results only cover Bi_2Te_3 samples of highly-compacted nanoparticles with ρ' in the range of $\sim 85 - 99\%$.

The list of investigated samples is represented in table.1. Compared to the first approach where sintering temperature of $\sim 320\,^{\circ}C$ resulted in Bi_2Te_3 compacted nanoparticles with ρ' of $\sim 80\%$, in the current approach, lower sintering temperature of $\sim 300\,^{\circ}C$ resulted in $\sim 99\%$-dense Bi_2Te_3 bulk pellets.

4.3.2. Morphological characterization of Bi_2Te_3 compacted nanoparticles

4.3.2.1. SEM and EDX morphological analysis

SEM image analysis of SS22-01 and SS22-03 compacted pellets at a broken cross section are demonstrated in Fig.41. According to Fig.41 (a)-(b), microstructural configuration of SS22-01 and SS22-03 samples at a broken cross section are compared to each other. As demonstrated in Fig.41 (b), particle growth in SS22-03 compacted pellet is well-recognized originating from higher sintering temperature (table.1). Compared to Fig.28, Bi_2Te_3 compacted nanoparticles of current approach demonstrate completely distinct morphological configuration where polygonal-shaped particles are randomly-oriented distributed within the material.

Compared to the Bi_2Te_3 nanoparticles synthesized by classical approach, average particle size distribution of current approach has been increased significantly; as demonstrated for SS22-03 compacted pellet (Fig.41 (c)-(f)), non-uniform particle size distribution consisting of coarse sheets of μm length as well as fine nanoparticles of $\sim 200\ nm$ are closely compacted into each other.

Highly-compacted sheets of $\sim 1.5\ \mu m$ length with only few nanometers thickness (Fig.41 (d) and (f)) introducing a high surface-to-volume ratio within the Bi_2Te_3 nano bulk material, provide well-defined trajectories for surface and bulk carrier transport channels.

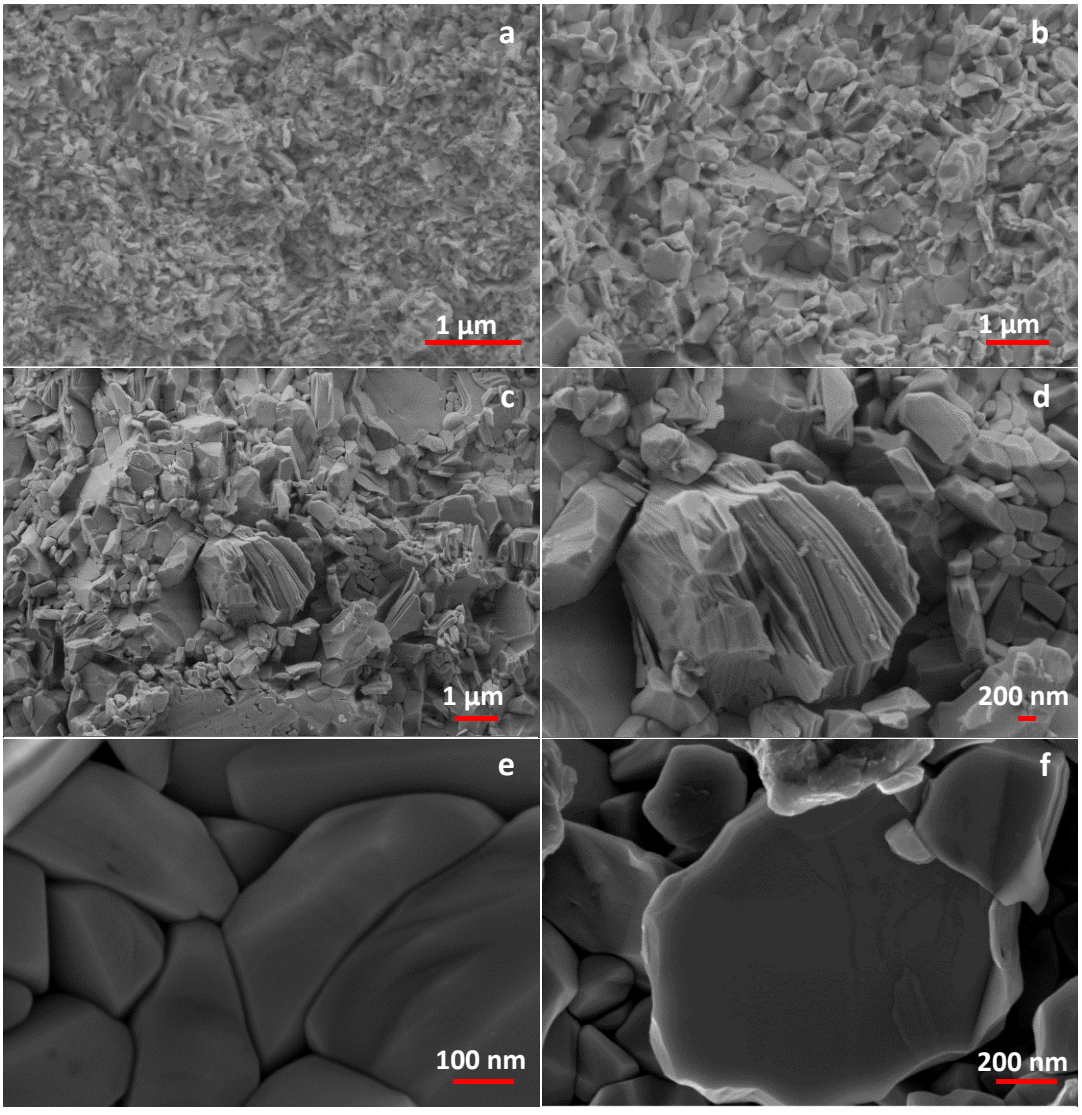

Fig.41: SEM analysis of SS22-01 (ρ = 85%) and (b)-(f) SS22-03 (ρ = 98%) compacted pellets at a broken cross section.

Average atomic compositional ratio of SS22 compacted pellets of SEM images represented in Fig.41 (a)-(b), are demonstrated in table.6 using EDX analysis; the corresponding results confirm desired stoichiometry of 2:3.

Table.6: EDX compositional analysis.

Element	Atomic ratio	
SEM	Fig.43 (a)	Fig.43 (b)
Bi	39%	40%
Te	61%	60%

4.3.2.2. AFM and Conductive-AFM analysis

Fig.42 (a) depicts AFM morphological analysis of SS22-03 Bi_2Te_3 compacted nanoparticles conducted at room temperature on the pellet cross section. The topographic AFM image shows a multi-grained-based nanoparticle material with the preserved characteristics of initial Bi_2Te_3 nanoparticles agglomeration.

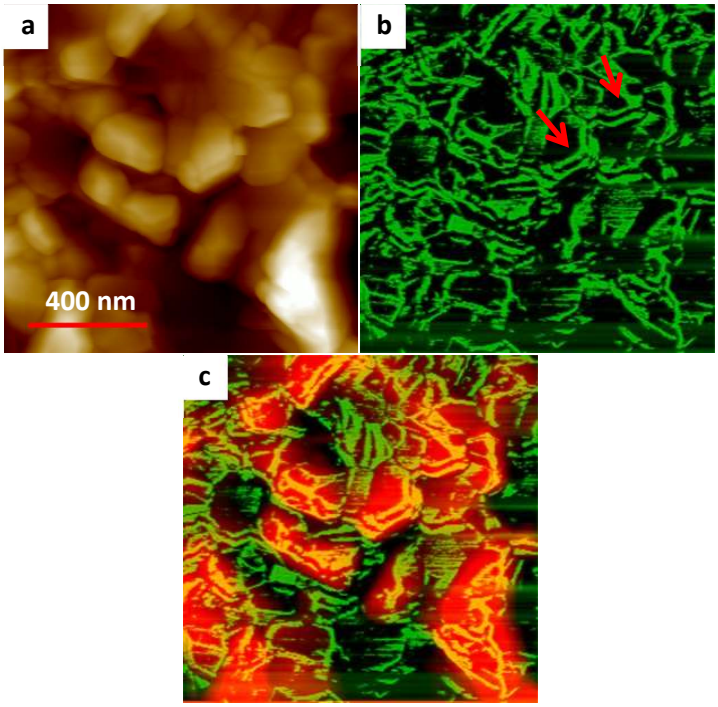

Fig. 42: (a) AFM image analysis of SS22-03 (ρ = 98%) bulk pellet. (b) Current image network of corresponding topography of represented in (a). (c) Superposition of AFM image and current network analysis.

To elucidate conduction network, Conductive-AFM analysis of the represented topography in Fig.42 (a) was performed at room temperature (Fig.42 (b)). Conductive-AFM on the same cross section indicates an enhanced conductivity along the interfaces of compacted nanoparticles; the green regions of Fig.42 (b) represent conducting current of $\sim 3\ nA$. Note that only percolating conductive channels contribute to the Conductive-AFM image.

As demonstrated in Fig.42 (b), conductive current flowing on nanoparticles facets (red arrows) visualizes closely-compacted nano-sheets of Fig.41. Compared to the observed current image of SS2-01 nanoporous sample (Fig.35 (b)), the continuous percolating current network of Fig.42 (b) can be attributed to distinct synthesis approach together with higher compaction degree of Bi_2Te_3 nanoparticles.

Conducted BET characterization of SS22-03 compacted pellet confirms that approximately one tenth of the initially available free surfaces are preserved within the compacted bulk material where free surface area of $1.8 \text{ x } 10^5\ cm^2 g^{-1}$ of the Bi_2Te_3 nanoparticles reduced into $2.6 \text{ x } 10^4\ cm^2 g^{-1}$ for the compacted pellet (table.7). Considering density of Bi_2Te_3 of $7.7\ g\ cm^{-3}$ Ref[147], the pellet revealed a surface-to-volume ratio of approximately $2 \text{ x } 10^5\ cm^2/cm^3$. Compared to classical approach, surface-to-volume ratio of the initial powder increased one order of magnitude which is in accordance with the realized μm surfaces.

Table.7: BET characterization of SS22 nanoparticles and SS22-02 bulk pellet.

	m (mg)	S $(cm^2 g^{-1})$
Powder	350	1.8 x 10^5
Pellet	74.8	2.6 x 10^4

4.3.3. Temperature dependent resistivity

Temperature-dependent ρ of SS22 compacted nanoparticles is represented in Fig.43; as shown in the figure, ρ specifies a metallic conductivity trend down to a temperature of $\sim 5\ K$ which is a typical behavior of highly-doped small band gap semiconductors. Below $5\ K$, ρ shows a clear drop which is qualitatively comparable to the behavior of a superconductor (Fig.43 (b)); however, based on heat capacity (C_p) measurement represented in Fig.43 (c), no indication of phase transition in this

temperature regime is evident. Therefore, this drop of ρ can be interpreted as an evidence of spin-orbit-coupled transport.

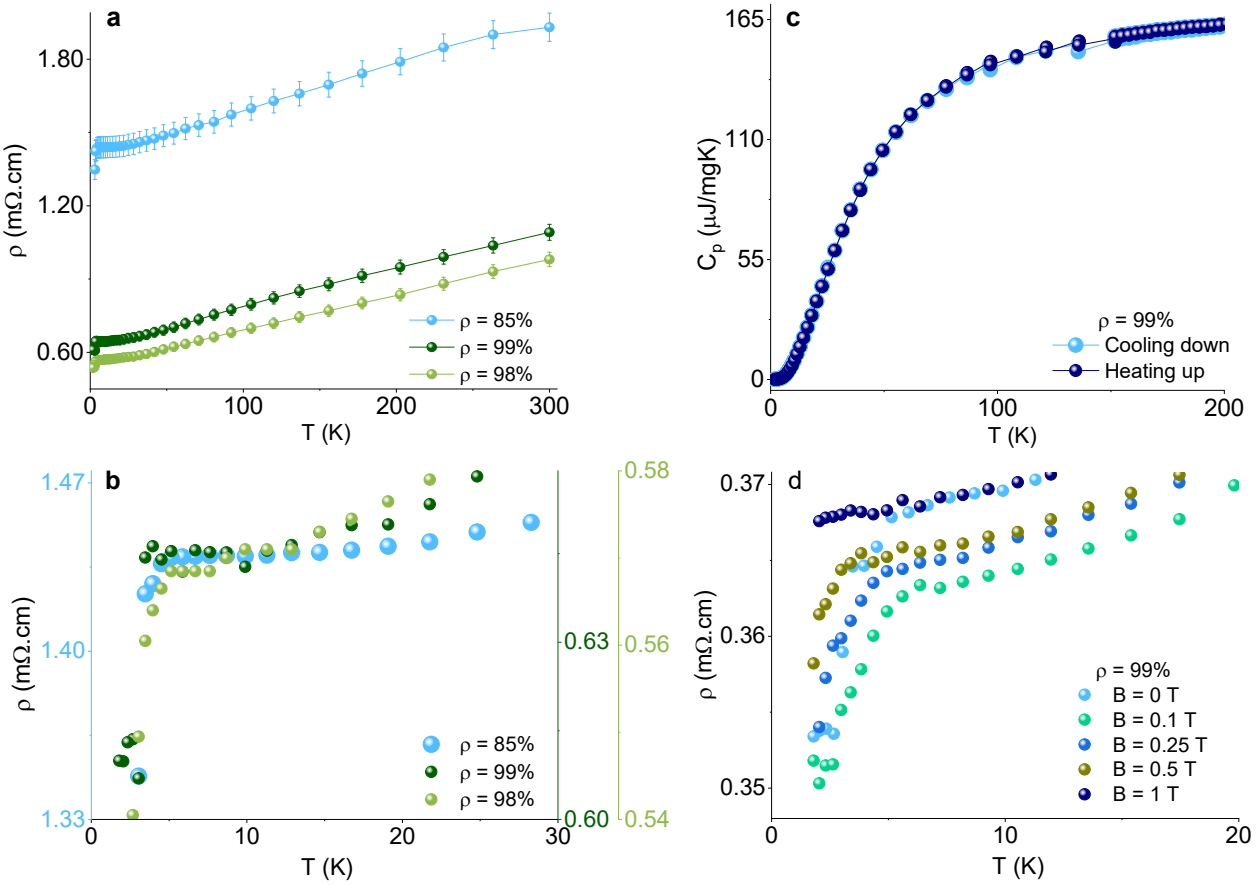

Fig.43: (a) ρ versus temperature of SS22 compacted pellets in temperature range of $300 - 1.8\ K$. (b) Magnified ρ drop of SS22 compacted pellets in temperature range of $30 - 1.8\ K$. (c) Heat capacity measurement of SS22-02 compacted pellet. (d) ρ versus temperature of low temperature regime (up to $30\ K$) with applied magnetic field of $0.1\ T$ up to $1\ T$.

For SS22-01, SS22-02 and SS22-03 samples ρ drop occurs at $\sim 7.6\ K$, $\sim 4\ K$ and $\sim 5\ K$ respectively. The observed ρ drop of SS22 compacted nanoparticles which was contacted directly via Copper Beryllium probes proves intrinsically-based material properties.

Similar downward trend of ρ was previously reported only for a high purity epitaxial Bi_2Te_3 film with a reduced bulk carrier density, and was attributed to the predominant conductivity channel of Dirac carriers arising at the surfaces of the TI[165]. As shown in Fig.43 (d), by applying perpendicular B of $0.1\ T$ up to $1\ T$ on the surface of SS22-02 compacted pellet, the signature of spin-orbit-coupled transport disappears.

Similar to the previous results (classical approach), ρ values decreased from $\sim 1.5\ m\Omega.cm$ into $\sim 0.6\ m\Omega.cm$ with increasing compaction degree of SS22 compacted pellets from $\sim 85\%$ to $\sim 99\%$ respectively. However, ρ values of current approach are reduced around one order of magnitude compared to classical approach (Fig.27), specifying Bi_2Te_3 nanoparticles of low levels of impurities and surface contaminations.

4.3.4. Magnetic field dependent resistivity

4.3.4.1. Magneto transport characterization

The results of $M\rho$ measurement of SS22 compacted nanoparticles are represented in Fig.44; similar to classical approach, $M\rho$ measurements exhibit an indication of spin-orbit-coupled transport where ρ values dropped sharply around zero B. Quite distinct ρ dip configuration of this approach specifies synthesis-based electrical transport properties of the nanoparticle-based Bi_2Te_3 bulk material.

Density dependent $M\rho$ of three different SS22 compacted pellets at $1.8\ K$ are compared in Fig.44 (d) where sharp ρ dip of SS22-01 sample becomes broader followed by compaction improvement which is in accordance with the previous approach (Fig.34 (a)).

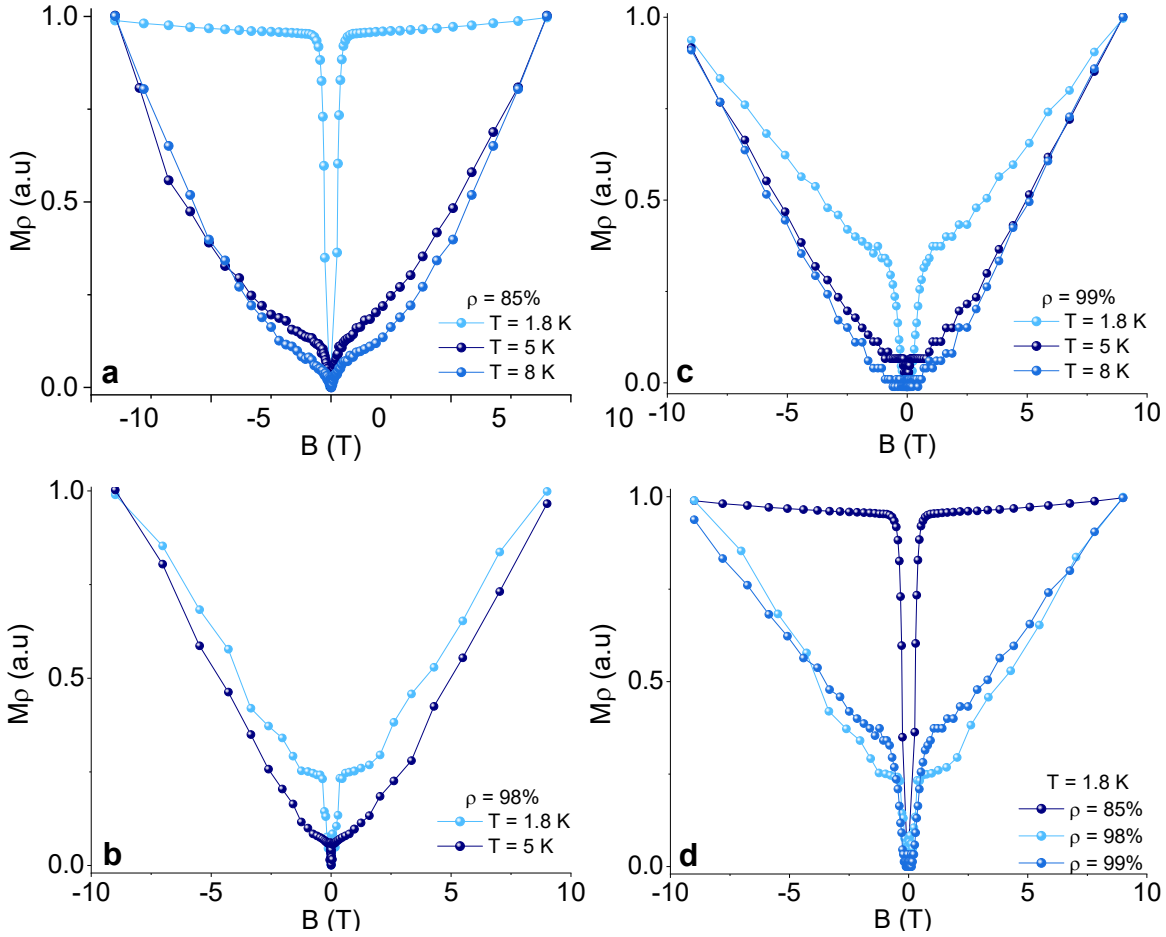

Fig.44: Normalized $M\rho$ of (a) SS22-01 (b) SS22-02 and (c) SS22-03 compacted pellets over magnetic field of $-9\ T$ to $9\ T$ at different temperatures. (d) Normalized $M\rho$ of three different SS22 compacted samples at temperature of $1.8\ K$.

4.3.4.1.1. HLN approach

To define the governed transport mechanism of the SS22 nanoparticle-based bulk material at low-temperature regime, two-dimensional HLN quantum interference model was effectively applied. However, ΔG of SS22 compacted nanoparticles was not fitted using eq. 30; ΔG of SS22-02 and SS22-03 compacted pellets were well-fitted using eq.32[166-167] where B_{i} $(i = \phi, SO, e)$ and ψ represent characteristic field and digamma function, respectively, α is a prefactor.

$$\Delta \mathrm{G}_{2D} = \frac{-e^2}{2\pi h}\left[\psi\left(\frac{B_\phi}{B}+\frac{1}{2}\right)-\ln\left(\frac{B_\phi}{B}\right)\right]-\frac{e^2}{\pi h}\left[\psi\left(\frac{B_{SO}+B_e}{B}+\frac{1}{2}\right)-\ln\left(\frac{B_{SO}+B_e}{B}\right)\right]+\frac{3e^2}{2\pi h}\left[\psi\left(\frac{\left(\frac{4}{3}\right)B_{SO}+B_\phi}{B}+\frac{1}{2}\right)-\ln\left(\frac{\left(\frac{4}{3}\right)B_{SO}+B_\phi}{B}\right)\right] \quad (32)$$

$$B_i = \frac{\hbar}{4el_i^2} \quad (33)$$

Considering three characteristic lengths of l_ϕ, spin-orbit scattering length (l_{SO}) and elastic scattering of mean free path (l_e), B_i of each scattering channel can be identified using eq.33[166]. Due to dominance of l_ϕ at low temperatures and small magnetic fields, B_ϕ is considered as characteristic field in quantum diffusive transport regime. Subsequently, l_e and spin orbit scattering contribution of bulk carriers are well approximated by the B^2 term represented in eq.34. Compared to the applied interference model of previous approach (eq.30), additional cB^2 term of the current approach introduces extra scattering mechanisms of l_e and l_{SO} into the transport signal.

$$\Delta G_{2D} = \frac{-\alpha e^2}{2\pi h}\left[\psi\left(\frac{1}{2}+\frac{B_\phi}{B}\right) - \ln\left(\frac{B_\phi}{B}\right)\right] - cB^2 \quad (34)$$

ΔG fitting of SS22-02 and SS22-03 compacted nanoparticles at three different temperatures are represented in Fig.45 (a)-(b) and (d)-(e), respectively, using eq.34. Therewith, temperature dependent l_ϕ of these two samples is provided in Fig.45 (c) and (f). Sudden l_ϕ variation from $\sim 22\, nm$ to $\sim 70\, nm$ and $\sim 28\, nm$ to $\sim 107\, nm$ for SS22-02 and SS22-03 compacted samples respectively, followed by temperature reduction which is consistent with previous reports[166, 168], could be an explanation for the observed downward ρ trend below $5\ K$.

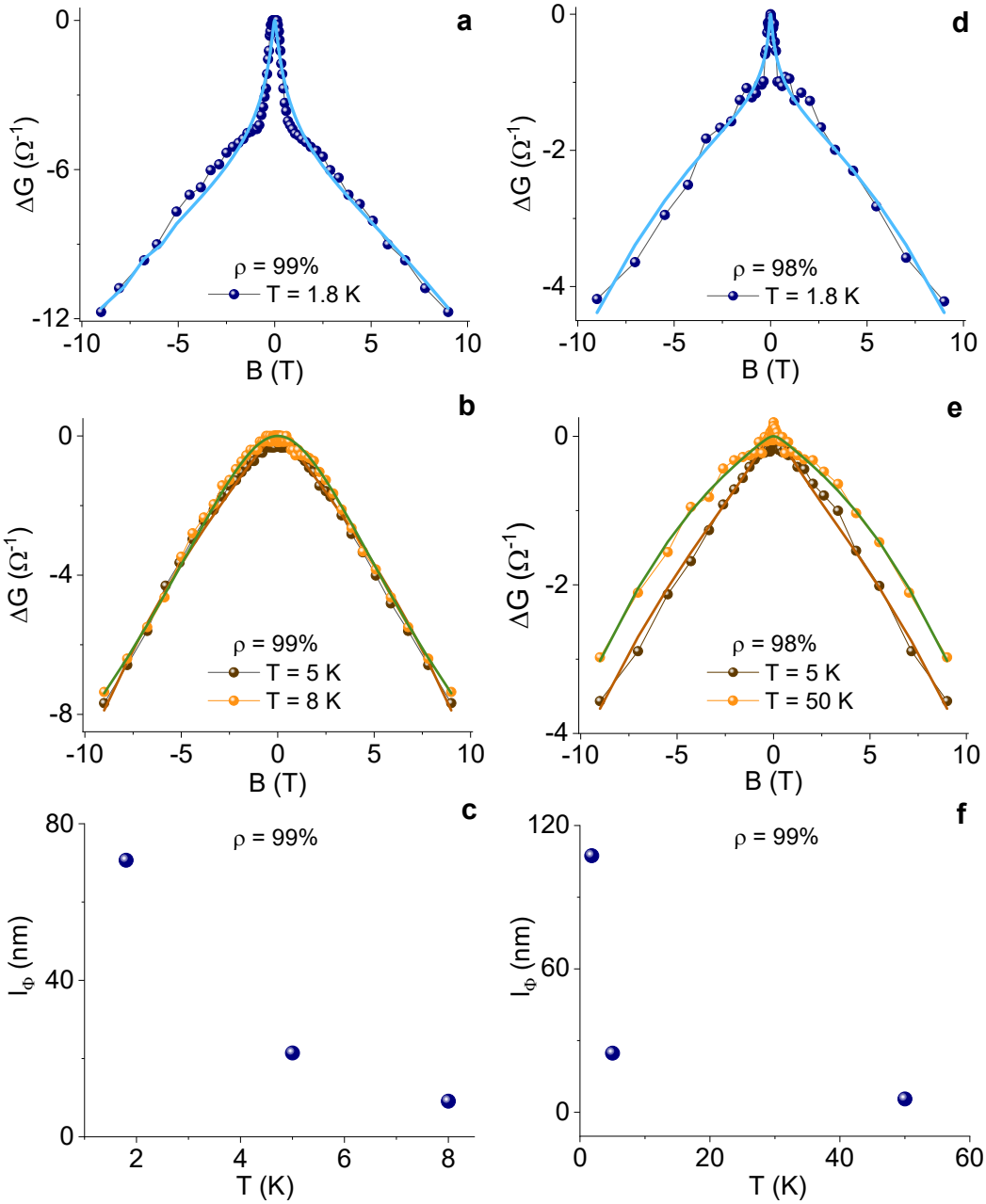

Fig.45: ΔG fitting of SS22-02 and SS22-03 compacted pellets using HLN approach (eq.34). (a)-(b) ΔG of SS22-02 sample at three different temperatures of $1.8\ K$, $5\ K$ and $8\ K$ versus magnetic field of $-9\ T$ to $9\ T$. (d)-(e) ΔG of SS22-03 sample at three different temperatures of $1.8\ K$, $5\ K$ and $50\ K$ versus magnetic field of $-9\ T$ to $9\ T$. l_ϕ versus temperature of (c) SS22-02 and (f) SS22-03 compacted nanoparticles.

Fitting parameters of l_ϕ and α for SS22-02 and SS22-03 compacted nanoparticles are collected in table.8. Considering multiple scattering channels (eq.34) as well as significant bulk carrier contribution into the transport signal, α can be assumed much higher.

Therewith, α values in the order of 10^5 were calculated whose order of magnitude is the same as that of Bi_2Te_3 single crystalline[152].

Compared to the α values of classical approach, the current values increased three orders of magnitudes elucidating synthesis-based electrical transport properties.

Table.8: Fitting parameters of SS22-02 and SS22-03 compacted pellets at temperatures of $1.8\ K$ and $5\ K$.

Sample name	$l_\phi\ (nm)$		α	
	$1.8\ K$	$5\ K$	$1.8\ K$	$5\ K$
SS22-02	70	22	1.2×10^5	1.1×10^5
SS22-03	107	28	2.4×10^5	5.3×10^5

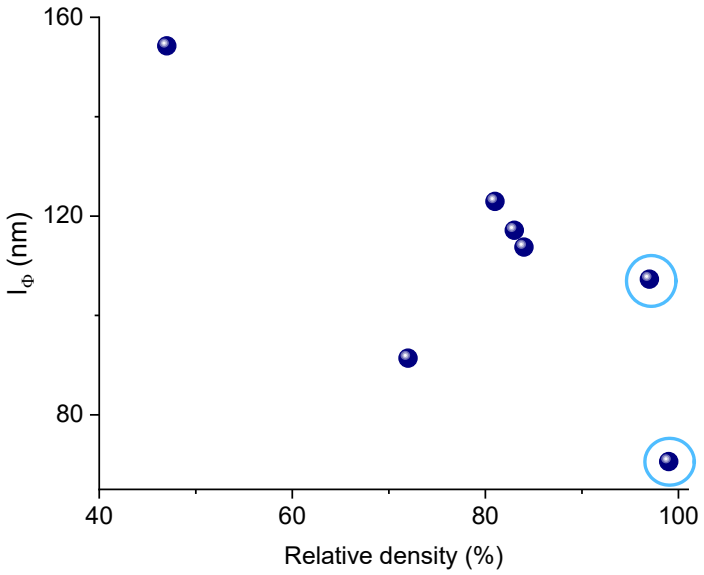

Fig.46: l_ϕ of Bi_2Te_3 compacted pellets versus relative sample density of two different chemical approaches (samples of developed synthesis approach are marked with blue circles).

4.3.4.2. Hall measurement

The results of Hall transport characterization at temperatures of $1.8\ K$, $5\ K$, $50\ K$, $100\ K$ and $300\ K$ are demonstrated in Fig.47. Negative Hall measurement slope of SS22 samples specifies n-type carrier transport within the Bi_2Te_3 compacted nanoparticles.

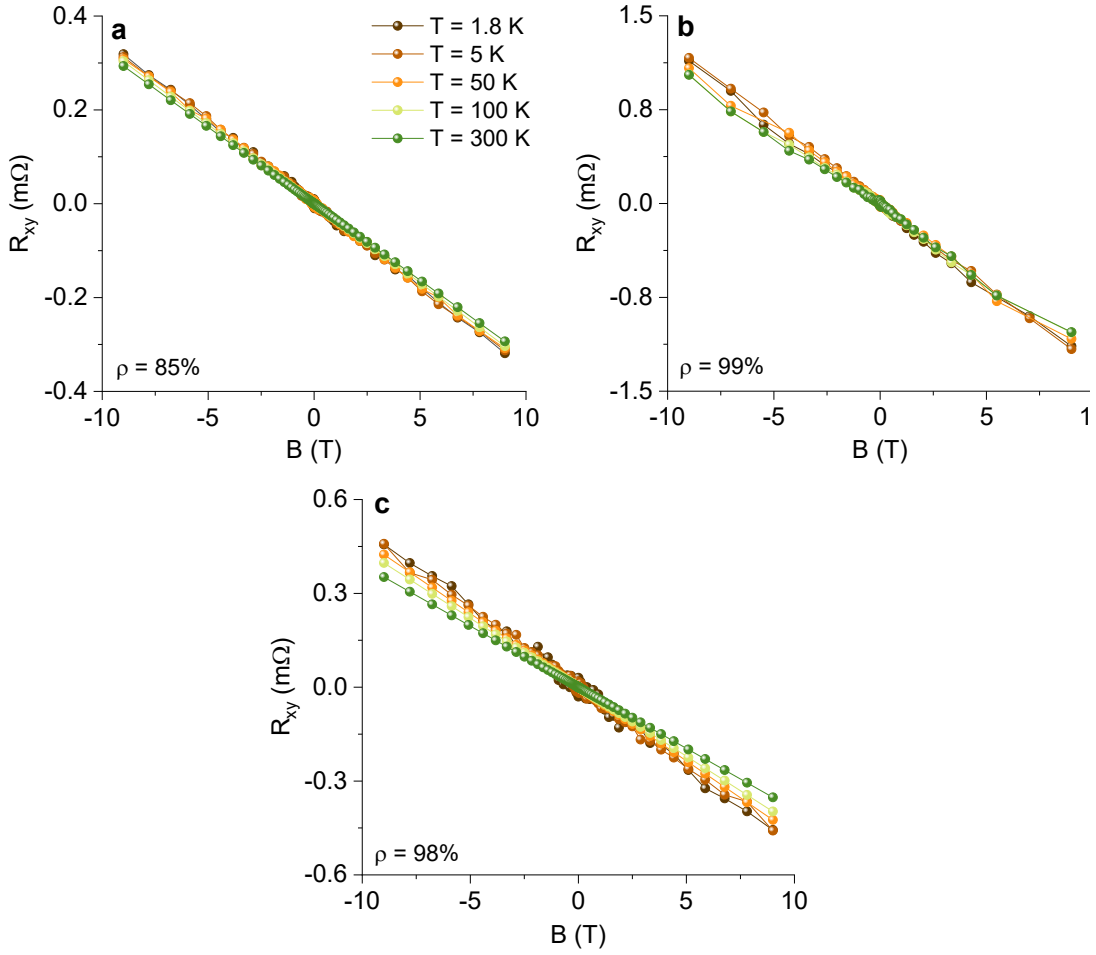

Fig.47: Hall measurement of (a) SS22-01, (b) SS22-02 and (c) SS22-03 compacted pellets over magnetic field of $-9\ T$ to $9\ T$ at temperatures of $1.8\ K$, $5\ K$, $50\ K$, $100\ K$ and $300\ K$.

n and μ of SS22 compacted pellets were calculated using Hall transport characterization; the corresponding results are demonstrated in Fig.48. Hall measurements revealed charge carrier density in the order of $10^{20}\ cm^{-3}$ as well as charge carrier mobility of $\sim 30\ cm^2V^{-1}s^{-1}$ at room temperature which are predominately related to the bulk transport channel. Similar to the classical approach, n decreased followed by temperature reduction down to $1.8\ K$ associating with carrier freeze out effect (Fig.48 (a)) where the values are preserved in the order of 10^{20} over the whole temperature interval. Compared to n values of 10^{19} at $1.8\ K$ of SS2 compacted pellets (Fig.38 (a)), the corresponding values were increased one order of magnitude for Bi_2Te_3 compacted pellets of current chemical approach.

In contrast, as demonstrated in Fig.48 (b), μ values of the compacted pellets were increased with decreasing temperature. Compared to μ values of SS2 compacted pellets of $\sim 20\ cm^2/Vs$ at $1.8\ K$

(Fig.38 (b)), the corresponding values increased ranging from $\sim 30\ cm^2/Vs$ up to $\sim 80\ cm^2/Vs$ which is in accordance with the improved sample degree of compaction together with higher n values.

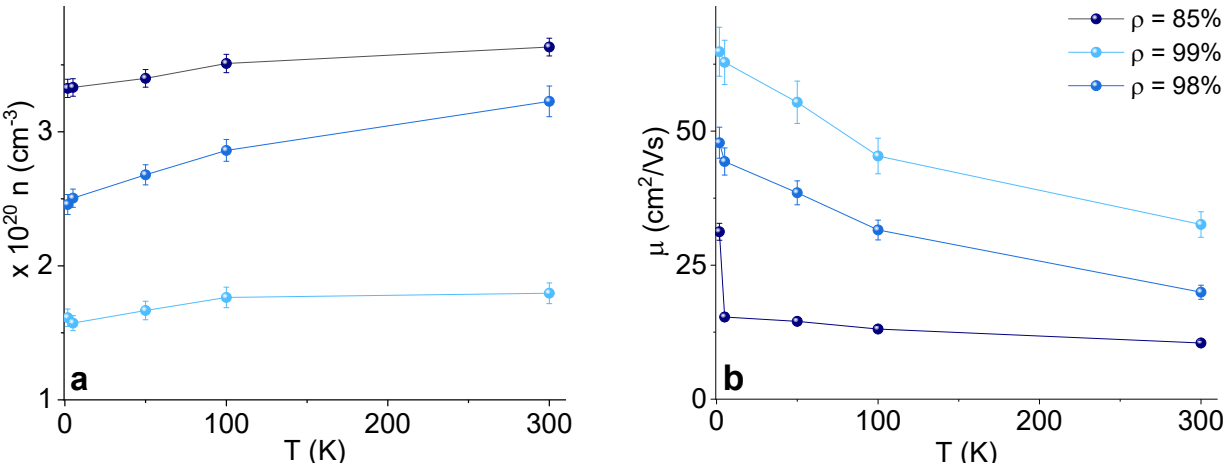

Fig.48: (a) n and (b) μ of SS22 compacted pellets in temperature range of $300 - 1.8\ K$.

4.3.5. Results of Terahertz time-domain spectroscopy

The findings presented so far give some evidences of surface transport mechanism within the nanograined bulk material. As was mentioned in Hall transport characterization, still surface carriers are outnumbered by majority of bulk carrier contribution.

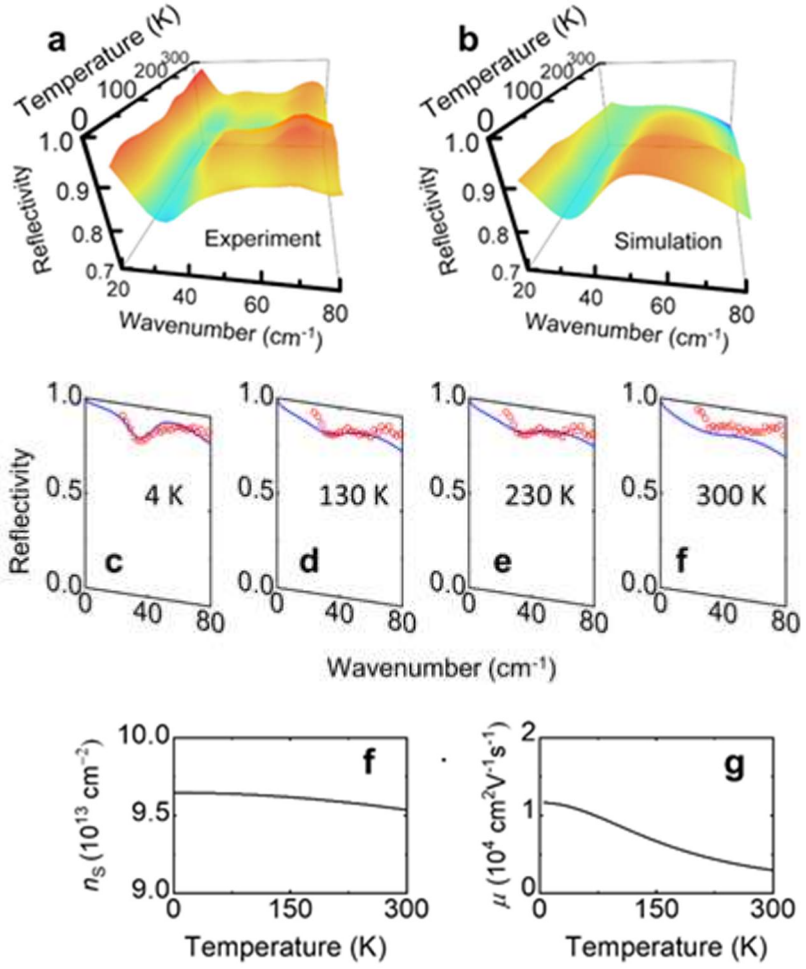

Fig.49: Experimentally obtained reflectivity (a) as a function of the wavenumber and temperature in the range of $4\ K$ to $300\ K$. (b) Calculated reflectivity with consideration of bulk and surface Drude conductivity as well as the surface plasmonic contribution. (c)-(f) Measured (red) and calculated (blue) reflectivity as a function of frequency for temperatures of $4\ K$, $130\ K$, $230\ K$, and $300\ K$, respectively. Surface carrier concentration (g) and mobility (h) extracted from the model as a function of temperature.

Superconducting-like ρ behavior as well as evidence of quantum interference transport at low temperatures of SS22 compacted nanoparticles stimulated further experimental investigation. The individual contributions of surface and bulk transport channels were elucidated in more detail by THz time-domain spectroscopy[169-173].

In the following section THz time-domain spectroscopy measurements of SS22-04 bulk pellet conducted by THz group at University of Duisburg-Essen is provided.

First, a short THz pulse that was generated by a photoconductive antenna guided to the sample with two parabolic mirrors. The reflected THz radiation was collected by another set of parabolic mirrors and focused to the detector. Sample reflectivity as a function of temperature and wavenumber is illustrated in Fig.49 (a). As demonstrated in the figure, a clear reflectivity dip appeared at wavenumber of $\sim 35\ cm^{-1}$ followed by temperature reduction down to $4\ K$. Similar intrinsic THz plasmons occur in graphene layers with natural nanoscale inhomogeneities[174].

For further analysis of the obtained spectra, a model consisting of three contributions of free carrier absorption by surface and bulk carriers as well as plasmonic contribution of surface carriers into the total σ was employed (eq.35). The latter contribution is attributed to collective charge carrier oscillations due to the microscopic structure of the Bi_2Te_3 nanoparticles. Therewith, as soon as the frequency of the electric field is resonant to the plasmon, a strong increase in light-matter interaction occurs.

$$\sigma_T = \sigma_{\mathrm{f}}^{\mathrm{B}} + \sigma_{\mathrm{f}}^{\mathrm{S}}(\omega) + \sigma_{\mathrm{P}}^{\mathrm{S}}(\omega) \qquad (35)$$

Based on the presented model first, the THz conductivity of the bulk carriers (σ_f^B) was calculated via Drude model represented in eq.36 where n_B represents bulk carrier concentration which was taken from Hall measurements; e, τ_B and m^* specify the elementary charge, momentum scattering time of bulk carriers and effective mass respectively. The value of 0.07 of electron mass was considered as m^* in the calculation[175-176]. In addition, the introduced scaling factor of p' into the bulk conductivity formula stands for not having a perfect bulk crystal structure; the best match of the employed model and obtained reflectivity spectra was found at $p' = 0.3$.

$$\sigma_{\mathrm{f}}^{\mathrm{B}}(\omega) = \frac{\mathrm{n_B p' e^2 \tau_B}}{\mathrm{m^*}}\left(\frac{1}{1-\mathrm{i}\omega\tau_{\mathrm{B}}}\right) \qquad (36)$$

The next contribution which is demonstrated in eq.37 accounts for surface Drude conductivity (σ_f^S); The formula slightly differs from eq.36 where n_S, V_F and γ_S specify surface carrier concentration, Fermi velocity and surface scattering rate respectively,

$$\sigma_f^S(\omega) = \frac{iq'e^2\sqrt{\pi n_S}v_F}{\pi\hbar(i\gamma_S+\omega)} \quad (37)$$

The represented parameter of q' in eq.37 serves as fitting parameter into Drude surface conductivity so that the amount of $2 \times 10^2 cm^2/cm^3$ was extracted as the optimized fitting parameter value. The corresponding value which is one per mill of the obtained value by BET measurements (table.7), accounts for the fact that most surfaces and interfaces will not be part of a percolating 3D network which is in qualitative agreement with the conducted Conductive-AFM measurement (Fig.42).

n_S of SS22-04 sample at different temperatures was extracted using Bi_2Te_3 band structure[177] as well as bulk carrier concentration of n_B. Taking Hall carrier concentration value at temperature of $2\ K$, E_F of Bi_2Te_3 compacted nanoparticles turned out to be placed $0.27\ eV$ above the DP and $0.05\ eV$ above CB minimum (Fig.50) which is in good agreement with literature value[5].

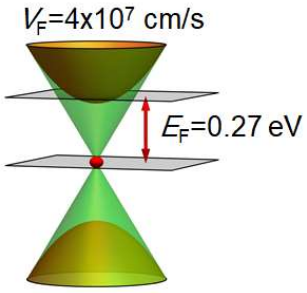

Fig.50: Schematic illustration of Bi_2Te_3 band structure; E_F of Bi_2Te_3 compacted nanoparticles is located 0.27 eV above the DP.

$D(E)$ and $f(E, E_F)$ represented in eq.38 stand for DOS and Fermi-Dirac distribution function respectively; DOS was taken from the previous calculation[177].

$$\int_{E_c}^{\infty} D(E)\times f(E,E_F)dE + \int_{-\infty}^{E_c} D(E)\times(1-f(E,E_F))dE = n_H\ (2\ K) \quad (38)$$

Temperature-dependent chemical potential ($\mu'(T)$) can be estimated using carrier conservation law. Therewith, one can calculate n_S using eq.39 where $D_{2D}(E)$ specifies DOS of surface Drude carriers with linear dispersion relation (eq.40),

$$n_S = \int_0^{\infty} \mathrm{D_{2D}(E)} \times \mathrm{f(E,\mu'(T))dE} \quad (39)$$

$$\mathrm{D_{2D}(E)} = \frac{2|\mathrm{E}|}{\pi \hbar^2 \mathrm{v_F^2}} \quad (40)$$

Assuming V_F of $4 \times 10^7 cm/s$[178], the surface carrier density was calculated to be $\sim 9.6 \times 10^{13} cm^{-2}$ which is only slightly depends on the temperature (Fig.49 (f)).

The scattering rate of the surface carriers (γ_S) is connected to the momentum lifetime of τ_S via $\tau_S = 1/\gamma_S$. The temperature dependent γ_S was calculated using eq.41 where γ_0 and A serve as fitting para meters[179].

$$\gamma_S = \gamma_0 + AT^2 \quad (41)$$

The proportionality factors of A and γ_0 were calculate as 3.33×10^{-4} and 10 respectively.
Using eq.41, temperature-dependent μ of the compacted nanoparticle was calculated using eq.42,

$$\mu = e \times \frac{V_F}{\sqrt{n\pi}(\gamma_0 + AT^2) * \hbar} \quad (42)$$

According to the corresponding result demonstrated in Fig.49 (g), μ of the surface carriers reaches the value of $\sim 1.2 \times 10^4\ cm^2 V^{-1} s^{-1}$ followed by temperature reduction.
This μ value which agrees well with the previous reports[52-53, 160], emphasizes on high quality of Bi_2Te_3 nanoparticles.
Finally, the plasmonic contribution of σ_P^S stimulates the obtained reflectivity-dip in the spectra demonstrated in Fig.49 (a). The plasmonic response originating from microscopic structure of the Bi_2Te_3 nanoparticles, was incorporated within the model using modified Drude formula[180],

$$\sigma_P^S(\omega) = \frac{\mathrm{iq'e^2}\sqrt{\pi \mathrm{n_S}}\mathrm{v_F}}{\pi\hbar(\mathrm{i}\gamma_S + \frac{\omega^2 - \omega_P^2}{\omega})} \quad (43)$$

ω_P represents the plasmon frequency of $1.35\ THz$, which served as a free parameter to fit the calculated results to the experimentally obtained values. The plasmon frequency of ω_p depends on the lateral dimensions of the microscopic structure as well as the carrier density[181].
To calculate reflection spectrum of three different conductivity channels (σ_f^B, σ_f^S and σ_P^S), the frequency dependent permittivity (ε) was calculated using eq.44 where ε_0 and ε_∞ specify vacuum

permittivity and background permittivity, respectively, based on previous reports[182] the value of 64 was considered as ε_∞,

$$\varepsilon(\omega)=\varepsilon_\infty+\frac{i(\sigma_f^S+\sigma_f^B+\sigma_P^S)}{\omega\varepsilon_0} \quad (44)$$

According to eq.45, sample reflectivity of R can be obtained; $\tilde{n}$ specifies complex refractive index,

$$\tilde{n}=\sqrt{\varepsilon_{tot}}, \quad R=\left(\frac{\tilde{n}-1}{\tilde{n}+1}\right)\left(\frac{\tilde{n}-1}{\tilde{n}+1}\right)^* \quad (45)$$

The calculated temperature- and wavenumber-dependent R is shown in Fig.49 (b) which is completely in accordance with the experimentally measured spectra of represented in Fig.49 (a). For a better quantitative comparison, the calculated spectra (blue curves) at four distinct temperatures of $4\ K$, $130\ K$, $230\ K$ and $300\ K$ over wavenumber interval of $0-80\ cm^{-1}$ are compared with the red experimental data (Fig.49 (c)-(f)).

4.3.5.1. Transport contribution disentanglement

The interplay of the three conduction mechanisms is rather complex as the weight of each to overall σ depends not only on the temperature, but also on the frequency. To provide a better insight to the role of each conduction channel, the ratio of these contributions were calculated at fixed frequency as a function of temperature; the corresponding results are discussed in the following.

The ratio of three conduction mechanisms at three different frequencies of DC, $0.75\ TH$, and $1.5\ THz$ are compared as a function of temperature (Fig.51). As can be seen in Fig.51 (a), the plasmonic contribution is zero for DC measurement and increases with frequency as it gets closer to resonance. The surface Drude contribution is decreasing upon increasing temperature for the DC case, which is related to the increase of scattering rate. With increasing frequency the surface carrier contribution decreases, which is related to the overall low scattering rate, i.e. the high scattering rate of the bulk carriers leads to a rather flat behavior while the role of the surface carriers decreases. It is worth to mention that the experimental data is only accessible in a limited frequency range and the values for DC case are extrapolated, leading to a small uncertain <ty. Nevertheless it is supposed to be helpful to understand the role of the surface carriers in general.

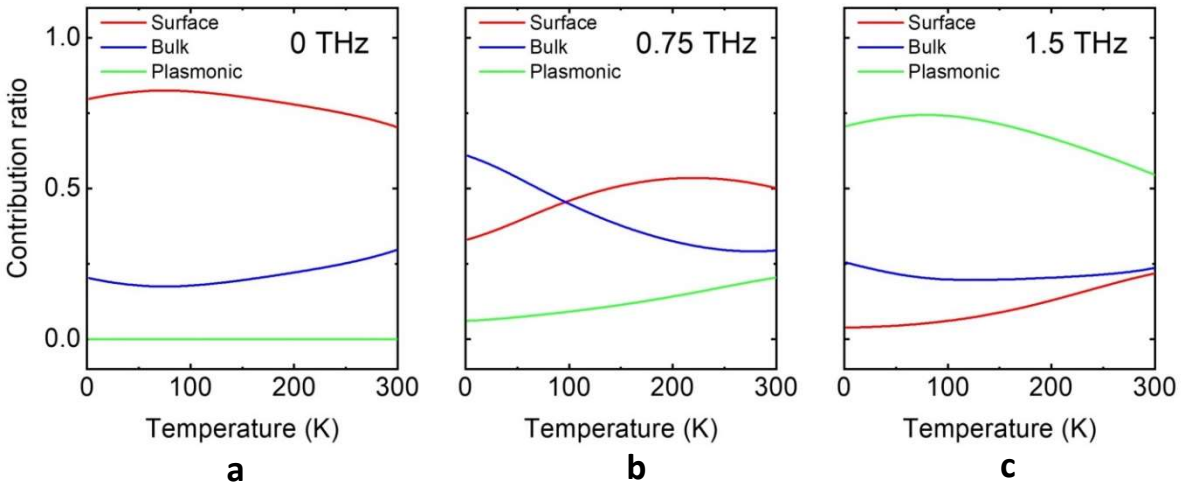

Fig.51: Contribution ratio for the three different conduction mechanisms, i.e. surface and bulk Drude conduction as well as surface plasmonic conduction is plotted as a function of temperature at (a) DC, (b) $0.75\ THz$ and (c) $1.5\ THz$.

The characteristic dip at $35\ cm^{-1}$ cannot be reproduced by only considering surface and bulk Drude contributions, but instead requires a resonant behavior connected to high μ carriers. Such high μ can be excluded from bulk carriers yet is offered in the sub-system of surface carriers.

Chapter.5

Results of Thermoelectric characterization

Introduction

Synthesis-based TE properties of Bi_2Te_3 bulk materials are represented and discussed in this chapter; therewith, S, σ, PF and k of Bi_2Te_3 compacted nanoparticles of each chemical approach has been identified and the corresponding results of both approaches are compared with each other.

5.1. Sample overview

Aiming at TE characterization, Bi_2Te_3 nanoparticles with majority particle size distribution of $\sim 40-70\ nm$ and $\sim 20-80\ nm$ for classical and developed synthesis approaches, respectively, can easily agglomerate resulting in closely-compacted Bi_2Te_3 nanoparticles.

A classification of Bi_2Te_3 bulk pellets whose TE properties were characterized is provided in table.9. Therewith, two samples of each nanoparticle batch (SS2 and SS22) were fabricated with ρ' values of $\sim 80\%$ and $\sim 99\%$ respectively. According to the table, pressure of $2\ kN$ was applied during Bi_2Te_3 nanoparticles compaction. Subsequently, highly-dense Bi_2Te_3 bulk pellets were triggered by applying sintering temperature of $\sim 320\ ^{\circ}C$ and $\sim 300\ ^{\circ}C$ for SS2 and SS22 nanoparticles respectively.

Table.9: list of Bi_2Te_3 compacted bulk pellets and corresponding compaction parameters.

Batch name	Sample name	$m \pm 0.001$ (mg)	$d \pm 0.001$ (mm)	T_1 ($^{\circ}C$)	T_2 ($^{\circ}C$)	ρ (gr/cm^3)	ρ' (%)
SS2	SS2-06	61.2	0.48	320	300	6.5	85
	SS2-07	66.5	0.53	320	306	6.4	83
SS22	SS22-P1	79.4	0.54	300	280	7.5	98
	SS22-P2	76	0.51	300	288	7.6	99

Densities of Bi_2Te_3 bulk pellets of classical approach did not exceed for more than $\sim 85\%$ which is most likely originated from the residual contaminations on nanoparticles surfaces (Fig.25-26). Comparable density as high as $\sim 87\%$ was reported for Bi_2Te_3 bulk pellet of compacted nanoparticles which were synthesized in presence of the capping agent of alkane thiol[183].

TE characterization of compacted Bi_2Te_3 nanoparticles was carried out for in-plane crystallographic orientation. However, k of the samples was characterized for both in-plane and cross-plane directions.

5.2. Thermoelectric characterization

5.2.1. Seebeck coefficient and electrical conductivity characterization

TE characterization of Bi_2Te_3 compacted nanoparticles of two synthesis-based approaches are represented in Fig.52; where TE properties including S, σ, PF and ZT were measured under Ar atmosphere in temperature range of $30\,^{\circ}C$ up to $240\,^{\circ}C$.

As represented in Fig.52, TE properties of different approaches follow similar behavior over temperature range of $30\,^{\circ}C$ up to $240\,^{\circ}C$ specifying reproducibility and reliability of the measurements.

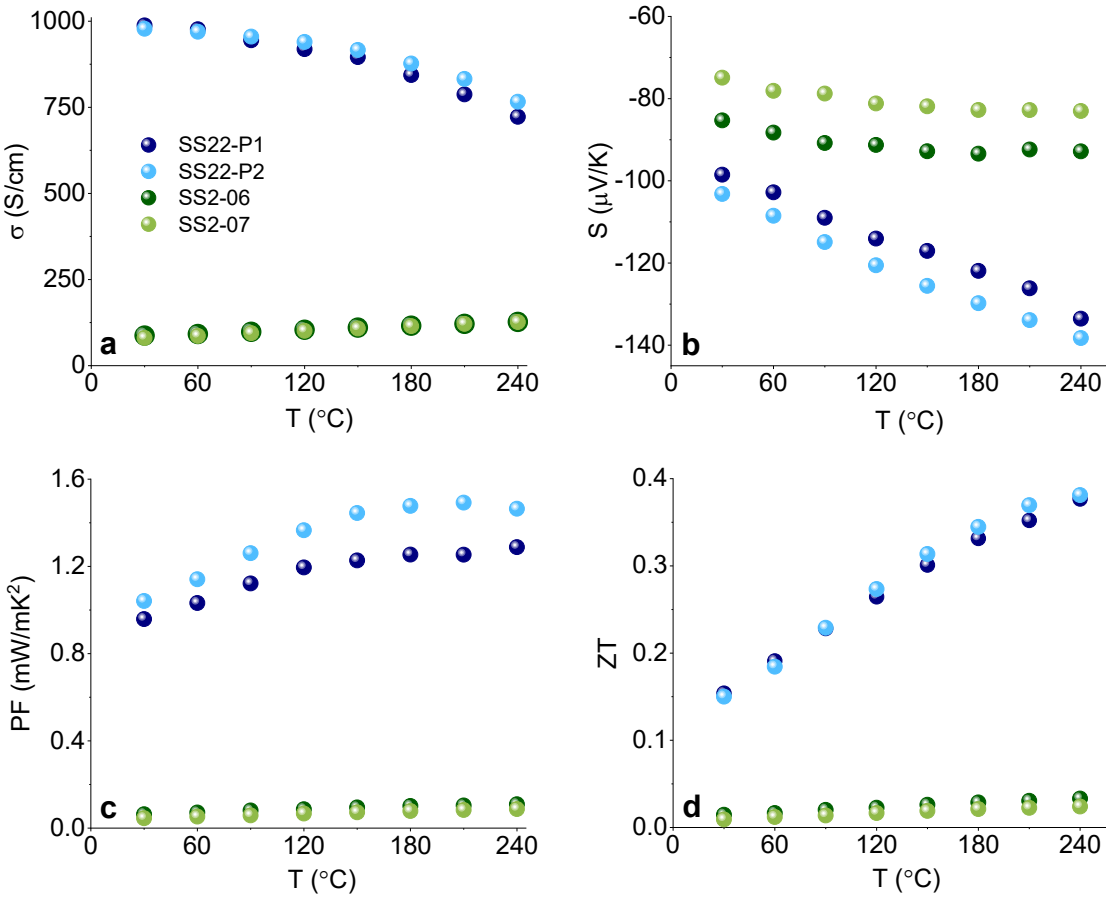

Fig.52: Comparison of (a) S (b) σ (c) PF and (d) ZT of compacted Bi_2Te_3 nanoparticles which were synthesized by two different chemical approaches; green and blue colors specify classical and developed synthesis approach respectively.

According to Fig.52 (a), σ of SS2 compacted nanoparticles revealed low values of $\sim 100\ Scm^{-1}$ over the whole temperature interval that can be attributed to the detected organic substance of OA surrounding Bi_2Te_3 nanoparticles (Fig.25-26). In contrast, electrical transport contribution of Bi_2Te_3 compacted nanoparticles of developed synthesis approach, improved dramatically; therewith, σ of SS22 compacted pellets revealed ~ 12-fold increase at temperature of $30^{\circ}C$ compared to SS2 compacted pellets resulting from Bi_2Te_3 nanoparticles of neither contaminated with organic surfactants nor with elemental Te.

As demonstrated in Fig.52 (a), σ of SS22 compacted nanoparticles revealed a decreasing trend from $\sim 990\ Scm^{-1}$ value down to $\sim 720\ Scm^{-1}$ upon temperature enhancement. *Tang et. al.* reported σ in the same order of magnitudes for layered Bi_2Te_3 nanostructure which was prepared by melt spinning and spark plasma sintering techniques. Moreover, σ of that work follows the same trend with temperature enhancement[103]. However, σ of SS2 compacted pellets follows an opposite temperature dependence where, σ increased upon temperature enhancement varying in the range of $\sim 88\ Scm^{-1}$ up to $\sim 127\ Scm^{-1}$.

It is worth to mention that further porosity reduction of SS2 compacted pellets will more likely improve the electrical transport contribution; however, the resulting values would be more likely still much lower compared to the corresponding values of SS22 compacted pellets.

Compared to the reported value of $12.2\ Scm^{-1}$ for 99.99% Bi_2Te_3 bulk material[183], dramatic σ improvement of this work which is comparable to the σ values of highly crystalline Bi_2Te_3 nanostructure[103] emphasizes on key importance of the synthesis-based material design strategy.

Negative S values of Bi_2Te_3 compacted nanoparticles (Fig.52 (b)), elucidates n-type carrier transport mechanism and agrees well with Hall transport characterization (Fig.37 and 47). The measured S of two different approaches relies on the same trend where S increases followed by temperature reduction with the measured maximum value of $\sim -138\ \mu V/K$ and $\sim -92\ \mu V/K$ for SS22 and SS2 compacted pellets at temperature of $30^{\circ}C$ respectively. S of SS22 compacted samples, being slightly lower compared to the intrinsic Bi_2Te_3[67], is in accordance with high n values in the order of $10^{20}\ cm^{-3}$ (Fig.48 (a)).

In contrast, lower S values of SS2 compacted samples are more likely attributed to excess elemental Te (table.3). According to the previous report[184], Bi/Te ratio of $Bi_{2-x}Te_{3+x}$ compound associates directly with material S value.

The overall contribution of S and σ into material PF is elucidated in Fig.52 (c). By raising temperature up to $240^{\circ}C$, PF of SS22 compacted pellets increased in range of $0.95 - 1.46\ mW/mK^2$, however, PF of SS2 compacted samples varied in the range of $0.04 - 0.1\ mW/mK^2$.

The enhanced PF values of SS22 compacted nanoparticles with a maximum value at temperature of $\sim 200\,^{\circ}C$ are mainly attributed to the improved Bi_2Te_3 nanoparticles σ.

5.2.2. Thermal conductivity characterization

Bi_2Te_3 nanograined bulk material contains high number of interfaces and grain boundaries which are specifically favored for lattice thermal conductivity (k_l) suppression; according to TEM images represented in Fig. 36 and 39, randomly oriented atomic lattice fringes can dramatically decrease k_l.

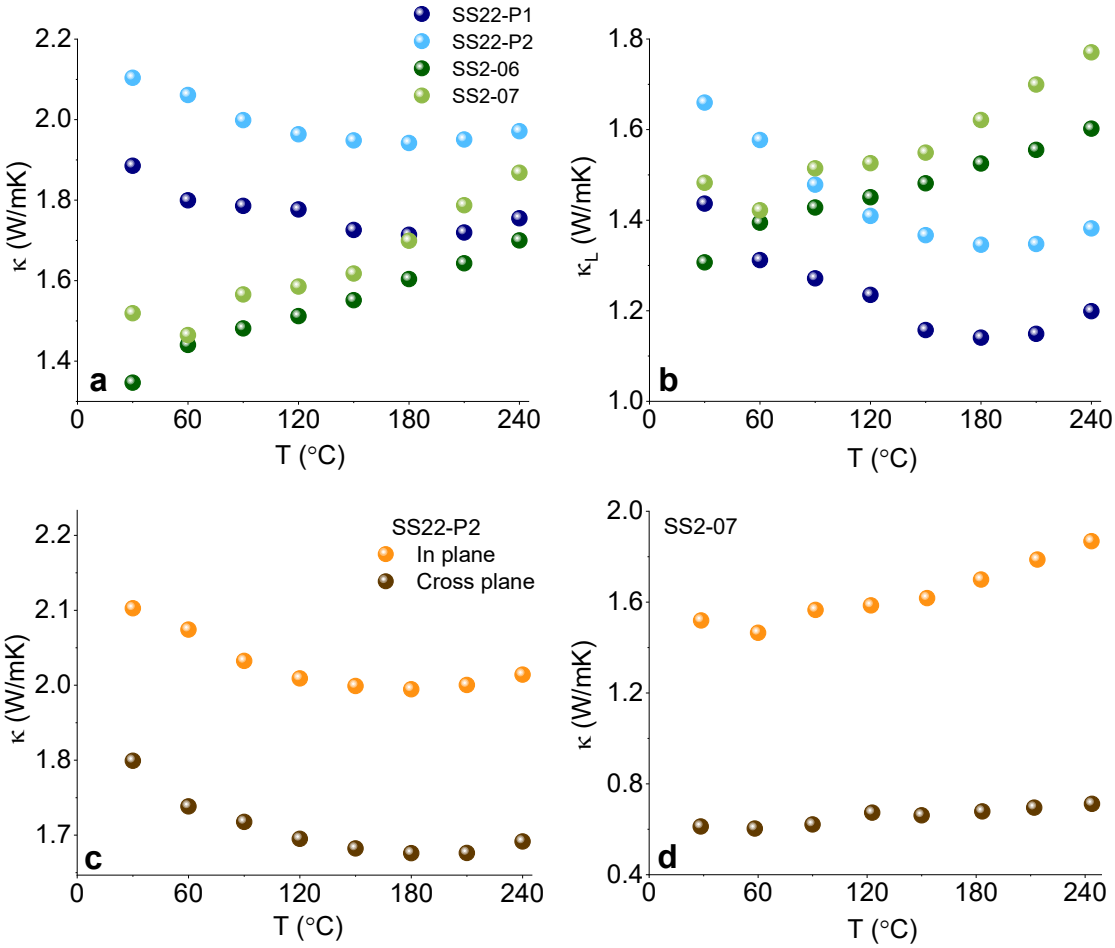

Fig.53: k characterization of Bi_2Te_3 compacted nanoparticles: (a) Total k (b) k_l of SS22 and SS2 compacted samples (green and blue colors specify SS2 and SS22 compacted samples respectively). Comparison of $k_{\perp}$ and $k_{\parallel}$ of (c) SS22-P2 and (d) SS2-07 compacted nanoparticles (brown and orange colors represent $k_{\parallel}$ and $k_{\perp}$ respectively).

k characterization of Bi_2Te_3 compacted samples are illustrated in Fig.53. According to Fig.53 (a), low amounts of k of SS2 compacted nanoparticles up to $\sim 150\,^{\circ}C$ can be attributed to excess elemental-

Te and considerable amounts of porosity within the material (ρ' of $\sim 85\%$) resulting in effective phonon scattering mechanism. However, these can be regarded as deteriorating factors for electrical transport contribution (Fig.52 (a)).

Considering theoretical value of l_0 ($1.5 \times 10^{-8}\ V^2K^{-2}$)[103], k_l of Bi_2Te_3 compacted bulk pellets was calculated using Wiedemann-Franz law (eq.14); the corresponding results are represented in Fig.53 (b) where the calculated k_l values of SS22 compacted nanoparticles at temperatures higher than $\sim 100\,^{\circ}C$ decreased compared to the corresponding values of SS2 compacted pellets; therewith, one can conclude with higher phonon scattering mechanism within SS22 compacted nanoparticles at higher temperature regime.

Moreover, electrical and thermal transport properties can be disentangled to some extent in SS22 compacted nanoparticles. As was already discussed in SEM morphological analysis, SS22-03 compacted pellet consists of both nano- and micro-sized particles; while μm-length surfaces facilitate electron transport contribution, thermal transport can be suppressed via nano-sized particle distribution (Fig. 41). This reason more likely explains higher amount of σ along with the reduced k values of SS22 compacted nanoparticles for temperatures higher than $\sim 100\,^{\circ}C$.

Interestingly, despite the obvious nanostructured texture of the pellets, k_l values of SS22 compacted samples are in close agreement with those reported for Bi_2Te_3 single crystals[185] and with values obtained using ab initio calculations[186]. The ratio of k between the crystallographic c-axis and a-b plane of Bi_2Te_3 single crystalline is also close to the one obtained in SS22 pellet between the pressing direction and its perpendicular plane (Fig. 53(c))[82]. Comparable k values with those of single crystalline emphasizes on high quality of Bi_2Te_3 nanoparticles together with reliability of the synthesis-based material design strategy.

Anisotropic crystalline configuration of Bi_2Te_3 compacted pellets can be well recognized by different amounts of $k_{\parallel}$ and $k_{\perp}$ measured for SS22 and SS2 compacted nanoparticles (Fig.53 (c)-(d). This result is consistent with anisotropic orientation of Bi_2Te_3 nanoparticles which was demonstrated by SEM morphological analysis (Fig.28 and Fig.41).

The values of k parallel to the pressing direction of both approaches are smaller compared with k perpendicular to the pressing direction. The anisotropy ratio of κ is 1.1 and 2 for SS22-P2 and SS2-07 respectively.

As demonstrated in X-Ray diffractograms of Fig.54, pronounced Bragg reflections of $00l$ $(l = 3, 6, ..)$ planes was revealed for perpendicular measurement to the pressing direction of SS22-P2 sample. However, these Bragg reflections were not detected in parallel measurement to the pressing direction. Therewith, one can conclude that morphological configuration of the sample favors parallel crystallographic alignment of Bi_2Te_3 nanoparticles which are perpendicularly aligned to the

pressing direction. Therefore, the measured $k_{\parallel}$ values of Bi_2Te_3 compacted samples are smaller compared to the corresponding $k_{\perp}$ values.

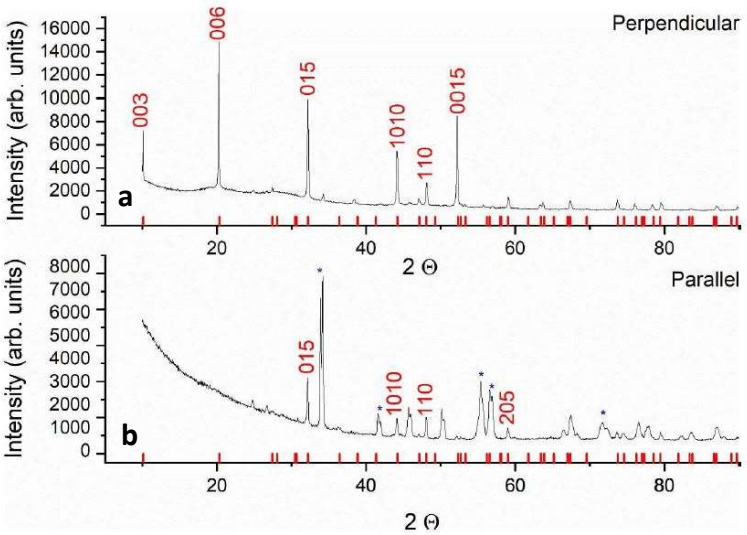

Fig.54: X-ray diffractogram of SS22-P1 pellet perpendicular and parallel to the pressing direction. The positions of the Bragg reflections of Bi_2Te_3 are shown as red bars as reference (Reflections from sample holder are marked with a blue star).

5.2.3. ZT characterization

Finally, dimensionless ZT of Bi_2Te_3 compacted nanoparticles were calculated using eq.10. According to Fig.52 (d), the calculated ZT values of Bi_2Te_3 compacted nanoparticles increased monotonically upon temperature enhancement with maximum ZT values of 0.38 and 0.03 for SS22-P2 and SS2-06 compacted pellets respectively. As demonstrated in Fig.52 (d), ZT values of Bi_2Te_3 bulk samples of developed synthesis approach are one order of magnitudes larger than classical approach which is mainly attributed to the enhanced σ of Bi_2Te_3 nanoparticles. Hereby, one can conclude that the improved TE performance of the SS22 Bi_2Te_3 bulk samples originates exclusively from high quality Bi_2Te_3 nanoparticles with low levels of impurities and surface contamination.

Summary and outlook

Topologically-protected surface states offer a variety of outstanding properties that are promising for many technological applications, e.g. spintronics or thermoelectricity. With increasing size, it gets more and more difficult to observe surface states as it is challenging to distinguish between surface and bulk carriers, which tend to dominate the electronic properties of large-scale samples. This work shows an accessible and pragmatic way of producing microscopic topological insulating materials that have a clear signature of the surface states and may pave the path towards the fabrication of TI materials, even on an industrial scale. The key to obtaining the samples is to synthesize nanoparticles with clean surfaces and to preserve the nanoparticle character in the bulk.

In summary, electrical transport and TE properties of Bi_2Te_3 bulk samples consisting of high quality tailored-based Bi_2Te_3 nanoparticles which were synthesized using ionic liquids, were investigated. Nanoparticle-based design strategy was successfully applied for the Bi_2Te_3 compacted nanoparticles of two different chemical approaches using hot pressing technique.

Interestingly, sample degree of compaction (density) and specific chemical synthesis were realized as determinative factors of defining governed transport mechanism of the Bi_2Te_3 compacted bulk material. Compared to Bi_2Te_3 compacted nanoparticles of classically-synthesized approach specifying nonmetallic ρ trend upon temperature reduction, compacted Bi_2Te_3 samples of developed synthesis approach exhibited metallic transport behavior followed by a superconducting-like ρ drop at temperatures below $5\ K$.

Suppression of bulk transport channel in a Bi_2Te_3 bulk material was triggered conceptually by tailor-based material design strategy where two effective approaches of porosity as well as large μm-length surface design concepts were successfully applied into the Bi_2Te_3 compacted nanoparticles of classical and developed approach, respectively, resulting in significant surface-to-volume ratio improvement. Therewith, high amount of free surfaces of $10^4\ cm^2 g^{-1}$ and $10^5\ cm^2 g^{-1}$introduced within the material.

Indications of surface transport carriers were realized using magneto-transport measurement technique. Loosely-contacted Bi_2Te_3 nanoparticles with preserved shape of the initial powder (Bi_2Te_3 nanoporous bulk material) revealed high l_ϕ value of $\sim 154\ nm$ along with the sharpest ρ dip. Basically, samples of both approaches revealed indication of destructive quantum interference known as WAL effect at low temperatures and small magnetic fields, however, the realized quantum interference of each category relied on distinct HLN models elucidating the synthesis-based electrical transport properties.

For that reason, time-domain THz spectroscopy was effectively employed so that dominance of the surface transport at low frequencies with a major contribution to the DC transport with a μ of above $10^3\ cm^2V^{-1}s^{-1}$ even at room temperature for Bi_2Te_3 compacted nanoparticle of developed synthesis approach were realized. In the meanwhile, distinct transport contributions of bulk and surface Drude conductivity as well as plasmonic surface carriers of the Bi_2Te_3 compacted nanoparticles were mathematically specified and contribution ratio of those conductivities were defined as a function of temperature and frequency. Despite the fact that surface carrier density was far below the one of the bulk carriers, it was demonstrated that surface carriers dominate DC transport signal even at room temperature as they accounted for roughly 60% of the total conductivity.

Moreover, Bi_2Te_3 nanoparticles of low levels of impurities and surface contaminations revealed distinct TE features where high S of $-138\,\mu VK^{-1}$ and σ of $720\,Scm^{-1}$ at highest tested temperature of $240\,^{\circ}C$ were realized. The corresponding k is comparable with those of single crystals and ab initio calculations which is in remarkable contrast to typical findings of nanograined bulk materials obtained from the compacted Bi_2Te_3 nanoparticles. If S and σ can be improved further while k value is maintained at least at their present values, ZT in excess of the state-of-the-art will become possible.

While often the investigation of surface states requires atomically clean surfaces of experimental model systems, this work showed that a “real-world” sample actually exhibits the desired properties. These findings set the stage for further utilization of topologically-protected carriers.

References

1. Hasan, M. Z. & Kane, C. L. Colloquium: Topological insulators. *Rev. Mod. Phys.* **82**, 3045–3067 (2010).

2. Qi, X. L. & Zhang, S. C. Topological insulators and superconductors. *Rev. Mod. Phys.* **83**, (2011).

3. Shockley, W. On the surface states associated with a periodic potential. *Phys. Rev.* **56**, 317–323 (1939).

4. Ramakrishnan, T. V. Nobel Prize in Physics 2016. *Resonance* **22**, 781–785 (2017).

5. Zhang, H. *et al.* Topological insulators in Bi_2Se_3, Bi_2Te_3 and Sb_2Te_3 with a single Dirac cone on the surface. *Nat. Phys.* **5**, 438–442 (2009).

6. Neupane, M. *et al.* Topological surface states and Dirac point tuning in ternary topological insulators. *Phys. Rev. B - Condens. Matter Mater. Phys.* **85**, 1–8 (2012).

7. Prange, R. E. *The Quantum Hall effect*. (Springer-Verlag, 1990).

8. Aoki, H. Integer Quantum Hall Effect. *Compr. Semicond. Sci. Technol.* **1–6**, 175–209 (2011).

9. Michel, L. Symmetry defects and broken symmetry. *Rev. Mod. Phys.* **52**, 617–651 (1980).

10. Henle, M. *A combinatorial introduction to topology*. (Dover, 1994).

11.https://www.asiaresearchnews.com/html/article.php/aid/5709/cid/2/research/science/riken/opening_the_door_to_new_forms_of_matter_at_the_condensed_matter_theory_laboratory.html (downloaded at 06.07.2021)

12. den Nijs, M. Quantized Hall conductance in a two dimensional periodic potential. *Phys. A Stat. Mech. its Appl.* **124**, 199–210 (1984).

13. Ando, Y. Topological insulator materials. *J. Phys. Soc. Japan* **82**, 1–32 (2013).

14. Qi, X. L. & Zhang, S. C. The quantum spin Hall effect and topological insulators. *Phys. Today* **63**, 33–38 (2010).

15. Bernevig, B. A. & Zhang, S. Toward dissipationless spin transport in semiconductors. *IBM J. Res. Dev.* **50**, 141–148 (2006).

16. Bernevig, B. A. & Hughes, T. L. Quantum spin hall effect and topological phase transition in HgTe quantum wells. *Science.* **314**, 1757–1761 (2006).

17. Culcer, D., Keser, A. C., Li, Y. & Tkachov, G. Transport in two-dimensional topological materials: recent developments in experiment and theory. *arXiv* (2019).

18. Zhang, F., Kane, C. L. & Mele, E. J. Time-reversal-invariant topological superconductivity and Majorana kramers pairs. *Phys. Rev. Lett.* **111**, 1–5 (2013).

19. Okugawa, R. & Murakami, S. Dispersion of Fermi arcs in Weyl semimetals and their evolutions to Dirac cones. *Phys. Rev. B - Condens. Matter Mater. Phys.* **89**, 1–8 (2014).

20. Arrachea, L. & Aligia, A. A. Unveiling a crystalline topological insulator in a Weyl semimetal with time-reversal symmetry. *Phys. Rev. B - Condens. Matter Mater. Phys.* **90**, 1–7 (2014).

21. He, M., Sun, H. & He, Q. L. Topological insulator: Spintronics and quantum computations. *Front. Phys.* **14**, (2019).

22. Heremans, J. P., Cava, R. J. & Samarth, N. Tetradymites as thermoelectrics and topological insulators. *Nat. Rev. Mater.* **2**, (2017).

23. Seo, J. *et al.* Transmission of topological surface states through surface barriers. *Nature* **466**, 343–346 (2010).

24. Roushan, P. *et al.* Topological surface states protected from backscattering by chiral spin texture. *Nature* **460**, 1106–1109 (2009).

25. Liu, M. *et al.* Crossover between weak antilocalization and weak localization in a magnetically doped topological insulator. *Phys. Rev. Lett.* **108**, 1–5 (2012).

26. He, H. T. *et al.* Impurity effect on weak antilocalization in the topological insulator Bi_2Te_3. *Phys. Rev. Lett.* **106**, 1–4 (2011).

27. Gooth, J., Schierning, G., Felser, C. & Nielsch, K. Quantum materials for thermoelectricity. *MRS Bull.* **43**, 187–192 (2018).

28. Chen, Y. Experimental Realization of a Three-Dimensional Topological insulator Bi_2Te_3. *Science (80-.).* **1173034**, 325 (2009).

29. Müchler, L., Casper, F., Yan, B., Chadov, S. & Felser, C. Topological insulators and thermoelectric materials. *Phys. Status Solidi - Rapid Res. Lett.* **7**, 91–100 (2013).

30. Tian, J. *et al.* Topological insulator based spin valve devices: Evidence for spin polarized transport of spin-momentum-locked topological surface states. *Solid State Commun.* **191**, 1–5 (2014).

31. Herdt, A. *et al.* Spin-polarization limit in Bi_2Te_3 Dirac cone studied by angle- and spin-resolved photoemission experiments and ab initio calculations. *Phys. Rev. B - Condens. Matter Mater. Phys.* **87**, 1–5 (2013).

32. Wang, G. *et al.* Topological insulator thin films of Bi_2Te_3 with controlled electronic structure. *Adv. Mater.* **23**, 2929–2932 (2011).

33. Hsieh, D. *et al.* A topological Dirac insulator in a quantum spin Hall phase. *Nature* **452**, 970–974 (2008).

34. Xiong, J. *et al.* High-field Shubnikov-de Haas oscillations in the topological insulator Bi_2Te_2Se. *Phys. Rev. B - Condens. Matter Mater. Phys.* **86**, 1–6 (2012).

35. Huang, S. M. *et al.* Observation of surface oxidation resistant Shubnikov-de Haas oscillations in Sb_2SeTe_2 topological insulator. *J. Appl. Phys.* **121**, (2017).

36. Zhang, Y. & Vishwanath, A. Anomalous Aharonov-Bohm conductance oscillations from topological insulator surface states. *Phys. Rev. Lett.* **105**, 2–5 (2010).

37. Peng, H. *et al.* Aharonov-Bohm interference in topological insulator nanoribbons. *Nat. Mater.* **9**, 225–229 (2010).

38. Chiu, S. P. & Lin, J. J. Weak antilocalization in topological insulator Bi_2Te_3 microflakes. *Phys. Rev. B - Condens. Matter Mater. Phys.* **87**, 1–7 (2013).

39. Bao, L. *et al.* Weak anti-localization and quantum oscillations of surface states in topological insulator Bi_2Se_2Te. *Sci. Rep.* **2**, 1–7 (2012).

40. Aharonov, Y. & Bohm, D. Electromagnetic Potentials in the Quantum Theory. *Phys. Rev.* **123**,

1511–1524 (1961).

41. Schubnikow, L. & De Haas, W. J. New phenomenon in the change of resistance in a magnetic field of single crystal Bismuth. *Nat.* **126**, 3179 (1930).

42. Zhu, T. J., Hu, L. P., Zhao, X. B. & He, J. New insights into intrinsic point defects in v_2vi_3 thermoelectric materials. *Adv. Sci.* **3**, (2016).

43. Hong, S. S., Cha, J. J., Kong, D. & Cui, Y. Ultra-low carrier concentration and surface-dominant transport in antimony-doped Bi_2Se_3 topological insulator nanoribbons. *Nat. Commun.* **3**, (2012).

44. Bando, H. *et al.* The time-dependent process of oxidation of the surface of Bi_2Te_3 studied by x-ray photoelectron spectroscopy. *J. Phys. Condens. Matter* **12**, 5607–5616 (2000).

45. Guo, J. H. *et al.* Surface oxidation properties in a topological insulator Bi_2Te_3 film. *Chinese Phys. Lett.* **30**, (2013).

46. Hor, Y. S. *et al.* P -type Bi_2Se_3 for topological insulator and low-temperature thermoelectric applications. *Phys. Rev. B - Condens. Matter Mater. Phys.* **79**, 2–6 (2009).

47. Taskin, A. A., Ren, Z., Sasaki, S., Segawa, K. & Ando, Y. Observation of dirac holes and electrons in a topological insulator. *Phys. Rev. Lett.* **107**, 1–4 (2011).

48. Kong, D. *et al.* Ambipolar field effect in the ternary topological insulator $(Bi_xSb_{1-x})_2Te_3$ by composition tuning. *Nat. Nanotechnol.* **6**, 705–709 (2011).

49. Wang, Y. *et al.* Gate-controlled surface conduction in Na-doped Bi_2Te_3 topological insulator nanoplates. *Nano Lett.* **12**, 1170–1175 (2012).

50. Chen, J. *et al.* Gate-voltage control of chemical potential and weak antilocalization in Bi_2Se_3. *Phys. Rev. Lett.* **105**, 1–4 (2010).

51. Steinberg, H., Gardner, D. R., Lee, Y. S. & Jarillo-Herrero, P. Surface state transport and ambipolar electric field effect in Bi_2Se_3 nanodevices. *Nano Lett.* **10**, 5032–5036 (2010).

52. Xiu, F. *et al.* Manipulating surface states in topological insulator nanoribbons. *Nat. Nanotechnol.* **6**, 216–221 (2011).

53. Qu, D. X., Hor, Y. S., Xiong, J., Cava, R. J. & Ong, N. P. Quantum oscillations and hall anomaly of surface states in the topological insulator Bi_2Te_3. *Science (80-.).* **329**, 821–824 (2010).

54. Ren, Z., Taskin, A. A., Sasaki, S., Segawa, K. & Ando, Y. Large bulk resistivity and surface quantum oscillations in the topological insulator Bi_2Te_2Se. *Phys. Rev. B - Condens. Matter Mater. Phys.* **82**, 1–4 (2010).

55. Lu, H.-Z. & Shen, S.-Q. Weak localization and weak anti-localization in topological insulators. *Spintron. VII* **9167**, 91672E (2014).

56. Hikami, S. PTP-63-707.pdf. *Progress of Theoretical Physics* vol. 63 707 (1980).

57. Sch, T. & Gr, P. Spintronics and Emergent Qubits 1 Forschungszentrum J ulich. (2013).

58. Connerade, J.-P., Solóvyov, A. & Surdutovich, E. A Review of Quantum Confinement. **1**, 1–33 (2010).

59. Shin, H. S. *et al.* The surface-to-volume ratio: A key parameter in the thermoelectric transport

of topological insulator Bi_2Se_3 nanowires. *Nanoscale* **8**, 13552–13557 (2016).

60. Hamdou, B., Gooth, J., Dorn, A., Pippel, E. & Nielsch, K. Surface state dominated transport in topological insulator Bi_2Te_3 nanowires. *Appl. Phys. Lett.* **103**, (2013).

61. Hinsche, N. F. *et al.* Impact of the topological surface state on the thermoelectric transport in Sb_2Te_3 thin films. *ACS Nano* **9**, 4406–4411 (2015).

62. Kong, D. & Cui, Y. Opportunities in chemistry and materials science for topological insulators and their nanostructures. *Nat. Chem.* **3**, 845–849 (2011).

63. Snyder, G. J. & Toberer, E. S. Complex TE meterials. *Nat. Mater.* **7**, 105–114 (2008).

64. Yang, J. Potential applications of thermoelectric waste heat recovery in the automotive industry. *Int. Conf. Thermoelectr. ICT, Proc.* **2005**, 170–174 (2005).

65. Ohara, B. *et al.* Optimization Strategies for a Portable Thermoelectric Vaccine Refrigeration System in Developing Communities. *J. Electron. Mater.* **44**, 1614–1626 (2015).

66. Yang, J. & Caillat, T. Thermoelectric Materials for Space Cooling. *Energy Convers. Sp. Power* **31**, 111–121 (1961).

67. Goldsmid, H. J. Bismuth telluride and its alloys as materials for thermoelectric generation. *Materials (Basel).* **7**, 2577–2592 (2014).

68. Poudel, B. *et al.* High-thermoelectric performance of nanostructured bismuth antimony telluride bulk alloys. *Science (80-.).* **320**, 634–638 (2008).

69. Ashalley, E., Chen, H., Tong, X., Li, H. & Wang, Z. M. Bismuth telluride nanostructures: preparation, thermoelectric properties and topological insulating effect. *Front. Mater. Sci.* **9**, 103–125 (2015).

70. Mamur, H., Bhuiyan, M. R. A., Korkmaz, F. & Nil, M. A review on bismuth telluride (Bi_2Te_3) nanostructure for thermoelectric applications. *Renew. Sustain. Energy Rev.* **82**, 4159–4169 (2018).

71. Vineis, C. J., Shakouri, A., Majumdar, A. & Kanatzidis, M. G. Nanostructured thermoelectrics: Big efficiency gains from small features. *Adv. Mater.* **22**, 3970–3980 (2010).

72. Nielsch, K., Bachmann, J., Kimling, J. & Böttner, H. Thermoelectric nanostructures: From physical model systems towards nanograined composites. *Adv. Energy Mater.* **1**, 713–731 (2011).

73. Loor, M. *et al.* Ionic Liquid-Based Low-Temperature Synthesis of Phase-Pure Tetradymite-Type Materials and Their Thermoelectric Properties. *Inorg. Chem.* **59**, 3428–3436 (2020).

74. Chen, Z. G., Hana, G., Yanga, L., Cheng, L. & Zou, J. Nanostructured thermoelectric materials: Current research and future challenge. *Prog. Nat. Sci. Mater. Int.* **22**, 535–549 (2012).

75. Minnich, A. J., Dresselhaus, M. S., Ren, Z. F. & Chen, G. Bulk nanostructured thermoelectric materials: Current research and future prospects. *Energy Environ. Sci.* **2**, 466–479 (2009).

76. Mun, H., Choi, S. M., Lee, K. H. & Kim, S. W. Boundary Engineering for the Thermoelectric Performance of Bulk Alloys Based on Bismuth Telluride. *ChemSusChem* **8**, 2312–2326 (2015).

77. Schierning, G. *et al.* Concepts for medium-high to high temperature thermoelectric heat-to-electricity conversion: a review of selected materials and basic considerations of module

design. *Transl. Mater. Res.* **2**, 025001 (2015).

78. Ding, L. C., Akbarzadeh, A. & Tan, L. A review of power generation with thermoelectric system and its alternative with solar ponds. *Renew. Sustain. Energy Rev.* **81**, 799–812 (2018).

79. Huang, B. J., Chin, C. J. & Duang, C. L. Design method of thermoelectric cooler. *Int. J. Refrig.* **23**, 208–218 (2000).

80. Chein, R. & Huang, G. Thermoelectric cooler application in electronic cooling. *Appl. Therm. Eng.* **24**, 2207–2217 (2004).

81. Kishore, R. A. & Priya, S. A review on design and performance of thermomagnetic devices. *Renew. Sustain. Energy Rev.* **81**, 33–44 (2018).

82. Dai, Y., Wang, R. & Ni, L. Experimental investigation and analysis on a solar thermoelectric refrigerator. *Taiyangneng Xuebao/Acta Energiae Solaris Sin.* **23**, 754–758 (2002).

83. Nolas, G. S., Morelli, D. T. & Tritt, T. M. Skutterudites: a phonon-glass-electron crystal approach to advanced thermoelectric energy conversion applications. *Annu. Rev. Mater. Sci.* **29**, 89–116 (1999).

84. Goldsmid, H. J. & Nolas, G. S. A review of the new thermoelectric materials. *Int. Conf. Thermoelectr. ICT, Proc.* 1–6 (2001) doi:10.1109/ict.2001.979602.

85. Dresselhaus, M. S. *et al.* New directions for low-dimensional thermoelectric materials. *Adv. Mater.* **19**, 1043–1053 (2007).

86. Li, J. F., Liu, W. S., Zhao, L. D. & Zhou, M. High-performance nanostructured thermoelectric materials. *NPG Asia Mater.* **2**, 152–158 (2010).

87. Hicks, L. & Dresselhaus, M. S. of of a. *Phys. Rev. B* **47**, 8–11 (1993).

88. Mahan, G. D. & Sofo, J. O. The best thermoelectric. *Proc. Natl. Acad. Sci. U. S. A.* **93**, 7436–7439 (1996).

89. Heremans, J. P. *et al.* Enhancement of Thermoelectric of the Electronic Density of States. *Science (80-.).* **321**, 1457–1461 (2008).

90. Cutler, M. & Mott, N. F. Observation of anderson localization in an electron gas. *Phys. Rev.* **181**, 1336–1340 (1969).

91. Harman, T. C., Taylor, P. J., Walsh, M. P. & LaForge, B. E. Quantum dot superlattice thermoelectric materials and devices. *Science (80-.).* **297**, 2229–2232 (2002).

92. Ohta, H. *et al.* Giant thermoelectric Seebeck coefficient of a two-dimensional electron gas in SrTiO3. *Nat. Mater.* **6**, 129–134 (2007).

93. Venkatasubramanian, R., Siivola, E., Colpitts, T. & O'Quinn, B. Thin-film thermoelectric devices with high room-temperature figures of merit. *Nature* **413**, 597–602 (2001).

94. Caylor, J. C., Coonley, K., Stuart, J., Colpitts, T. & Venkatasubramanian, R. Enhanced thermoelectric performance in PbTe-based superlattice structures from reduction of lattice thermal conductivity. *Appl. Phys. Lett.* **87**, (2005).

95. Hao, Q., Xu, D., Lu, N. & Zhao, H. High-throughput ZT predictions of nanoporous bulk materials as next-generation thermoelectric materials: A material genome approach. *Phys. Rev. B* **93**, 1–11 (2016).

96. Winkler, M. *et al.* Current status in fabrication, structural and transport property characterization, and theoretical understanding of Bi_2Te_3 / Sb_2Te_3 superlattice systems. *Zeitschrift fur Anorg. und Allg. Chemie* **638**, 2441–2454 (2012).

97. Mehta, R. J. *et al.* A new class of doped nanobulk high-figure-of-merit thermoelectrics by scalable bottom-up assembly. *Nat. Mater.* **11**, 233–240 (2012).

98. Hu, L. *et al.* Enhancement in thermoelectric performance of bismuth telluride based alloys by multi-scale microstructural effects. *J. Mater. Chem.* **22**, 16484–16490 (2012).

99. Zhang, Z., Sharma, P. A., Lavernia, E. J. & Yang, N. Thermoelectric and transport properties of nanostructured Bi_2Te_3 by spark plasma sintering. *J. Mater. Res.* **26**, 475–484 (2011).

100. Zhao, L. D., Zhang, B. P., Li, J. F., Zhou, M. & Liu, W. S. Effects of process parameters on electrical properties of n-type Bi2Te3 prepared by mechanical alloying and spark plasma sintering. *Phys. B Condens. Matter* **400**, 11–15 (2007).

101. Yamashita, O., Tomiyoshi, S. & Makita, K. Bismuth telluride compounds with high thermoelectric figures of merit. *J. Appl. Phys.* **93**, 368–374 (2003).

102. Zemskov, V. S., Belaya, A. D., Beluy, U. S. & Kozhemyakin, G. N. Growth and investigation of thermoelectric properties of Bi-Sb alloy single crystals. *J. Cryst. Growth* **212**, 161–166 (2000).

103. Tang, X. *et al.* Preparation and thermoelectric transport properties of high-performance p-type Bi_2Te_3 with layered nanostructure. *Appl. Phys. Lett.* **90**, 1–4 (2007).

104. Ivanov, O., Maradudina, O. & Lyubushkin, R. Grain size effect on electrical resistivity of bulk nanograined Bi_2Te_3 material. *Mater. Charact.* **99**, 175–179 (2015).

105. Ma, Y. *et al.* Enhanced thermoelectric figure-of-merit in p-type nanostructured bismuth antimony tellurium alloys made from elemental chunks. *Nano Lett.* **8**, 2580–2584 (2008).

106. Xie, W., Tang, X., Yan, Y., Zhang, Q. & Tritt, T. M. Unique nanostructures and enhanced thermoelectric performance of melt-spun BiSbTe alloys. *Appl. Phys. Lett.* **94**, 2007–2010 (2009).

107. Zhao, L. D., Zhang, B. P., Liu, W. S. & Li, J. F. Effect of mixed grain sizes on thermoelectric performance of Bi_2Te_3 compound. *J. Appl. Phys.* **105**, (2009).

108. Kim, S. Il *et al.* Dense dislocation arrays embedded in grain boundaries for high-performance bulk thermoelectrics. *Science (80-.).* **348**, 109–114 (2015).

109. Hao, Q. Effective medium formulation for phonon transport analysis of nanograined polycrystals. *J. Appl. Phys.* **111**, (2012).

110. Takahashi, R. & Murakami, S. Thermoelectric transport in perfectly conducting channels in quantum spin Hall systems. *Phys. Rev. B - Condens. Matter Mater. Phys.* **81**, 1–4 (2010).

111. Xu, N., Xu, Y. & Zhu, J. Topological insulators for thermoelectrics. *npj Quantum Mater.* **2**, 1–9 (2017).

112. Xu, Y., Gan, Z. & Zhang, S. C. Enhanced thermoelectric performance and anomalous seebeck effects in topological insulators. *Phys. Rev. Lett.* **112**, 1–5 (2014).

113. Xu, Y. Thermoelectric effects and topological insulators. *Chinese Phys. B* **25**, (2016).

114. Rittweger, F., Hinsche, N. F., Zahn, P. & Mertig, I. Signature of the topological surface state in the thermoelectric properties of Bi_2Te_3. *Phys. Rev. B - Condens. Matter Mater. Phys.* **89**, 1–6

(2014).

115. Sun, G. L. *et al.* Enhanced thermoelectric performance of nanostructured topological insulator Bi_2Se_3. *Appl. Phys. Lett.* **106**, 1–5 (2015).

116. Goldsmid, H. J. & Douglas, R. W. The use of semiconductors in thermoelectric refrigeration. *Br. J. Appl. Phys.* **5**, 386–390 (1954).

117. Ying, P. *et al.* Towards tellurium-free thermoelectric modules for power generation from low-grade heat. *Nat. Commun.* **12**, 1–6 (2021).

118. Bauer, C. *et al.* Heterostructured Bismuth Telluride Selenide Nanosheets for Enhanced Thermoelectric Performance. *Small Sci.* **1**, 2000021 (2021).

119. Sehr, R. & Testardi, L. R. The optical properties of p-type $Bi_2Te_3Sb_2Te_3$ alloys between 2-15 microns. *J. Phys. Chem. Solids* **23**, 1219–1224 (1962).

120. Hashibon, A. & Elsässer, C. First-principles density functional theory study of native point defects in Bi_2Te_3. *Phys. Rev. B - Condens. Matter Mater. Phys.* **84**, 14–16 (2011).

121. Teweldebrhan, D., Goyal, V. & Balandin, A. A. Exfoliation and characterization of bismuth telluride atomic quintuples and quasi-two-dimensional crystals. *Nano Lett.* **10**, 1209–1218 (2010).

122. Soni, A. *et al.* Interface driven energy filtering of thermoelectric power in spark plasma sintered $Bi_2Te_{2.7}Se_{0.3}$ nanoplatelet composites. *Nano Lett.* **12**, 4305–4310 (2012).

123. Yan, X. *et al.* Experimental studies on anisotropic thermoelectric properties and structures of n-type $Bi_2Te_{2.7}Se_{0.3}$. *Nano Lett.* **10**, 3373–3378 (2010).

124. Kim, D. H., Kim, C., Heo, S. H. & Kim, H. Influence of powder morphology on thermoelectric anisotropy of spark-plasma-sintered Bi-Te-based thermoelectric materials. *Acta Mater.* **59**, 405–411 (2011).

125. Shafai, C. & Brett, M. J. Optimization of Bi_2Te_3 thin films for microintegrated Peltier heat pumps. *J. Vac. Sci. Technol. A Vacuum, Surfaces, Film.* **15**, 2798–2801 (1997).

126. Zhang, Z., Wang, Y., Deng, Y. & Xu, Y. The effect of (00l) crystal plane orientation on the thermoelectric properties of Bi_2Te_3 thin film. *Solid State Commun.* **151**, 1520–1523 (2011).

127. Lin, J. M. *et al.* Thermoelectric properties of Bi_2Te_3 thin films prepared by thermal evaporation method. *Innov. Commun. Eng. - Proc. 2nd Int. Conf. Innov. Commun. Eng. ICICE 2013* **2013**, 35–38 (2014).

128. Lan, Y. *et al.* Structure study of bulk nanograined thermoelectric bismuth antimony telluride. *Nano Lett.* **9**, 1419–1422 (2009).

129. Cao, Y. Q., Zhao, X. B., Zhu, T. J., Zhang, X. B. & Tu, J. P. Syntheses and thermoelectric properties of Bi_2Te_3 Sb_2Te_3 bulk nanocomposites with laminated nanostructure. *Appl. Phys. Lett.* **92**, 90–93 (2008).

130. Zhao, X. B. *et al.* Bismuth telluride nanotubes and the effects on the thermoelectric properties of nanotube-containing nanocomposites. *Appl. Phys. Lett.* **86**, 1–3 (2005).

131. Heimann, S. *et al.* Record figure of merit values of highly stoichiometric Sb_2Te_3 porous bulk synthesized from tailor-made molecular precursors in ionic liquids. *J. Mater. Chem. C* **3**, 10375–10380 (2015).

132. Zastrow, S. *et al.* Thermoelectric transport and Hall measurements of low defect Sb_2Te_3 thin films grown by atomic layer deposition. *Semicond. Sci. Technol.* **28**, (2013).

133. Rusek, M., Komossa, T., Bendt, G. & Schulz, S. Bismuth amides as promising ALD precursors for Bi_2Te_3 films. *J. Cryst. Growth* **470**, 128–134 (2017).

134. Bendt, G. *et al.* Deposition of topological insulator Sb_2Te_3 films by an MOCVD process. *J. Mater. Chem. A* **2**, 8215–8222 (2014).

135. Brebrick, R. F. Homogeneity ranges and Te_2-pressure along the three-phase curves for Bi_2Te_3(c) and a 55-58 at.% Te, peritectic phase. *J. Phys. Chem. Solids* **30**, 719–731 (1969).

136. Cho, S. *et al.* Antisite defects of Bi_2Te_3 thin films. *Appl. Phys. Lett.* **75**, 1401–1403 (1999).

137. Kim, D. H. & Mitani, T. Thermoelectric properties of fine-grained Bi_2Te_3 alloys. *J. Alloys Compd.* **399**, 14–19 (2005).

138. Schulz, S. *et al.* Synthesis of hexagonal Sb_2Te_3 nanoplates by thermal decomposition of the single-source precursor (Et 2 Sb) 2 Te. *Chem. Mater.* **24**, 2228–2234 (2012).

139. Stavila, V. *et al.* Wet-chemical synthesis and consolidation of stoichiometric bismuth telluride nanoparticles for improving the thermoelectric figure-of-merit. *ACS Appl. Mater. Interfaces* **5**, 6678–6686 (2013).

140. Bendt, G., Schulz, S., Zastrow, S. & Nielsch, K. Single-source precursor-based deposition of Sb_2Te_3 films by MOCVD. *Chem. Vap. Depos.* **19**, 235–241 (2013).

141. Bendt, G. *et al.* Structural and thermoelectrical characterization of epitaxial Sb_2Te_3 high quality thin films grown by thermal evaporation. *Semicond. Sci. Technol.* **33**, (2018).

142. Rieger, F. *et al.* Low intrinsic c-axis thermal conductivity in PVD grown epitaxial Sb_2Te_3 films. *J. Appl. Phys.* **123**, (2018).

143. Stavila, V. *et al.* Wet-chemical synthesis and consolidation of stoichiometric bismuth telluride nanoparticles for improving the thermoelectric figure-of-merit. *ACS Appl. Mater. Interfaces* **5**, 6678–6686 (2013).

144. Zhang, C., Ng, H., Li, Z., Khor, K. A. & Xiong, Q. Minority Carrier Blocking to Enhance the Thermoelectric Performance of Solution-Processed $Bi_xSb_{2-x}Te_3$ Nanocomposites via a Liquid-Phase Sintering Process. *ACS Appl. Mater. Interfaces* **9**, 12501–12510 (2017).

145. Koch, C. & Rinke, T. *Photolithography Basics of Microstructuring*. (Siegel Druck & Medien GmbH & Co. KG, 2020).

146. Van der PAUW, L. J. A method of measuring specific resistivity and Hall effect of discs of arbitary shape. *Philips Res. Repts* 13, 1–9 (1958).

147. Saleemi, M., Toprak, M. Synthesis, processing and thermoelectric properties of bulk nanostructured bismuth telluride (Bi_2Te_3). *J.Mater. Chem.* **22**, 725 (2012).

148. Wang, Z. H. *et al.* Granularity controlled nonsaturating linear magnetoresistance in topological insulator Bi_2Te_3 films. *Nano Lett.* **14**, 6510–6514 (2014).

149. Zhang, H. B. *et al.* Weak localization bulk state in a topological insulator Bi_2Te_3 film. *Phys. Rev. B - Condens. Matter Mater. Phys.* **86**, 1–7 (2012).

150. Lee, H. Y. *et al.* Epitaxial growth of Bi_2Te_3 topological insulator thin films by temperature-gradient induced physical vapor deposition (PVD). *J. Alloys Compd.* **686**, 989–997 (2016).

151. Butch, N. P. *et al.* Strong surface scattering in ultrahigh-mobility Bi_2Se_3 topological insulator crystals. *Phys. Rev. B - Condens. Matter Mater. Phys.* **81**, 3–6 (2010).

152. Lakhani, A. & Kumar, D. Observation of multichannel quantum coherent transport and electron-electron interaction in Bi_2Te_3 single crystal. *Appl. Phys. Lett.* **114**, 0–5 (2019).

153. Tian, M. *et al.* Dual evidence of surface Dirac states in thin cylindrical topological insulator Bi_2Te_3 nanowires. *Sci. Rep.* **3**, 1–7 (2013).

154. Hor, Y. S., Qu, D., Ong, N. P. & Cava, R. J. Low temperature magnetothermoelectric effect and magnetoresistance in Te vapor annealed Bi_2Te_3. *J. Phys. Condens. Matter* **22**, (2010).

155. Zhang, S. X. *et al.* Magneto-resistance up to 60 Tesla in topological insulator Bi_2Te_3 thin films. *Appl. Phys. Lett.* **101**, 2–6 (2012).

156. Dey, R. *et al.* Strong spin-orbit coupling and Zeeman spin splitting in angle dependent magnetoresistance of Bi_2Te_3. *Appl. Phys. Lett.* **104**, (2014).

157. Chiu, S. P. & Lin, J. J. Weak antilocalization in topological insulator Bi_2Te_3 microflakes. *Phys. Rev. B - Condens. Matter Mater. Phys.* **87**, 1–7 (2013).

158. Ning, W. *et al.* One-dimensional weak antilocalization in single-crystal Bi_2Te_3 nanowires. *Sci. Rep.* **3**, 1–6 (2013).

159. Kumar, D. & Lakhani, A. Effect of band bending on topological surface transport of Bi_2Te_3 single crystal. *J. Phys. Condens. Matter* **33**, (2020).

160. Shrestha, K. *et al.* Extremely large nonsaturating magnetoresistance and ultrahigh mobility due to topological surface states in the metallic Bi_2Te_3 topological insulator. *Phys. Rev. B* **95**, 1–6 (2017).

161. Chiatti, O. *et al.* 2D layered transport properties from topological insulator Bi_2Se_3 single crystals and micro flakes. *Sci. Rep.* **6**, 1–11 (2016).

162. He, H. T. *et al.* Impurity effect on weak antilocalization in the topological insulator Bi_2Te_3. *Phys. Rev. Lett.* **106**, 1–4 (2011).

163. Jing, Y. *et al.* Weak antilocalization and electron-electron interaction in coupled multiple-channel transport in a Bi_2Se_3 thin film. *Nanoscale* **8**, 1879–1885 (2016).

164. Qin, L. X. *et al.* Confined-path interference suppressed quantum correction on weak antilocalization effect in a $BiSbTeSe_2$ topological insulator. *Appl. Phys. Lett.* **112**, 1–6 (2018).

165. De Castro, S. *et al.* Systematic study of transport via surface and bulk states in Bi_2Te_3 topological insulator. *Mater. Res. Express* **3**, (2016).

166. Shekhar, C. *et al.* Evidence of surface transport and weak antilocalization in a single crystal of the Bi_2Te_2Se topological insulator. *Phys. Rev. B - Condens. Matter Mater. Phys.* **90**, 1–6 (2014).

167. Assaf, B. A. *et al.* Linear magnetoresistance in topological insulator thin films: Quantum phase coherence effects at high temperatures. *Appl. Phys. Lett.* **102**, (2013).

168. Chiatti, O. *et al.* 2D layered transport properties from topological insulator Bi 2 Se 3 single crystals and micro flakes. *Sci. Rep.* **6**, 1–11 (2016).

169. Tang, C. S. *et al.* Terahertz conductivity of topological surface states in $Bi_{1.5}Sb_{0.5}Te_{1.8}Se_{1.2}$. *Sci. Rep.* **3**, 3–8 (2013).

170. Park, B. C. *et al.* Terahertz single conductance quantum and topological phase transitions in topological insulator Bi_2Se_3 ultrathin films. *Nat. Commun.* **6**, (2015).

171. Horng, J. *et al.* Drude conductivity of Dirac fermions in graphene. *Phys. Rev. B - Condens. Matter Mater. Phys.* **83**, 1–5 (2011).

172. Han, J. W. *et al.* Extraction of optical constants using multiple reflections in the terahertz emitter-sample hybrid structure. *Opt. Lett.* **39**, 5531 (2014).

173. Shimakawa, K., Itoh, T., Naito, H. & Kasap, S. O. The origin of non-Drude terahertz conductivity in nanomaterials. *Appl. Phys. Lett.* **100**, 10–13 (2012).

174. Crassee, I. *et al.* Intrinsic terahertz plasmons and magnetoplasmons in large scale monolayer graphene. *Nano Lett.* **12**, 2470–2474 (2012).

175. Huang, B. L. & Kaviany, M. Ab initio and molecular dynamics predictions for electron and phonon transport in bismuth telluride. *Phys. Rev. B - Condens. Matter Mater. Phys.* **77**, 1–19 (2008).

176. Wolos, A. *et al.* Landau-level spectroscopy of relativistic fermions with low Fermi velocity in the Bi_2Te_3 three-dimensional topological insulator. *Phys. Rev. Lett.* **109**, 1–5 (2012).

177. Yamamoto, M. & Hamada, N. First-principles estimation of seebeck coefficient of bismuth telluride and selenide. *Jpn. J. Appl. Phys.* **51**, (2012).

178. Gooth, J., Hamdou, B., Dorn, A., Zierold, R. & Nielsch, K. Resolving the Dirac cone on the surface of Bi_2Te_3 topological insulator nanowires by field-effect measurements. *Appl. Phys. Lett.* **104**, (2014).

179. Tang, C. S. *et al.* Terahertz conductivity of topological surface states in $Bi_{1.5}Sb_{0.5}Te_{1.8}Se_{1.2}$. *Sci. Rep.* **3**, 3–8 (2013).

180. Jadidi, M. M. *et al.* Nonlinear Terahertz Absorption of Graphene Plasmons. *Nano Lett.* **16**, 2734–2738 (2016).

181. Ju, L. *et al.* Graphene plasmonics for tunable terahertz metamaterials. *Nat. Nanotechnol.* **6**, 630–634 (2011).

182. Dordevic, S. V., Wolf, M. S., Stojilovic, N., Lei, H. & Petrovic, C. Signatures of charge inhomogeneities in the infrared spectra of topological insulators Bi_2Se_3, Bi_2Te_3 and Sb_2Te_3. *J. Phys. Condens. Matter* **25**, 1–5 (2013).

183. Dirmyer, M. R., Martin, J., Nolas, G. S., Sen, A. & Badding, J. V. Thermal and electrical conductivity of size-tuned bismuth telluride nanoparticles. *Small* **5**, 933–937 (2009).

184. Sumithra, S. *et al.* Enhancement in thermoelectric figure of merit in nanostructured Bi_2Te_3 with semimetal nanoinclusions. *Adv. Energy Mater.* **1**, 1141–1147 (2011).

185. Pettes, M. T., Maassen, J., Jo, I., Lundstrom, M. S. & Shi, L. Effects of surface band bending and scattering on thermoelectric transport in suspended bismuth telluride nanoplates. *Nano Lett.* **13**, 5316–5322 (2013).

186. Huang, B., Li, G., Yang, X. & Zhai, P. Capturing anharmonic and anisotropic natures in the thermotics and mechanics of Bi2Te3 thermoelectric material through an accurate and efficient potential. *J. Phys. D. Appl. Phys.* **52**, (2019).

Statement of Authorship

Except where reference is made in text of this thesis, this thesis contains no material published elsewhere or extracted in whole or in part from a thesis presented by me for another degree or diploma. This thesis has not been submitted for the award of any other degree or diploma in any other tertiary institution.

Sepideh Izadi

Bielefeld, July, 2021